TECHNICAL REPORT
NATICK/TR-04/006

AD_____

DISCOVERY AND UTILIZATION OF NANOSCALE AND MESOSCALE ENABLING MATERIALS AND PROCESSES FOR OPTOELECTRONICS AND ELECTRONIC INTERCONNECTS

by
Sanford Asher
John T. Yates, Jr.
Craig Wilcox
Gilbert Walker
Rob Coalson
Joachim Ahner
Jeremy Levy
David Beratan
and
Michael Hopkins

University of Pittsburgh
Pittsburgh, PA 15260

December 2003

Final Report
October 1999 – June 2002

20040112 185

REPORT DOCUMENTATION PAGE

Form Approved
OMB No. 0704-0188

1. REPORT DATE (DD-MM-YYYY)	2. REPORT TYPE	3. DATES COVERED (From - To)
17-12-2003	Final Report	October 1999 - June 2002

4. TITLE AND SUBTITLE
DISCOVERY AND UTILIZATION OF NANOSCALE AND MESOSCALE ENABLING MATERIALS AND PROCESSES FOR OPTOELECTRONICS AND ELECTRONIC INTERCONNECTS

5a. CONTRACT NUMBER
C-DAAD16-99-C-1036

5b. GRANT NUMBER

5c. PROGRAM ELEMENT NUMBER

6. AUTHOR(S)
Sanford Asher, John T. Yates, Jr., Craig Wilcox, Gilbert Walker, Rob Coalson, Joachim Ahner, Jeremy Levy, David Beratan, and Michael Hopkins

5d. PROJECT NUMBER

5e. TASK NUMBER

5f. WORK UNIT NUMBER

7. PERFORMING ORGANIZATION NAME(S) AND ADDRESS(ES)
University of Pittsburgh
Department of Chemistry
701 Chevron Science Center
219 Parkman Drive
Pittsburgh, PA 15260

8. PERFORMING ORGANIZATION REPORT NUMBER

9. SPONSORING/MONITORING AGENCY NAME(S) AND ADDRESS(ES)
Sponsor: Defense Advanced Research Projects Agency (DARPA)
Microsystems Technology Office (Elana Ethridge)
3701 North Fairfax Drive
Arlington, VA 22203-1714

10. SPONSOR/MONITOR'S ACRONYM(S)

11. SPONSOR/MONITOR'S REPORT NUMBER(S)
NATICK/TR-04/006

12. DISTRIBUTION/AVAILABILITY STATEMENT
Approved for public release;
distribution is unlimited.

13. SUPPLEMENTARY NOTES
Monitor: US Army Research, Development and Engineering Command, Natick Soldier Center,
ATTN: AMSRD-NSC-SS-MA (T. Gilroy), Kansas Street, Natick, MA 01760-5020

14. ABSTRACT
This report describes the development of enabling mesoscale materials and development of new instrumentation and methodologies for nanoscale material characterization. The work involved the following eight separate efforts: 1. Use of Colloidal Array Photonic Materials for Photochemically and Photothermally Controllable Diffraction Devices; 2. Development of Methods to Fabricate Nanoscale and Mesoscale Enabling Materials such as Magnetically Anisotropic Spherical Particles; 3. Development of Methods to Fabricate Particles with Chemically Anisotropic Surfaces; 4. Theoretical Determination of the Dependence of Photonic Crystal Diffraction on Crystal Dielectric Modulation and the Crystal Defect Structures; 5. Development of Methods to Direct, Control and Study the Self-Assembly of Ge/Si Quantum Dots; 6. Fabrication of Molecular Scale Shift Register Memories; 7. Development of a Nanoworkbench for Analysis, Manipulation and Excitation of Individual Nanostructures; and 8. Development of Instrumentation and Methodologies for Chemical Imaging of Nanoscale Surface Structures.

15. SUBJECT TERMS

NANOSCALE MATERIALS	ELECTRONIC	PHYSICAL PHENOMENA
MESOSCALE MATERIALS	SMART MATERIALS	ENABLING TECHNOLOGIES
OPTOELECTRONICS	NANOSTRUCTURES	
INTERCONNECTS	RESEARCH PROGRAMS	

16. SECURITY CLASSIFICATION OF:			17. LIMITATION OF ABSTRACT	18. NUMBER OF PAGES	19a. NAME OF RESPONSIBLE PERSON
a. REPORT	b. ABSTRACT	c. THIS PAGE			Thomas Gilroy
U	U	U	SAR	92	19b. TELEPHONE NUMBER (include area code) 508-233-5855

Standard Form 298 (Rev. 8/98)
Prescribed by ANSI Std. Z39.18

TABLE OF CONTENTS

iii

LIST OF FIGURES

ix

LIST OF TABLES

PREFACE

This report describes the development of enabling mesoscale materials and development of new instrumentation and methodologies for nanoscale material characterization. The effort was funded by the Defense Advanced Projects Agency (DARPA), Arlington, VA, and the contract number, DAAD16-99-C-1036, was administered by the U.S. Army Natick Soldier Center (NSC), Natick, MA. The effort was conducted by the University of Pittsburgh, Department of Chemistry, Pittsburgh, PA, between October 1999 and June 2002.

DISCOVERY AND UTILIZATION OF NANOSCALE AND MESOSCALE ENABLING MATERIALS AND PROCESSES FOR OPTOELECTRONICS AND ELECTRONIC INTERCONNECTS

SUMMARY

This is the final report for contract number: DAAD16-99-C-1036 entitled, "Discovery and Utilization of Nanoscale and Mesoscale Enabling Materials and Processes for Optoelectronics and Electronic Interconnects", which was carried out by faculty, students and postdoctoral researchers at the University of Pittsburgh. The work here has developed enabling mesoscale materials and has developed new instrumentation and methodologies for nanoscale material characterization.

The work involves the following eight separate efforts:

1. **Use of Colloidal Array Photonic Materials for Photochemically and Photothermally Controllable Diffraction Devices.** We have created new photonic crystals whose diffraction wavelength is shifted by light. This material has utility in optical memories. At present the optical switching time of this material is slow (sec). Methods are proposed to dramatically speed up the photoresponse. A new photonic crystal material was fabricated which utilizes polymer volume phase transitions to actuate efficient optical limiting. Large refractive index modulations (0.15) are induced; this material should switch in a sub-μsec time frame.

2. **Development of Methods to Fabricate Nanoscale and Mesoscale Enabling Materials Such as Magnetically Anisotropic Spherical Particles.** We synthesized monodisperse ~200 nm superparamagnetic and ferromagnetic highly charged colloidal particles that readily form photonic crystals. We demonstrate new magnetic field induced self assembly phenomena. The position and orientation of these spheres can be controlled by external magnetic fields. This enables new methods to self assemble complex, functional chemical assemblies for electro-optics.

3. **Development of Methods to Fabricate Particles with Chemically Anisotropic Surfaces.** We developed methods to chemically functionalize anisotropic reactive chemical patches on colloidal particle surfaces. This enables new self-assembly techniques for electro-optical devices.

4. **Theoretical Determination of the Dependence of Photonic Crystal Diffraction on Crystal Dielectric Modulation and the Crystal Defect Structures.** We have developed a theoretical understanding of the dependence of photonic crystal diffraction on the photonic crystal dielectric modulation, crystal structure, defects and disorder. This quantitative understanding allows us to experimentally optimize colloidal crystal self-assembly and allows us to estimate the efficiency of optical filtering and switching.

5. **Development of Methods to Direct, Control and Study the Self-Assembly of Ge/Si Quantum Dots.** We developed novel approaches for controlling both the size and spacing of quantum dot structures, based on *directed* self-assembly on a strained wetting layer surface. We have demonstrated this methology on Ge/Si, although it should work equally well for III-V systems such as InAs/GaAs and II-VI systems like CdSe/ZnSe. We utilize the coexistence of a metastable 2D phase and an equilibrium 3D phase, and locally perturb the surface causing the nucleation of islands only in regions where the surface is perturbed. The perturbation is achieved by planting C atoms on Si with an STM tip. We have developed unique laser and AFM instrumentation for femtosecond time-resolved luminescence and transient absorption measurements. These studies elucidate the energy relaxation mechanisms, important for optoelectronic applications.

6. **Fabrication of Molecular Scale Shift Register Memories.** We have developed synthetic methods which allow us to fabricate supramolecular shift-register memories. We have modeled electron transfer in models of these compounds, and have clarified the important issues of electron transfer in these types of molecules.

7. **Development of a Nanoworkbench for Analysis, Manipulation, and Excitation of Individual Nanostructures.** We constructed a novel instrument that combines a multiple tip STM device, with an SEM and with an Auger analyzer for the study of single nanostructures. This system was coupled to a multiple UHV chamber system which allowed molecular beam epitaxy (MBE) and was equipped with multiple surface analysis capabilities.

8. **Development of Instrumentation and Methodologies for Chemical Imaging of Nanoscale Surface Structures.** We constructed an aperture less near-field scanning infrared microscope which has a spatial resolution of <100 nm. This novel instrument enables chemical mapping and imaging of surface nanoscale structures.

1.0 Introduction

This final report summarizes the results of research programs to harness novel physical phenomena and to develop new enabling materials to create practical devices. The work consists of the following seven separate efforts:

1. The Use of Colloidal Array Photonic Materials for Photochemically and Photothermally Controllable Diffraction Devices

2. Development of Methods to Fabricate Nanoscale and Mesoscale Enabling Materials Such as Magnetically Anisotropic Spherical Particles.

3. Development of Methods to Fabricate Particles with Chemically Anisotropic Surfaces

4. Theoretical Determination of the Dependence of Photonic Crystal Diffraction on Crystal Dielectric Modulation and the Crystal Defect Structures

5. Development of Methods to Direct, Control and Study the Self-Assembly of Ge/Si Quantum Dots

6. Fabrication of Molecular Scale Shift Register Memories

7. Development of a Nanoworkbench for Analysis, Manipulation, and Excitation of Individual Nanostructures."

8. Development of Instrumentation and Methodologies for Chemical Imaging of Nanoscale Surface Structures

2.0 Nanoscale to Mesoscale Smart Enabling Materials: Applications For Optical Limiting, Switching, and Optoelectronics Interconnects

2.1 Introduction

This portion of the research program utilizes photonic crystals fabricated through the self-assembly of highly charged colloidal particles into crystalline colloidal arrays (CCA)[1]. These CCA form as a result of the electrostatic repulsion between colloidal particles, due to the ionized functional groups attached to their surface. These monodisperse, highly charged colloidal particles are easily synthesized from a variety of organic and inorganic materials. If these particles have nearest neighbor spacings of <1 μm in water, they spontaneously self assemble into either a BCC or FCC array (Fig. 1) in order to minimize the system energy. We have polymerized hydrogels around the CCA (PCCA) to create rugged composite materials which possess the periodic ordering of the original CCA. These materials also display the responsive volume phase transition properties of hydrogels (Fig. 2)[1-5].

3
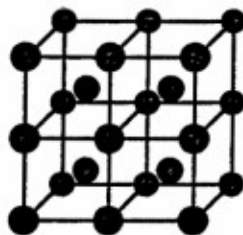
Figure 1. Crystalline colloidal arrays (CCA) form because of repulsion between monodisperse, highly charged colloidal particles in low ionic strength aqueous solutions. The particles form cubic arrays with a lattice spacing of several hundred nanometers and diffract visible light. Each sphere in this illustration represents a polyanionic colloidal particle.
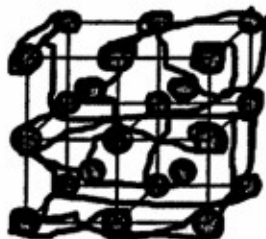
Figure 2. Polymerized CCA (PCCA) are formed by dissolving monomers in a CCA and polymerizing them to form a crosslinked hydrogel network. The hydrogel preserves the crystalline order of the array and can be modified to respond to target molecules or ions. PCCA swell when the charge on the hydrogel increases and shrink in response to increased crosslinking.

These PCCA Bragg diffract light efficiently in the UV, visible or near IR spectral region, depending on the fabricated array spacing. This diffraction phenomenon can be used to reject light transmission, for applications in optical switching[1,6,7] or limiting[6,7], or can be used to create visual patterns for display device applications[5], or it can be used to create spectral reporting elements for chemical sensors[3,4]. The work here attempted to fabricate more sophisticated PCCA, which utilize smart colloidal particles and smart hydrogels, to create highly efficient optical switches, limiters, nanoscale electronic interconnects and optoelectronic devices.

2.2 Fabrication of Photochemically Switchable Photonic Crystal Diffraction

We developed a method to photochemically switch the PCCA diffraction by covalently attaching azobenzene derivatives to the PCCA as shown in Fig. 3. Azobenzene derivatives are well known to show high quantum yield (0.1) photoisomerization from their ground state trans configuration to their ground state cis configuration.

Fig. 4 compares the transmission spectra of PCCA's with and without a covalently attached azobenzene derivative. In the absence of azobenzene the PCCA shows only diffraction from the fcc 111 planes at ~570 nm, as well as, higher order diffraction in the region below 300 nm. In addition absorption by the polystyrene colloids occurs below 300 nm. The PCCA containing covalently attached azobenzene shows, in addition, the 322 nm absorption band of trans azobenzene.

4
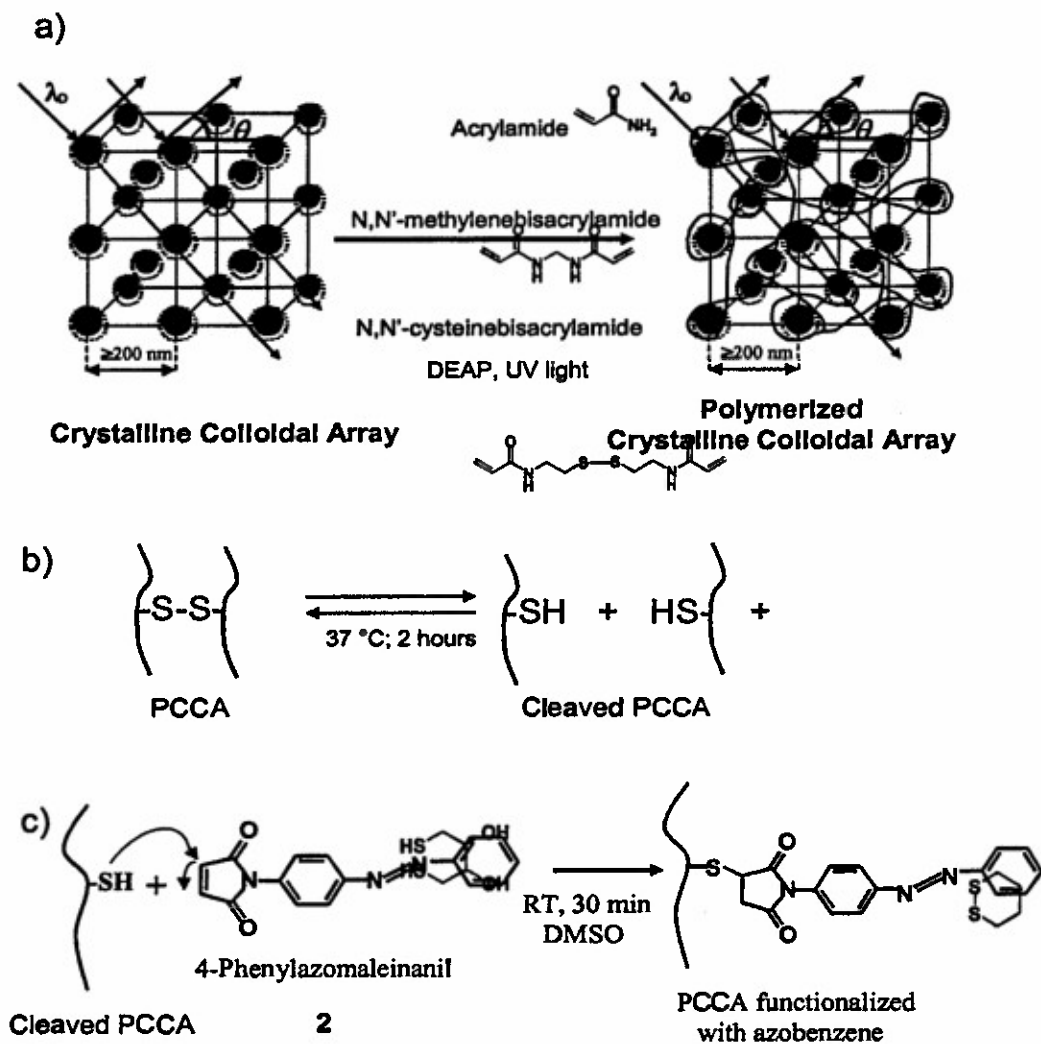
Figure 3. (a) Synthesis of photoresponsive PCCA containing an azobenzene derivative. (a) synthesis of PCCA with disulfide bonds (b) Cleavage of PCCA disulfide bonds with DTT (c) Attachment of azobenzene derivative via maleimide-thiol reaction.

Fig. 5 shows the dependence of the transmission spectrum of a PCCA with covalently attached azobenzene upon light illumination. This PCCA was oriented such that the incident beam is normal to the fcc 111 planes, which diffract ~525 nm light at normal incidence.

Excitation of the PCPCCA with ~365 nm UV light converts the ground state trans azobenzene to the cis form. This causes a bleaching of the 340 nm trans absorption band and an increase in the absorption of the cis band at ~440 nm. The diffraction shifts from ~525 nm to ~585 nm upon this conversion of the trans to the cis form. The diffraction of the cis form remains at 585 nm for over one week at room temperature in the dark; negligible ground state thermal conversion occurs from the cis to the trans form.

However, excitation at ~440 nm readily photoconverts the cis to the trans form, causing the diffraction to blue shift back to 525 nm. This PCCA can toggle back and forth between these diffraction values indefinitively (Fig. 6).

The diffraction shift must derive from an increased free energy of mixing of the hydrogel with the medium for the cis azobenzene derivative[3], since no change occurs in the hydrogel crosslink density or in its charge state. Presumably this increased free energy of mixing results from a more favorable solvation of the cis form compared to the trans form, due to its larger permanent dipole.

The rate of swelling and shrinkage of the hydrogel controls the rate of change in the diffraction condition. These rates are controlled by the collective diffusion constant of the hydrogel, the rate of water flow into and out of the hydrogel, and to the magnitude of the osmotic pressure due to the change in the free energy of mixing. For the macroscopic PCCA studied here we observe multisecond response times to 100 nsec UV excitation pulses.
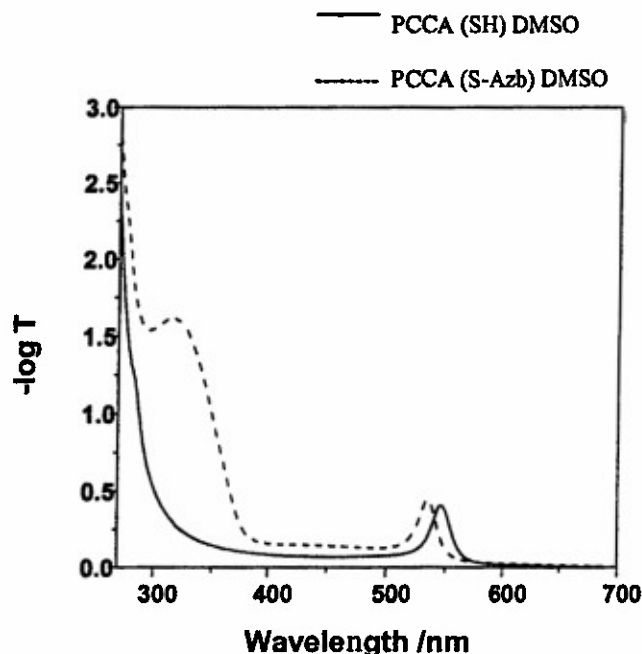
Figure 4. Comparison of PCCA with and without a covalently attached azobenzene derivative.
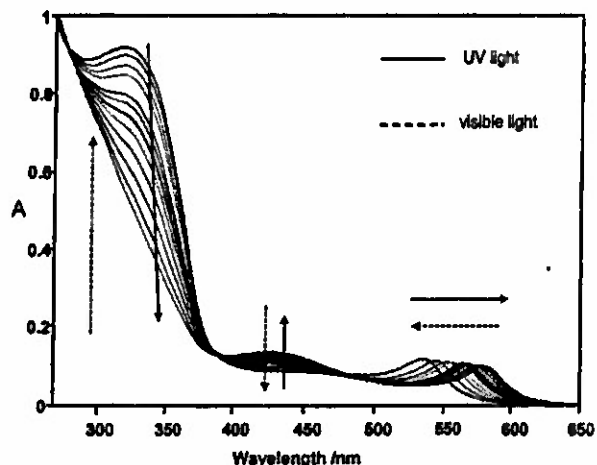
Figure 5. Photochemistry of a PCCA functionalized with 4-phenylazomaleinanil (4 mM) under visible wavelength and UV excitation. UV excitation converts trans azobenzene to the cis form. This shifts the diffraction to 585 nm. Excitation in the visible converts the cis to the trans form and shifts the diffraction back to 525 nm..
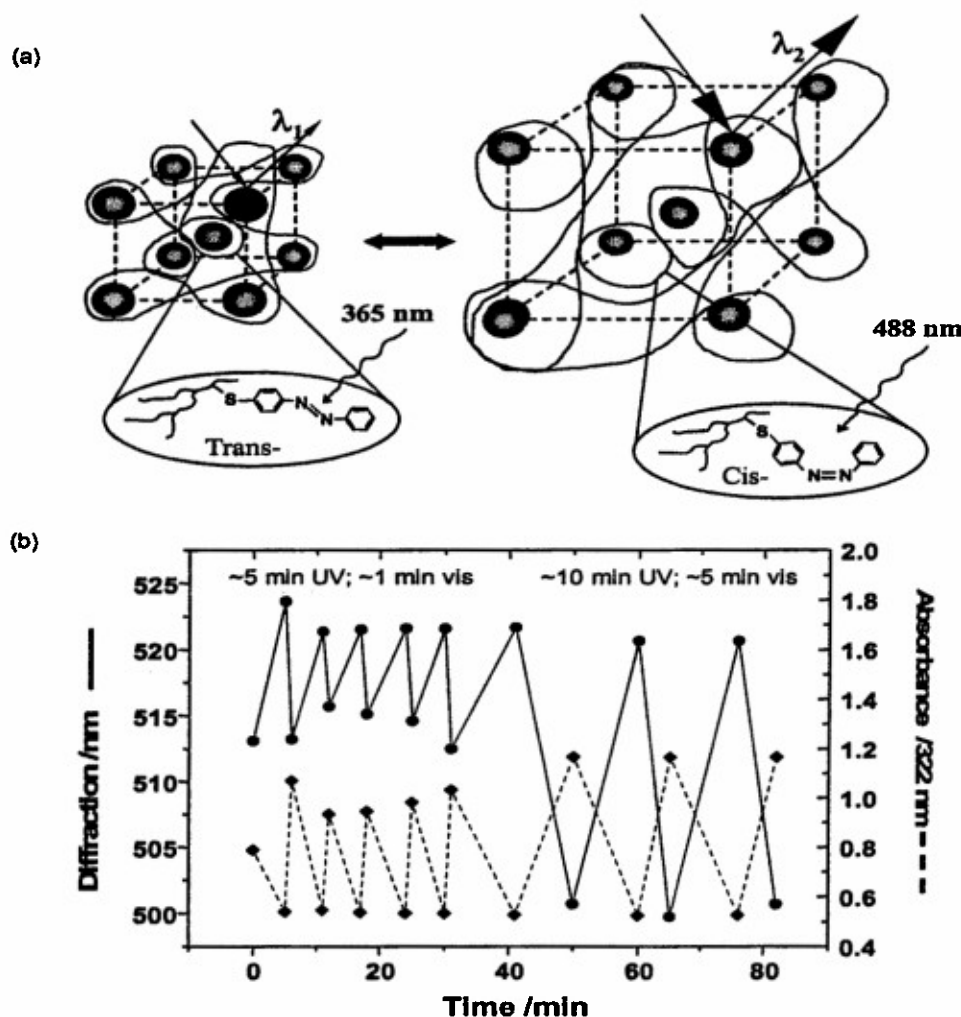
Figure 6. a) Photoisomerization of azobenzene attached to PCCA. b) Dependence of diffraction and 322 nm absorbance on UV and visible excitation and on excitation duration.

This rate of PCCA response is obviously too long for useful optical limiting or switching devices. However, this rate can be dramatically increased by decreasing the volume over which the hydrogel and water must respond. The swelling times should vary as r^{-2}, where r is the characteristic size of the device[8]. As discussed below we use this strategy in the hydrogel volume phase transition optical limiter work described below where we decrease the size by 1000-fold which should permit subμsec switching.

However, we cannot, as yet, decrease the size of our azobenzene photochemically driven PCCA. This is because the diffraction efficiencies are relatively modest due to the small refractive index differences between the PCCA polystyrene colloidal particles and the DMSO medium[10]. We are working on synthesizing titania colloids which would allow us to decrease the PCCA thickness by more than 100-fold. This approach would speed up the response rate by more than 10^4.

7

2.3 Fabrication of Optical Limiting Photonic Crystals

Normal Intensity
$n_s = n_m$

High Intensity
$n_s \neq n_m$
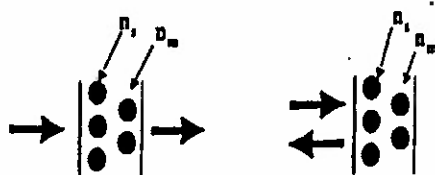
★ Thermal nonlinearity —— Dyed spheres.

★ Electronic nonlinearity—— Quantum dots.

Figure. 7 Concept for nonlinear PCCA. Under normal illumination the PCCA particles are refractive index matched to medium and no diffraction occurs. However, at high intensity illumination the particle refractive index diverges from that of the medium and the PCCA diffracts light meeting the Bragg condition.

We previously showed that PCCA containing dyed spheres can optically switch light in the nsec time regime[6,7,9]. These optical switching materials utilize colloidal spheres which are refractive index matched to the medium at normal light intensities, but at high light intensities the spheres heat up; the resulting refractive index mismatch with the medium causes the array to "pop up" to diffract away the incident radiation (Fig. 7). Our previous work utilized simple polymers and we relied on the polymer temperature density dependence to change the refractive index[6,7]. We demonstrated that, as predicted by theory, the switching occurs in the nsec time regime. Unfortunately, the efficiency was below that theoretically calculated, due to imperfect ordering of the CCA array.

The advantage of the PCCA for optical limiting is that very thin films can be used in parallel to protect different spectral regions. We envision a stack of limiters, each of which would be actuated and would protect only in a narrow spectral interval. If the limiter were actuated by a threat pulse in one spectral interval, only light in that interval would be rejected; light in adjacent spectral intervals would freely transmit to allow the observer to view the scene.

These PCCA optical switches could also be utilized for sophisticated optical processing. For example, it should be possible to focus light onto very small areas of the PCCA ($<10~\mu m^2$) which would separately respond to incident light intensity changes. This would permit the effective addressing of a large number of pixels; thus, this optical switching material could also be used for fast parallel image processing.

2.3.1 Development of Larger Refractive Index Nonlinearities

The diffraction efficiency and thus, the optical switching depend exponentially on the refractive index difference between the array and

Figure 8. Response of PCCA of NIPAM colloids to temperature change from 20 to 40 °C. The individual colloidal particles dramatically change their diameters, while the lattice constant stays constant.

8

the imbedding medium[10]. Thus, the efficiency of optical limiting or switching would be dramatically improved by increasing the refractive index change which occurs upon sphere heating. We are utilizing much larger refractive index which derive from polymer phase transitions. For example, the hydrogel volume phase transition in poly-N-isopropylacrylamide PNIPAM gives rise to $\Delta n > 0.1$ refractive index changes[5]. If these particles were in a diffracting CCA they would switch >99 % of the incident intensity at modest incident intensities. Because the colloidal particles are small <100 nm, these phase transition could occur in subμsec intervals. The limiting dynamics will be the water flow of out of the hydrogel spheres.

We utilized our previously determined method to synthesize monodisperse, highly charged PNIPAM colloidal particles[5]. These particles are ~3% polymer at 10°C and have a diameter of ~300 nm and a refractive index of ~1.35. They undergo a volume phase transition at ~33°C and shrink to a diameter of 100 nm, where they are ~100% polymer with a refractive index of ~1.50.

Figure 9. Response of NIPAM spheres PCCA to temperature. The large increase in diffraction at ~350 nm results from an increased diffraction by higher order planes.
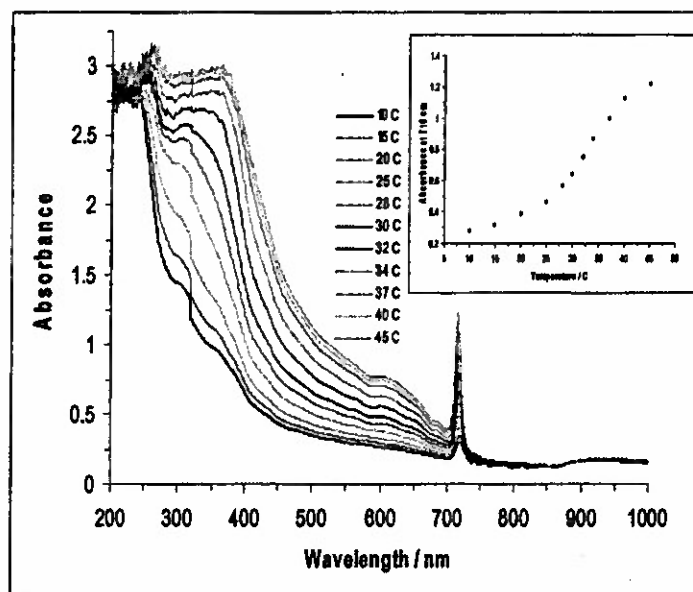
We have arrayed these PNIPAM particles in a CCA and have added acrylamide monomer and bisacrylamide crosslinker to polymerize the medium around the PNIPAM colloids. This PCCA continues to show the temperature induced volume phase transition of the PNIPAM spheres (Fig. 8 and 9). We have added an absorbing dye to this PNIPAM-PCCA and have demonstrated that laser absorption heats the water and causes the volume phase transition that causes the light to be diffracted away. We are now measuring these dynamics with a pulsed laser to determine the time scale of the optical switching.

2.4 Development of Enabling Anisotropic Colloidal Particles

We are developing synthetic procedures to fabricate particles which would be chemically anisotropically functionalized on their surfaces. These particles would function in devices such as electronic interconnects and could be used in self assembling machines. One approach to synthesizing chemically anisotropic spheres is to develop a method to synthesize monodisperse, ~100 nm magnetic colloidal particles whose position and orientation could be externally

9

controlled by magnetic fields. We would then functionalize the particle surface anisotropically as we reorient the spheres.

Our first attempts to fabricate magnetic colloids resulted in superparamagnetic colloidal particles[11,12] whose position could be controlled by external magnetic fields. These particles displayed a novel magnetic self assembly motif which could be used to form photonic crystals under conditions which normally prevent self-assembly.

We subsequently developed a synthesis for monodisperse ferromagnetic colloids. External magnetic fields could control both the orientation and position of these particles. We developed methods to functionalize the surface of these particles anisotropically. These particles also enabled novel magnetically controllable photonic crystals.

Fig. 10. TEM image of monodisperse polystyrene particles containing superparamagnetic nanoparticles. The aggregates of iron oxide nanoparticles appear as black dots in the larger polystyrene spheres. The polystyrene particle average diameter is 134 nm, with a polydispersity of 7.5%.

2.4.1 Synthesis of Superparamagnetic Colloidal Particles and Fabrication of Superparamagnetic Photonic Crystals

We synthesized monodisperse superparamagnetic particles by modifying the procedure of Yanase et al[14]. These superparamagnetic particles were synthesized by emulsion polymerization of styrene, in the presence of nanosized iron oxide particles formed by the coprecipitation of ferric and ferrous ions in ammonium hydroxide solution[15,16]. Before emulsion polymerization, the surface of these iron oxide particles was modified by adsorption of oleic acid. After emulsion polymerization, the polystyrene particles containing iron oxide inclusions were harvested with a magnet. TEM measurements indicate a 134 nm number average diameter (polydispersity 7.5%, Fig. 10).

These monodisperse superparamagnetic particles self-assemble into CCA in deionized water, due to electrostatic repulsive interactions between the individual spherical particles. When a permanent magnet is brought close to the CCA, an additional force occurs which causes the superparamagnetic particles to be attracted to the maximum of the local magnetic field gradient. Thus, the CCA is compressed along the magnetic field lines. As shown in Fig. 11, the diffraction wavelength blueshifts as the magnetic field and its gradient increases. The lattice constant observed is determined by the balance between the magnetic packing forces and the spherically symmetric interparticle electrostatic repulsive forces. Therefore, the lattice constant is a minimum at the locus of the magnetic field gradient maximum and increases as the gradient decreases.

10

Normally, CCA do not self assemble into highly ordered CCA in high ionic strength aqueous solutions or in polar organic solvents due to the weak interparticle electrostatic interactions. However, these superparamagnetic particles magnetically phase separate, and self assemble into highly ordered CCA within high ionic strength aqueous solutions and in polar organic solvents. Fig. 12 shows the dependence of the diffraction wavelength and the FCC 111 lattice constant on the NaCl concentration of aqueous solutions and on the dielectric constant of a series of polar organic solvents. The FCC 111 lattice constant decreases as the NaCl concentration increases, and as the organic solvent dielectric constant increases. The nearest neighbor sphere spacing of ~ 170 nm at 4 mM NaCl remains much larger than the particle diameter (134 nm).
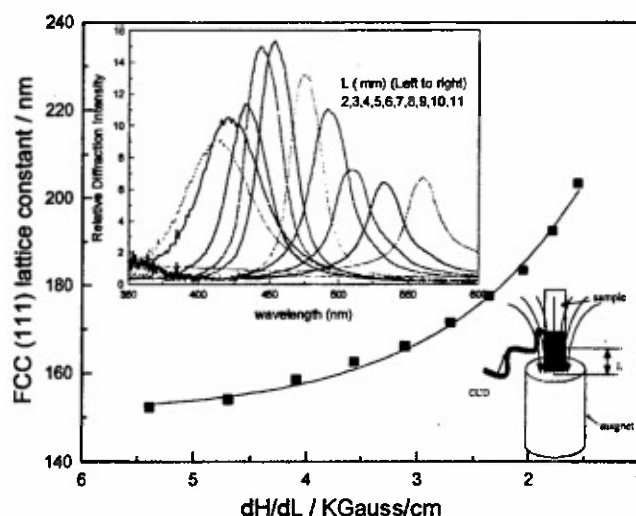
Fig. 11. Influence of the average magnetic field gradient, dH/dL on the lattice constant of a thick CCA composed of 134 nm superparamagnetic particles in deionized water (4.2 vol %). Top inset shows the dependence of the diffraction peak wavelength on the distance from the magnet. In the lower right is an experimental schematic showing the CCA on top of a permanent magnet, with an optical fiber probe connected to a CCD spectrometer to determine the diffraction spectrum. The spatial dependence of the magnetic field was measured by using a Hall probe.

This magnetic CCA self assembly involves the phase separation of the superparamagnetic particles into a high volume fraction phase. However, this self assembly must also involve magnetically induced crystal growth to form the highly ordered CCA; similar high volume fraction colloidal dispersions do not form highly ordered CCA due to their high viscosity which prevents annealing. This mechanism is probably similar to that responsible for close packed CCA ordering, which occurs with gravitational settling or with fluid flow close packing CCA assembly[17], where the 111 FCC crystal planes grow out from the surface the particles pack against.

2.4.2 Synthesis of Ferromagnetic Colloidal Particles

Ferromagnetic composite colloidal particles were synthesized by emulsion polymerization, using methods similar to those used to synthesize our mesoscopic superparamagnetic particles.[11,12] First, ~20 nm Co-ferrite particles were formed by coprecipitation of $CoCl_2$ and $FeCl_3$ (mole ratio 1:2) in a 1 M tetramethylammonium hydroxide (TMAOH) solution.[14,15] These Co-ferrite particles were incorporated within polystyrene colloidal particles by emulsion polymerization. The resulting monodisperse ferromagnetic particles were harvested with a magnet (~10 %

Figure 12. Magnetic field induced packing of superparamagnetic particles in different media in a 4.6 KOe magnetic field with a 6.2 KOe cm^{-1} gradient: (A) magnetic assembly from a 5% particle volume fraction NaCl aqueous solution; (B) magnetic self-assembly from 10% particle volume fraction dispersions in ethanol (24.5), methanol (32.6), acetonitrile (37.7), ethylene glycol (38), DMSO (46.6), and water (78). The dielectric constant of each solvent is given in parentheses.

yield). X-ray diffraction indicates that the cobalt ferrite nanocrystals are in an inverse spinel structure. Fig. 13 shows the TEM images of ~120 nm (polydispersity 7%, Figure 1A) and ~154 nm (polydispersity 6%, Figure 1B) ferromagnetic particles. The nanoscale cobalt ferrite particles appear as black inclusions in TEM images. The cobalt ferrite loading is obviously smaller in the 154 nm (Figure 13B) particles. Although the mesoscopic polystyrene ferromagnetic composite particles are reasonably monodisperse, the TEM indicates significant polydispersity in the cobalt ferrite loading.

Figure 13. TEM image of ferromagnetic polystyrene composite particles containing cobalt–ferrite nanoparticles. (A) TEM image of 120 nm composite particles with a size polydispersity of 7%. The particles contain 14 wt% cobalt ferrite. (B) TEM image of 154 nm composite particles with a size polydispersity of 6%. The particles contain 5 wt% cobalt ferrite. The cobalt ferrite particles appear as black dots inside the composite particles.

We used a SQUID magnetometer to measure the magnetic properties of these particles at room temperature. For a dried powder of the ~ 120 nm particles, we observe hysteresis that demonstrates ferromagnetism (Figure 14), a saturation magnetization, M_S at 50 kOe of 7.2 emu/g (7.0×10^{-15} emu/particle), a remanent magnetization of 1.7 emu/g (1.6×10^{-15} emu/particle). The remanent magnetization persists indefinitely. For the ~154 nm particles, we observe a saturation magnetization M_S of 2.5 emu/g (4.9×10^{-15} emu/particle) and a remanent magnetization of 0.55 emu/g (1.0×10^{-15} emu/particle). Given the 51 emu/g measured saturation magnetization of a powder of our nanoscopic Co-ferrite particles, we calculate a 14 wt % cobalt ferrite fraction in the 120 nm particles, and a 5 wt% cobalt ferrite fraction in 154 nm composite particles.

Figure 14. Magnetic behavior of a dried powder and a deionized water dispersion (1.6 wt%) of 120 nm ferromagnetic particles. The magnetization observed was normalized to the saturation magnetization (M_S) observed at 50 kOe. The powder magnetization curve clearly shows hysteresis, while the solution dispersion does not. The larger reduced magnetization (M/M_S) observed for the liquid dispersion presumably results from the ability of these particles to orient with their easy magnetic axes along the field.
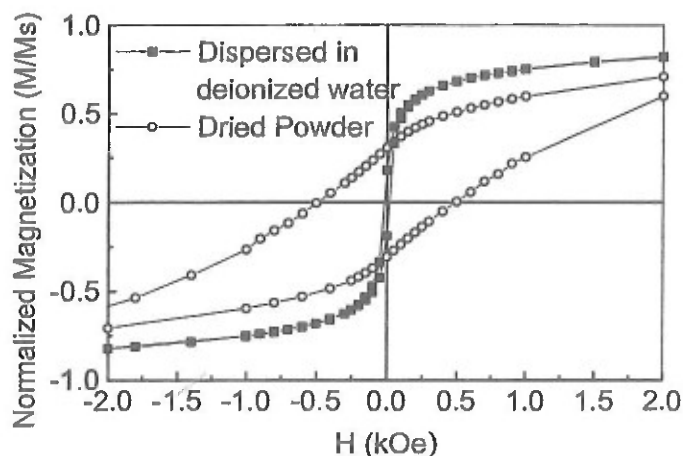
2.4.3 Magnetically Controlled Orientation of Single Ferromagnetic Particles

Inhomogeneous magnetic fields generate translational forces on all magnetic particles[18], while homogeneous magnetic fields induce physical torques only on ferromagnetic particles. This torque attempts to rotate the particles to align their magnetic moments along the magnetic field. In contrast, superparamagnetic particles show only Néel rotation, where the magnetic moments of the particles rotate, but not the particles themselves. In a superparamagnet, Néel rotation is rapid relative to the measurement time, but in small ferromagnetic particles Brownian rotation predominates.[18]

The Fig. 14 room temperature hysteresis occurs because the magnetic torque is insufficient to reorient the entire sample and Néel relaxation in the ferromagnet is negligibly slow. In contrast, no hysteresis is observed for these same particles in a 1.6 wt% aqueous dispersion at room temperature (Figure 14), because they rapidly rotate and align with the field within the measurement time. The larger reduced magnetization (M/M_S) observed for the liquid dispersion compared to the powder results from the ability of spheres to rotate until their easy magnetic axes lie parallel to the field.

Thus, a strong magnetic field induces a permanent magnetic moment in these particles. A weaker magnetic field can then act on this moment to control the orientation of these ferromagnetic particles. We demonstrated this by coating the ~ 120 nm ferromagnetic particles with a thin silica shell[19] and then drying these ferromagnetic particles on a substrate. A permanent magnetic moment was induced in these particles by applying a 6 kOe magnetic field normal to the substrate plane. The north pole of each sphere was labeled by sputtering gold onto the exposed north pole surfaces[20].

These labeled spheres were then redispersed into deionized water and a drop of this dispersion was dried onto a TEM grid in a homogeneous 300 Oe magnetic field, either oriented within the TEM grid plane or normal to it. TEM measurements of the particles (Figure 15 A and B) clearly show that the 300 Oe magnetic field rotates the ferromagnetic particles to orient their

Figure 15. Demonstration of magnetically controlled orientation of magnetized ferromagnetic particles. The magnetized ferromagnetic particles are labeled with a gold patch on their north pole. An aqueous drop containing the magnetized particles was dried onto the TEM grid in the presence of a 300-Oe magnetic field. (A) The magnetic field was oriented as shown within the TEM grid plane. The outward normals to the gold patches orient along the magnetic field direction. (B) The magnetic field was oriented normal to the TEM grid plane, pointed toward the observer. The outward normals to the gold patches point towards the observer.
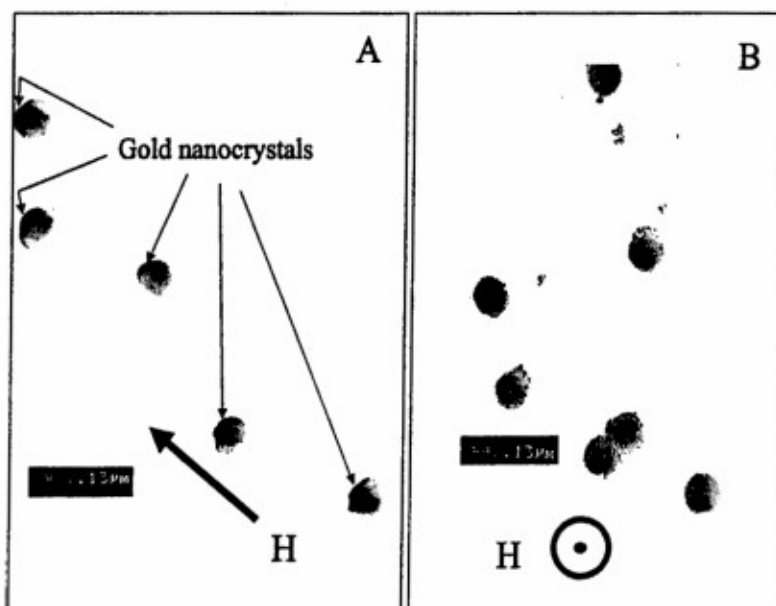
magnetic moments along the applied magnetic field. Figure 15A shows that the spheres orient with the outward normals to the gold patches pointing toward the upper left corner, in the direction of the applied field. When the magnetic field is normal to the TEM grid plane, the gold patches orient with their normals towards the observer (Figure 15B).

2.4.4 Fabrication and Response of Ferromagnetic Photonic Crystals to External Magnetic Fields

Our monodisperse ferromagnetic colloidal particles can be induced to magnetically self assemble into CCA in a manner similar to that demonstrated for our superparamagnetic particles.[11,12] This magnetic self assembly is induced by placing a magnet next to a cell containing magnetic particles; the particles are attracted by the magnetic field divergence and slowly pack into a three dimensional array against the wall of a container. Because the particles have a large surface charge they also spontaneously self assemble into a fcc CCA photonic crystal in low ionic strength aqueous solution, due to the strong electrostatic repulsion between neighboring particles.[1] These photonic crystals can be transiently magnetized by a strong magnetic field; the CCA will possess a macroscopic magnetic moment due to the summed contribution of the magnetic moments of the individual ferromagnetic colloidal spheres of the CCA. However, the magnetization quickly dissipates due to the free rotations of the spheres within the CCA.

However, we can create a macroscopically magnetized photonic crystal by polymerizing a CCA of ferromagnetic particles into a hydrogel (PCCA) to lock the position and orientation of these particles relative to one another. We should observe a net magnetization of the ferromagnetic PCCA such that magnetic fields can now be used to control the orientation of this ferromagnetic photonic crystal in order to control the wavelength of light diffracted by the photonic crystal.

For example, we self assembled ~154 nm monodisperse high surface charged ferromagnetic polystyrene particles (5 wt% Co-ferrite) into a CCA which we then polymerized into a ~ 35 μm thick acrylamide hydrogel PCCA film.[2] The PCCA fcc 111 planes, which orient parallel to the plane of the PCCA film, has a lattice spacing such that it Bragg diffracts 540 nm normally incident light. We used a 3 kOe magnetic field to magnetize the PCCA such that its magnetic moment was oriented normal to the PCCA film. We then shredded this PCCA into small fragments (~100 μm× ~100 μm× 35 μm). Each PCCA fragment possesses a macroscopic magnetic moment due to the summed contribution of the magnetic moments of the individual ferromagnetic colloidal spheres.

We measured the diffraction from this PCCA film dispersion by using a nine-around-one fiber optic probe. Incident white light from the central fiber is back diffracted by the PCCA fragments and collected by the nine surrounding fibers. In the absence of a magnetic field we only detect weak diffraction from the small number of fragments fortuitously oriented with their 111 directions almost parallel to the fiber optic probe.[21] Application of a magnetic field orients the fragment normals parallel to the fiber optic probe axis; the diffracted intensity increases with the magnetic field strength.

As shown in Fig. 17, the diffraction depends on the magnetic field strength and orientation. At the lowest frequencies (<1Hz), the fragments can fully orient with the field direction within each cycle; thus, a maximum modulation occurs for the diffracted light. At 1 Hz we observe both a slow and fast rise time within each cycle. These two rise times probably result from a bimodal population of fragment sizes; the smaller fragments completely and promptly orient, while the largest fragments do not have sufficient time to fully orient. Higher frequency modulations (>4 Hz), do not permit fragments to fully orient; thus the modulation depth of the diffraction decreases (Figure 17).

Figure 16. Response of ferromagnetic composite PCCA fragments to an external magnetic field. In the absence of a magnetic field, the fiber optic probe only detects weak back diffraction from the small number of fragments fortuitously oriented with their 111 directions parallel to the fiber optic probe. Application of a magnetic field orients the fragments with their normals along the fiber optic probe, which results in an increased diffraction intensity. The small magnetic field induced diffraction wavelength blue shift occurs because the magnetic field was not exactly parallel to the fiber optic axis.
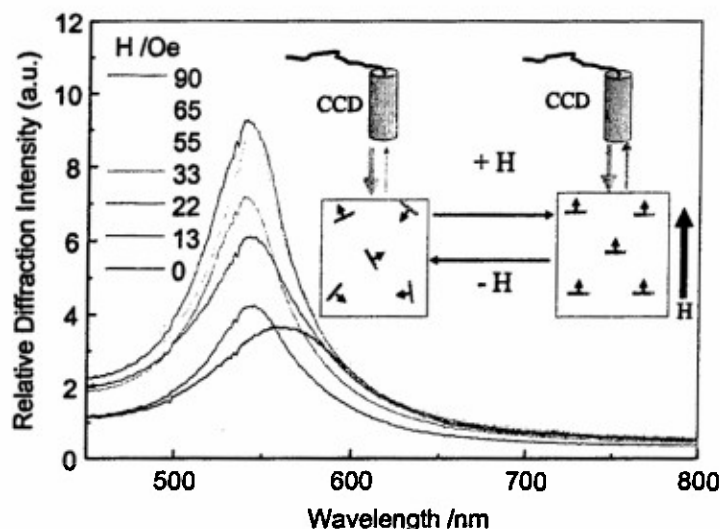
Figure 17. shows the response of this magneto-optical fluid to a periodically varying magnetic field. A 543.5 nm He-Ne laser beam was incident as shown, and a fiber optic was oriented such that it collected the diffracted light at a Bragg glancing angle of ~75°. This diffraction occurs only for those photonic crystals fragments oriented such that their normals bisected the angle between the incident and diffracted beam. One electromagnet gave a constant $H_1 = 75$ Oe field along the sample cell normal, while another magnet imposed a perpendicular magnetic field, H_2 which oscillated as a step function between zero and 30 Oe. This resulted in a net magnetic field direction whose orientation periodically switched between being along the sample cell normal and 22° from the normal. The ferromagnetic photonic crystals fragments reorient in response to the oscillating field which results in oscillating diffraction intensity.

16
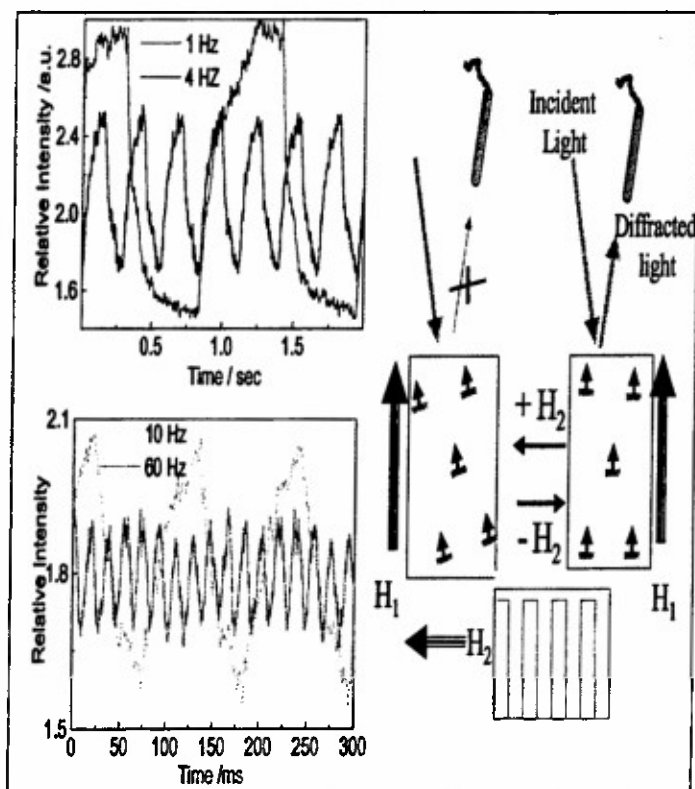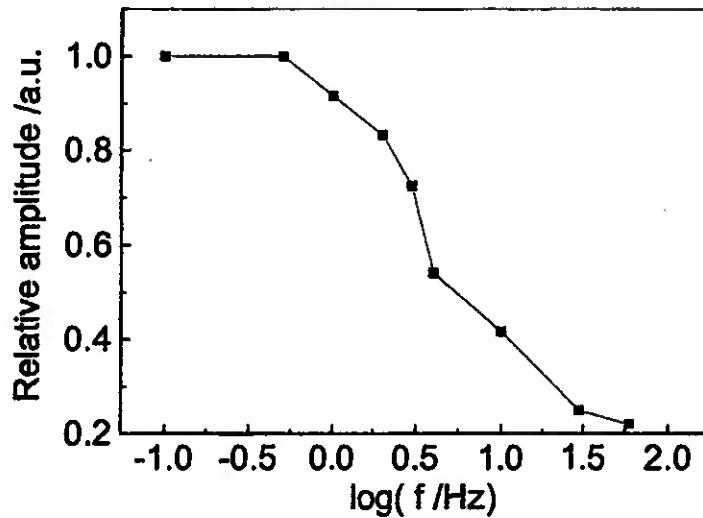
Figure 18. Dependence of the magnetically induced diffraction intensity modulation on the magnetic field switching frequency.

This dispersion of ferromagnetic photonic crystal fragments acts as a magneto-optical fluid whose diffraction and transmission is controlled by incident magnetic fields. The maximum response rate observed was slightly greater than 70 Hz (Fig. 18). This response rate is determined by the reorientation rate which depends upon the magnetically induced torque and the rotational friction. The response rate is expected to dramatically increase as the ferromagnetic photonic crystals fragment size decreases.

We also fabricated a reversible photonic crystal mirror by gluing together two ferromagnetic PCCA (2 × 5 × 0.2 mm) with different fcc lattice constants. These PCCA diffract 549 nm and 686 nm light incident perpendicular to their 111 planes. We then magnetized this photonic crystals laminate with a 3 kOe magnetic field oriented within the PCCA 111 planes. This laminate was sufficiently thick that we were able place this film on the surface of water, with the PCCA 111 plane normal lying parallel to the plane of the water surface. This film could only rotate about an axis normal to the water surface.

Figure 19 shows the magnetic field orientation dependence of this PCCA film diffraction observed by our nine-around-one fiber optic probe, whose axis was oriented within the plane of the water surface, and normal to external magnetic field direction. The left panel shows that a magnetic field can control the PCCA film orientation and can switch the surface of the film facing the fiber optic probe. When the magnetic field points to the left, we observe diffraction of 549 nm light. A 180^0 reversal of the magnetic field rotates the PCCA film such that the other PCCA face diffracts 686 nm light. The diffraction efficiency increases as the field strength increases from 9 to 20 Oe, due to the increased in the alignment of the film. This is most clearly shown in the right panel of Figure 19, which shows the dependence of the diffraction wavelength and intensity as a function of the magnetic field strength.

17
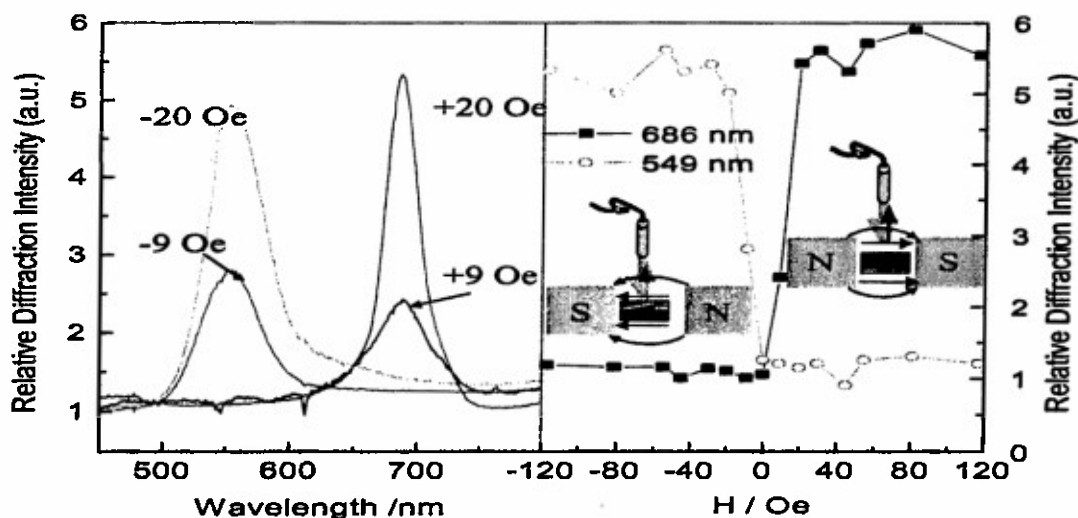
Figure 19. Response of ferromagnetic composite PCCA to a magnetic field. Two PCCA with different lattice constants were glued together with their 111 planes parallel. The PCCA magnetic moment was aligned to lie within the 111 plane. The PCCA film was suspended on a water surface, with the magnetic moment and both PCCA 111 plane normals parallel to the water surface. The figure shows the experimental configuration viewed from the top; the CCD fiber optic was oriented within the plane of the water surface and normal to the magnetic field. If the magnetic field points to the left, the PCCA Bragg diffracts ~ 549 nm light. If the magnetic field is reversed, the PCCA Bragg diffracts ~ 686 nm light.

2.4.5 Conclusions: Magnetically Controllable Colloidal Particles Enable the Construction of Novel Colloidal Assemblies for Electro-optics and Other Technologies

These magnetic particles allow magnetic field control of particle orientation and position. We wish to now develop methods to create chemically reactive patches on the sphere surfaces; although the particles retain spherical symmetry we can create magnetic anisotropies that allow us to coat different parts of their surface. We can orient one face of a particle for reaction and then reorder the particles for another reaction. We can create complex chemically reactive patches.

These chemically reactive patches enable the creation of particles which will react with one another to form functional objects. These particles can be endowed with "valence and reactivity". We envision building a "Periodic Table of the Particles". These particles will function as "elements" with characteristic valence and reactivity. When these spheres are mixed together they chemically self assemble to create new functional devices.

We also envision synthesizing electronically conductive patches on the sphere surfaces. By using a magnetic field we can both orient and cause the spheres to contact one another to create anisotropic switchable electrical circuits where electron flow can be controlled by the magnitude and direction of external magnetic fields.

2.5 Development of Methods to Synthesize Chemically Anisotropic Colloidal Particles.

2.5.1 Summary of approach

The Wilcox group has pioneered direct chemical methods to create chemically distinct regions on the surface of polystyrene microspheres. These methodologies were designed to be scalable so that, although the proof of concept work was carried out with 10 micron spheres, the processes could be applied to spheres of 100 nm diameter. We synthesized benzophenone derivatives for use in colloid surface mediated chemical functionalization and have successfully demonstrated that photoactive agents can be used to create chemically distinct regions on polystyrene microspheres.
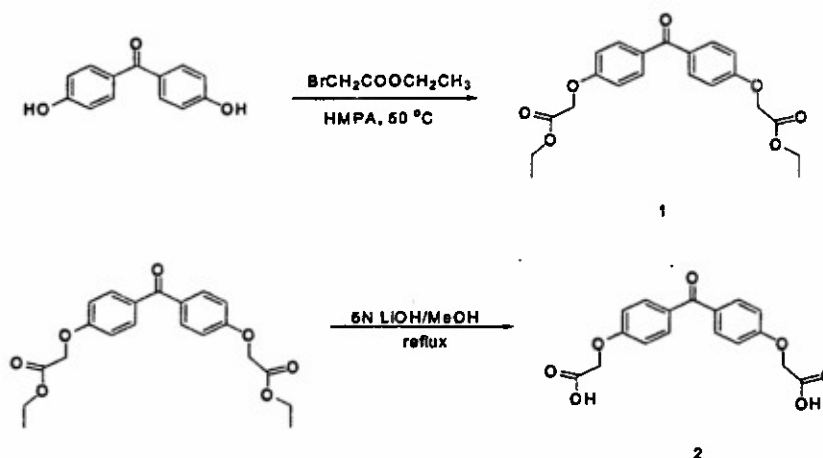
Our strategy for polystyrene sphere functionalization was based on the hypothesis that a thin coating of this photoactive molecule (2) on a quartz plate could be overlaid with a coating of microspheres, and only the part of the microspheres in contact with the coating would react during photoexcitation of the benzophenone (Fig.20).

We examined spin-coating and dip methods for applying the spheres to the coated plates, but found that the best method was to apply a measured volume of colloid suspension to the plate and to then spread the drop by covering the first plate with a second optical flat. The required volume of the drop could be calculated based on the known diameter of the microspheres and the area of the plates (Figure 21).
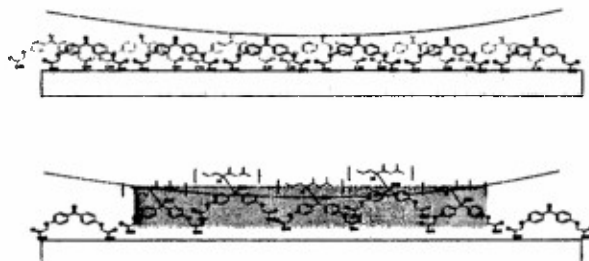
Figure 20. Surface localized chemical
modification of a microsphere.
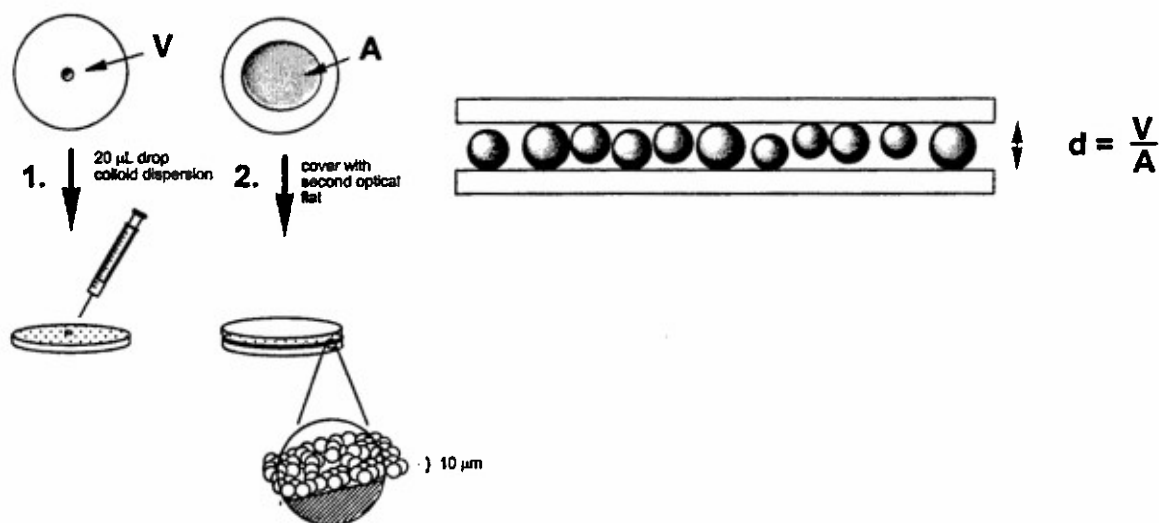
Figure 21. Preparation of the coated quartz plate for irradiation.

Plates prepared in this way were irradiated at 350 nm and after irradiation the modified microspheres were resuspended in water. The overall process is illustrated in Figure 22.
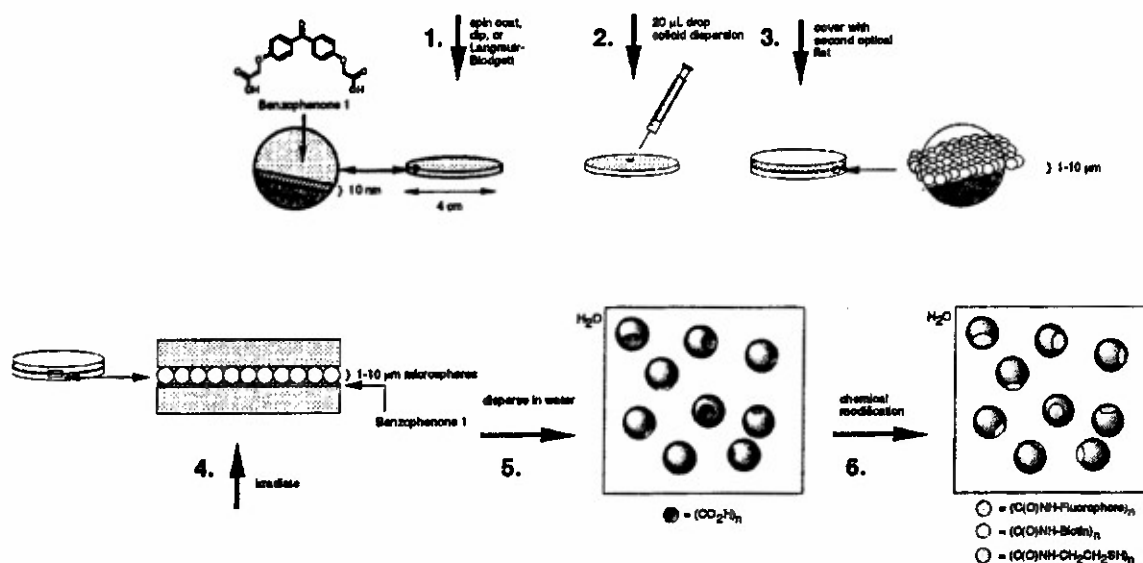
Figure 22. Overall process for chemical modification of microspheres.

We used EDAC in aqueous dispersions of the colloid particles in the presence 5-(aminoacetamido)fluorescein (fluoresceinyl glycine amide, Figure 23) to achieve the coupling. The methods developed for cleaning the microspheres and inducing the coupling are described in detail below in the experimental section.

Figure 23. Fluoresceinyl glycine amide.
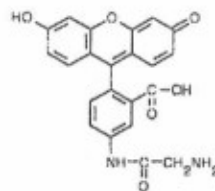
The spheres created in this manner were examined by optical microscopy. The left hand image (Figure 24) is of a 10 μm sphere that has been labeled with a 1.5 μm patch of fluorophore. The microsphere is in contact with the glass cover slip, and at the point of contact (3) light scattering from the surrounding water is eliminated. The functionalized patch (1) is to the left of the contact point. The microsphere does not present a perfectly circular outline. This may be due to optical distortion or may be a real result of the processing. With some production runs we did observe deformation of the spheres that we attribute to heating of the microspheres during irradiation.

- **Image Analysis**
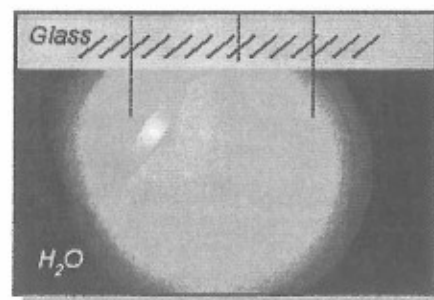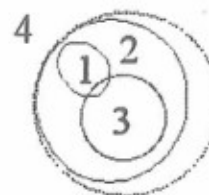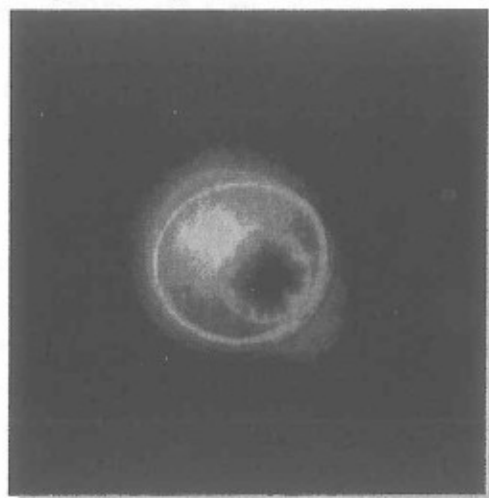
Figure 24. Fluorescence microscopy image of a chemically anisotropic microsphere.

2.5.2   Procedure for the Preparation of Chemically Anisotropic Colloid Particles.

2.5.2.1 Materials.

Polystyrene Microspheres were purchased from Polyscience Inc. Beads were of 1 μm, 6 μm, or 10 μm diameter and were obtained as 5% aqueous suspensions having mainly sulfate groups at the surface. The number concentration of the 10 μm beads was 4.55×10^7 particles per mL and for the 1-micron beads the concentration was 4.55×10^{10} particles per mL. Quartz plates (2-inch diameter, A-1 QTZ WINDOW) were purchased from Esco Products Inc. Biotech Cellulose Ester Dialysis Membrane MWCO 1×10^6 was

purchased from Spectrum Company. 5-(Aminoacetamido)fluorescein (fluoresceinyl glycine amide) and 1-ethyl-3-(3-dimethylaminopropyl)carbodiimide hydrochloride (EDAC) were purchased from Molecular Probes. Deuterated solvents were obtained from Cambridge Isotope Laboratories, Inc. Thin layer chromatography (TLC) was performed using E. Merck silica gel 60F-254 (0.25 mm) analytical glass plates. Silica gel columns for flash chromatography, according to the method of Still,[1] were prepared with E. Merck silica gel 60 (230-240 mesh ASTM).

Dry solvents were distilled shortly before use from an appropriate drying agent under nitrogen atmosphere. Tetrahydrofuran (THF) and diethyl ether (Et$_2$O) were distilled from sodium and benzophenone. Dichloromethane and benzene were distilled from calcium hydride. Dry methanol was distilled from magnesium turnings and stored under nitrogen. Ethyl acetate was dried over 4 Å molecular sieves for at least 24 hours prior to use. Dimethylformamide (DMF) was dried over MgSO$_4$, distilled under reduced pressure, and stored over 4 Å molecular sieves. Pyridine was distilled from calcium hydride and stored over 4 Å molecular sieves. Hexane refers to the mixed hydrocarbon fraction (bp 68-70 °C), principally n-hexane, and was purified as follows: the commercial solvent was stirred over concentrated H$_2$SO$_4$ for at least 24 hours, decanted, stirred over anhydrous NaHCO$_3$ for at least 6 hours, decanted, and distilled. Benzene, methylene chloride (CH$_2$Cl$_2$) and triethylamine (TEA) were distilled from CaH$_2$. Other commercially available reagents and solvents were reagent grade and were used without further purification. Alkyllithium reagents were titrated according to Juaristi's procedure prior to use.[2]

2.5.2.2 General Procedures.

Fluorescence microscopy was carried out using a Nikon Eclipse E800 laser scanning fluorescence microscope equipped with confocal Biorad Radiance 2000 stage. Proton (^{1}H NMR) and carbon (^{13}C NMR) nuclear magnetic resonance spectra were recorded on Bruker Avance 300 and Bruker DRX 500 spectrometers at 300 MHz and 75 MHz, and 500 MHz and 125 MHz, respectively. Chemical shifts (^{1}H-NMR and ^{13}C-NMR) are expressed in parts per million (δ units) downfield from tetramethylsilane (TMS). The solvent peak was used as the reference value. For ^{1}H NMR: CDCl$_3$ = 7.27 δ; DMSO-d_6 = 2.49 δ; acetone-d_6 = 2.05 δ. For ^{13}C NMR: CDCl$_3$ = 77.23 δ; DMSO-d_6 = 39.51 δ. For the proton data: s = singlet; d = doublet; t = triplet; q = quartet; dd = doublet of doublets; dq = doublet of quartets; m = multiplet; br = broad; app = apparent. Low and high resolution mass spectra were recorded on a VG 7070 spectrometer. Infrared (IR) spectra were collected on a Mattson Cygnus 100 or an IBM IR/32 spectrometer. Melting points were determined using a Thomas Hoover capillary melting point apparatus and are uncorrected. UV-Vis spectra were recorded on a Hewlett-Packard 8451A Diode Array Spectrophotometer.

Reactions run under a nitrogen atmosphere were arranged with a mercury or oil bubbler so that the system could be alternately evacuated and filled with nitrogen and left under positive pressure. Syringes and reaction flasks were dried in an oven at 120 °C and cooled in a desiccator over calcium sulphate prior to use. Reactions at "room

temperature" were conducted under ambient laboratory conditions: T = 20-27 °C, p = 720-770 mmHg. References to "removal of solvents under reduced pressure" refer to rotary evaporation of the sample at 25-65 °C under reduced pressure (18-25 mmHg), sometimes followed by removal of residual volatile materials under vacuum (0.05-0.5 mm Hg) at room temperature. Yields are reported based on the amount of isolated material obtained after the indicated procedure. The purities of these products were each determined by ^{1}H-NMR and are greater than 95% unless otherwise noted.

2.5.2.3 [4-(4-Ethoxycarbonylmethoxy-benzoyl)-phenoxy]-acetic acid ethyl ester (1).

To a solution of 0.106 g (0.467 mmol) of dihydroxybenzophenone and 0.3 g (0.934 mmol) cesium carbonate in 2 mL of hexamethylphosphorictriamide (HMPA) under nitrogen at 50 °C was added, with stirring, 0.17 g (1.028 mmol) of ethyl bromoacetate . The resulting mixture was stirred at 50 °C for 18 h. Analysis by TLC (CH$_2$Cl$_2$/EtOAc, 4:0.1) on silica gel revealed appearance of a new product with R$_f$ = 0.4. After cooling to room temperature the mixture was poured into 500 mL of ice cold water. The resulting precipitate was filtered off, washed with 25 mL of 5% sodium hydroxide and 2 x 50 mL portions of water. The residue was dried under high vacuum to yield 0.153 g (85% yield) of compound 1 as a white powder: ^{1}H NMR (CDCl$_3$, 300MHz, ppm) δ 1.32 (t, 6H, CH$_3$), 4.32 (q, 4H, CH$_2$), 4.71 (s, 4H, CH$_2$), 6.98 (dd, 8.8 Hz, 1.9 Hz, 4H, Ph), 7.80 (dd, 8.8 Hz, 1.9 Hz, 4H, Ph); ^{13}C NMR (CDCl$_3$, 300 MHz, ppm) δ 14.20 (-CH$_3$), 61.70 (-CH$_2$CH$_3$), 65.29 (Ph-O-CH$_2$-), 114.18, 131.56, 132.32, 161.03 (Ph), 168.45 (C=O), 194.29 (C=O);
IR (CHCl$_3$, cm^{-1}): 1755, 2305, 2978, 3057.

2.5.2.4 [4-(4-Carbomethoxy-benzoyl)-phenoxy]-acetic acid (2).

A solution of ester 1 (0.104 g, (0.269 mmol) in 2 mL of 5N LiOH/MeOH (5/1) was refluxed for 27 hours. The reaction mixture was cooled to room temperature and then acidified by addition of 15 mL 1N HCl. The precipitate was removed by filtration and washed with 3 x 50 mL water. The material obtained was dried under high vacuum to yield compound 2 (0.088 g; 96% yield) as a white solid: mp 233-235 °C; ^{1}H NMR (CDCl$_3$, 300 MHz, ppm) δ 4.77 (s, 4H, CH$_2$), 7.04 (d, 8.7 Hz, 4H, Ph), 7.68 (d, 8.8 Hz, 4H, Ph), 13.15 (s, 2H, COOH); ^{13}C NMR (DMSO, 300 MHz, ppm) δ 64.99 (Ph-O-CH$_2$-), 114.75, 130.84, 132.24, 161.50 (Ph), 170.29 (C=O), 193.58 (C=O); MS: calculated 330; found 330

2.5.2.5 Single Spot Functionalization.

A quartz plate 2 inches in diameter was dip coated with a 0.005 M solution of benzophenone analog 2 and allowed to air dry in a container covered with aluminum foil to exclude light. A 40 μL aliquot of the 10 μm Polybead suspension was gently introduced and spread evenly on one surface of a second quartz plate. The plate coated with benzophenone was gently placed over the beads on the second quartz plate. The beads are thus positioned between two quartz plates with only one side in contact with benzophenone. The two plates were clamped together and placed in a Rayonet

23

Photochemical Reactor containing 350 nm UV lamps and were irradiated for 1 h. The beads were then suspended in 0.3 mL of water by sonication. The bead suspension was washed with 4 x 2 mL portions of water on a 0.45 micron pore size PVB membrane (filtration by centrifugation). The beads were re-suspended in 0.3 mL of water in a vial and to this suspension was added 5(aminoacetamido)fluorescein (fluoresceinyl glycine amide) (0.67 mg, 1.65 x 10^{-3} mmoles), EDAC (4.92 mg, 2.58 x 10^{-2} mmoles) and 1 mL of pH 5 phosphate buffer solution. The mixture was allowed to stir for 24 hours and then washed with 5 x 2mL portions of water on a PVD Durapore membrane, 0.45-micron pore size (filtration by centrifugation). Examination of these microspheres by fluorescence microscopy shows that approximately 30% of the microspheres had fluorescent patches. The patch size was uniform and of about 1.5 μm in diameter. (Figure 25)

Figure 25. Photomicrographs of modified 10 micron polystyrene sphere.
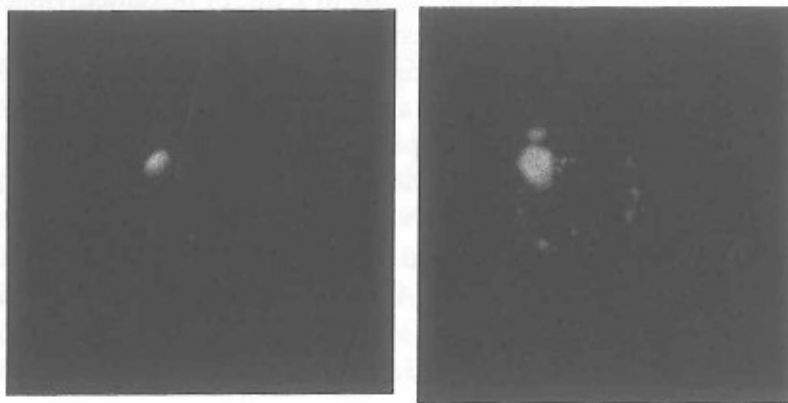
2.5.2.6 Two-Sided Functionalization. Two quartz plates 2 inches in diameter were each dip coated with a 0.005 M solution of the benzophenone 2. The quartz plates were placed in a container covered with aluminum foil to air dry. A 40 μL aliquot of the 10 μm Polybead suspension was gently introduced and spread evenly on one surface of a second quartz plate. The plate coated with benzophenone was gently placed over the beads on the second quartz plate. The beads are thus positioned between two quartz plates with only one side in contact with benzophenone. The two plates were clamped together and placed in a Rayonet Photochemical Reactor containing 350 nm UV lamps and were irradiated for 1 h. The beads were then suspended in 0.3 mL of water by sonication. The bead suspension was washed with 5 x 2 mL portions of water on a PVDf Durapore 0.45 micron pore membrane. The beads were re-suspended in 0.3 mL of water and to this suspension was added 5(aminoacetamido) fluorescein (fluoresceinyl glycine amide) 0.67 mg (1.65 x 10^{-3} mmoles), EDAC 4.92 mg (2.58 x 10^{-2} mmoles) and 1 mL of a pH 5 phosphate buffer solution. The mixture was allowed to stir for 24 hours and then washed with 5 x 2mL portions of water on a PVD Durapore membrane, 0.45-micron pore size (filtration by centrifugation).

Control experiment. A 40 μL aliquot of the 10 μm Polybead suspension was gently introduced and spread evenly on one surface of a quartz plate and a second plate was gently placed over the beads. The two plates were clamped together and placed in a Rayonet UV reactor containing 350 nm UV lamps. The plates with the contents were irradiated for 1 hour. The beads were then suspended in 0.3 mL of water by sonication

and washed with 4 x 2 mL portions of water on a PVB, 0.45 micron pore size membrane by centrifugation. The beads were re-suspended in 0.3 mL of water in a vial and to this suspension was added 5(aminoacetamido) fluorescein (fluoresceinyl glycine amide) 0.62 mg (1.53 x 10^{-3} mmoles), EDAC 3.30 mg (1.72 x 10^{-2} mmoles) and 1 mL of phosphate buffer solution pH 5. The mixture was allowed to stir at room temperature for 24 hours and then washed with 5 x 2mL portions of water on a PVDf Durapore membrane, 0.45-micron pore size by centrifugation.

2.5.2.7 Fluorescence Microscope Analysis.

An aqueous suspension of beads was mounted on a microscope slide and DABCO solution in glycerol was added to inhibit photo-bleaching of the fluorescein dye. Fluorescence microscope analysis of the beads obtained from the single side experiment showed a single patch of bright fluorescence on the surfaces of some of the beads. Fluorescence on the surface of the beads indicates partial modification on the bead surface as a result of coupling of the amino portion of the fluorescein dye to the carboxylic group of the benzophenone. The yield is about 30% based on the number of beads with fluorescent patches vs. total number of beads in the field. Only very weak fluorescence was observed on the beads obtained from the control experiment. Two patches of bright fluorescence were observed on some of the beads obtained from the double sandwich experiment. Due to the angle of focus on the microscope the patches of fluorescence appeared as dots opposite to each other. The idea of using the double sandwich method to get the beads in contact with benzophenone at two contact points on the beads appears useful, but multiple fluorescence patches were also observed on some of the beads. Yield for the double sandwich experiment is estimated to be 20% based on the number that are observed to have only two-patch fluorescence. Since control experiment showed no fluorescence on the control beads it can be concluded that single and double patch fluorescence observed in our single and double sandwich experiments indicated a successful partial surface modification of the bead surfaces using benzophenone.

2.5.3 Conclusions Regarding Preparation of Chemically Anisotropic Colloid Particles by Surface Localized Photochemical Reactions.

1.	Photoactivation of quartz-surface localized benzophenone, while the polystyrene microspheres are in contact with the surface, leads to selective chemical modification of the microsphere surface.
2.	The modified surface has an enhanced reactivity toward the EDAC/fluorescein reaction mixture and after thorough washing the microspheres retain a fluorescent patch. We propose that the fluorescein is covalently bound to the microsphere through the carboxylic acid groups of the benzophenone label.
3.	The yield of microspheres is only about 20% (determined by hand counting within the microscope field). The cause of this low yield has not been determined. Lack of reaction of the majority of microspheres could be caused by lack of contact with the surface, by uneven surface coating of the quartz plate by the benzophenone, or by other

unidentified events. The yield must be improved or methods must be developed for separating plain microspheres from functionalized microspheres.

4.   A few exploratory experiments in this project have shown that transmission infrared spectroscopy is a good method for evaluating the coating of the quartz plate with benzophenone. Future work should rely on this or related methods for measuring the uniformity of the coating prior to bead functionalization. Higher spatial resolution could be achieved by near-field infrared microscopy.

5.   Control of the experiment can be improved by construction of a mechanical stage that would control the pressure between the quartz plates and the distance between the plates. This stage should also allow X-Y tranlation of one of the optical plates.

6.   An evaluation of how the yield of modified microspheres is affected by the dispersity of microsphere size should be carried out.

2.6   Theoretical Study of the Dependence of Photonic Crystal Diffraction on Crystal Properties and Defect Structures

We have theoretically investigated scattering of light from crystalline colloid structures. Although the band structure of light propagating through an infinite photonic crystal is well studied[24], the intensities of light diffracted from finite, possibly imperfect chunks of realistic colloidal crystals remains an active area of research.

We have addressed this problem using three different methods. First, we have utilized the 1-D transfer matrix method to model diffraction of light through finite colloidal crystals and compare these theoretical calculations to experimental results obtained by the Asher group. Second, we have developed a full 3-D Finite-Difference Time Domain (FDTD) code to calculate diffraction of light from arbitrary 3-D colloidal systems. Third, we have performed a 3-D numerical integration of light scattered by all individual colloidal particles comprising the finite crystal. We briefly summarize results obtained using each of these methods.

2.6.1   Application of 1-D Transfer Matrix Method

We applied the 1-D transfer matrix method[25] to model the propagation of light through colloidal crystals. Reduction of a 3-D periodic structure to a 1-D set of layers is possible if light propagates in a direction close to the Bragg condition. In this case we can model the particular set of Bragg diffracting crystal planes as a periodic 1-D structure which can be exactly analyzed by the transfer matrix method. This simple method has been suggested for use in experimental data analyses as a replacement for the less accurate dynamical diffraction method[26].

Fig. 26 shows the effect of static disorder on the band gap properties of a photonic crystal. Adding disorder to the positions of individual layers decreases the band gap width compared with that of the perfectly periodic structure.
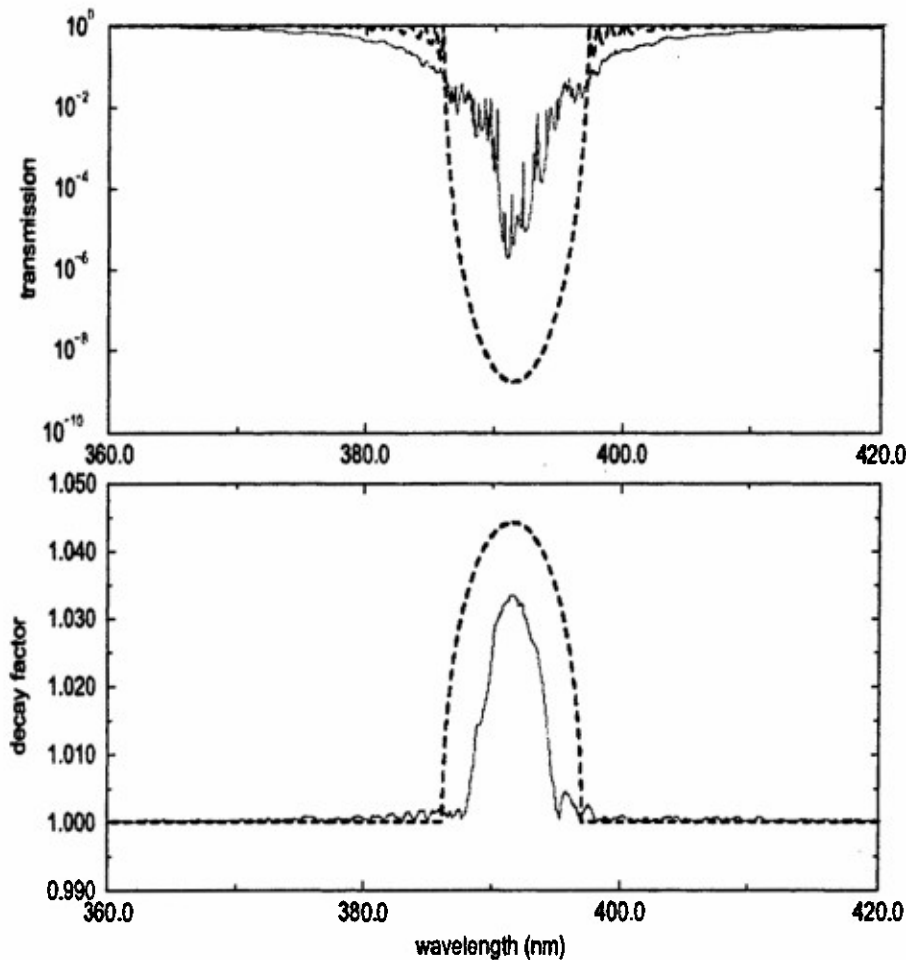
Figure 26. Top figure, dashed line: Calculated dependence of transmission spectrum for 1-D periodic photonic crystal vs frequency of normal incident laser light. The photonic crystal consists of 250 dielectric layers of width 100 nm and 100 nm with corresponding dielectric constants 1.93 and 1.77. Range of frequencies over the first order stop gap is shown. Solid line: Averaged (over 60 runs) spectrum for a disordered photonic crystal. Disorder is included into the widths of the dielectric layers based on uniform random deviations of 10% magnitude. Bottom figure: Decay factor for periodic (dashed line) and disordered (solid line) system.

2.6.2 Application of Finite Difference Time Domain Method

To understand the applicability limits of 1-D theories and provide a full 3-D picture of light scattering from colloidal crystals, we have applied the Finite Difference Time Domain (FDTD) method[27] of numerical integration of Maxwell's equations. We were able to simulate the scattering of light by a 9x9x6 crystal (Fig. 27), which unfortunately is too small to address the properties of realistic colloidal crystals. We believe it is possible to continue developing this approach to analyze much larger systems, but we decided to concentrate on the third method, which provides more flexibility in analyzing light patterns diffracted from arbitrary 3D colloid crystal structures.
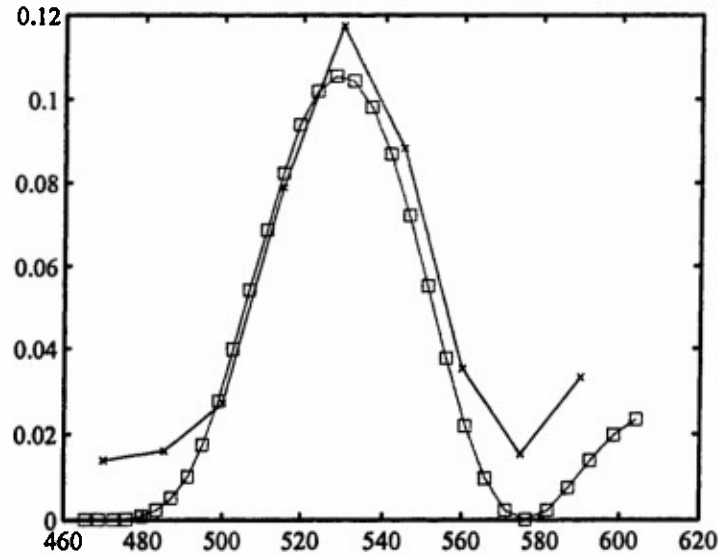
Figure 27. Finite Difference Time Domain (FDTD) simulation results for the scattering of light by a small 9x9x5 crystal. We plot the diffracted light intensity dependence vs the wavelength (in nm) of the incident light: Blue curve (squares)- analytical 1-D result for reflection from 5 layers; red curve (crosses) – FDTD simulations for the 9x9x5, 5 layer colloidal crystal.

2.6.3   Direct Diffraction Mie Scattering Modeling

Recently our analysis of realistic 3-D colloidal crystals has focused on application of Mie theory[28] to analytically calculate light scattering by a single sphere and then sum individual scattering contributions from all particles in the crystal. This method allows us to treat macroscopic systems consisting of thousands of colloid particles and provides a basis for calculating the intensity of light diffracted from colloidal crystals. This method can be used as a reference point in analysis of the applicability of 1-D theories based on transfer matrix method.

In Figure 28 we present a calculation of backward reflected light intensities from [111] planes of an fcc colloidal crystal, for the case of incident light normal to the [111] set of planes. The crystal consists of 18 planes and each plane contains 60x50 identical spheres. Blue solid curve shows the total intensity of exactly backward ("specularly") diffracted light occupying a scattering angle of 5 degrees. Red curve shows the total intensity of all light scattered into the backwards hemisphere.

The advantage of this method of calculation is that it allows us to consider non-perfect fcc crystals containing any sequence of types of individual planes. The distribution of light in 3-D space for light diffracting from the same finite colloidal crystal is presented in Figure 29, for the case of incident light of wavelength 160 nm normal to the (111) planes of the colloidal crystal. This 2-D diffraction pattern, which is typical of light scattered from a finite system comprised of several crystal planes, consists of a central peak (direct backscattering) and 6 peaks around it.
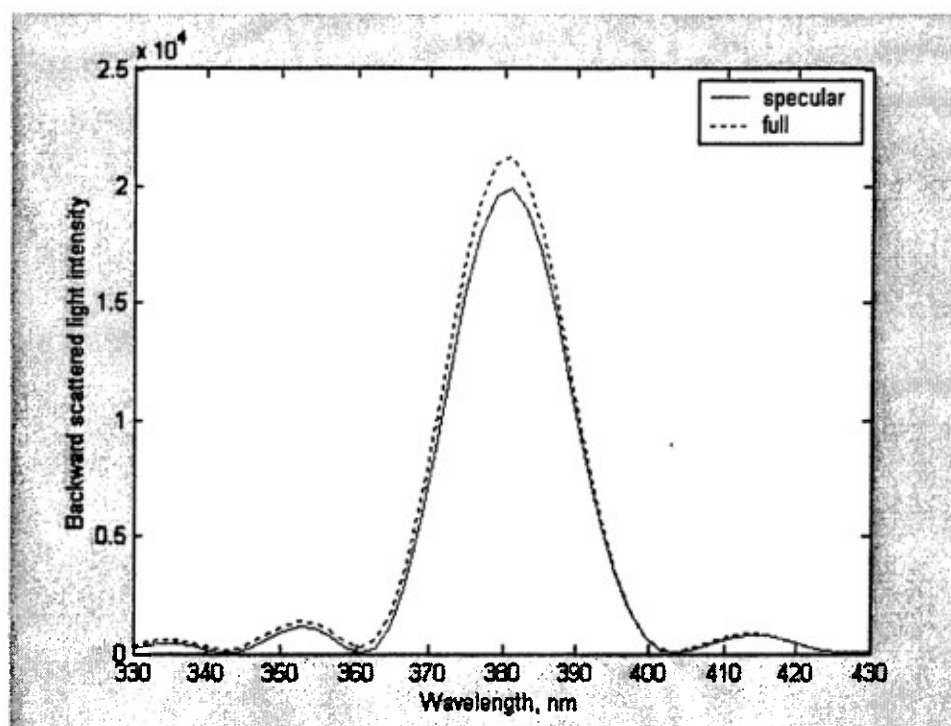
Figure 28. Diffracted light intensity dependence vs wavelength of the normally incident light. The crystal consists of 18 (111) planes. Incident light is normal to this set of planes. Blue (solid) curve represents the specularly diffracted backscattered light, while red (dotted) curve is the total intensity of all backscattered light. The crystal lattice constant is 330 nm, while the diameter of individual colloids is 120 nm.
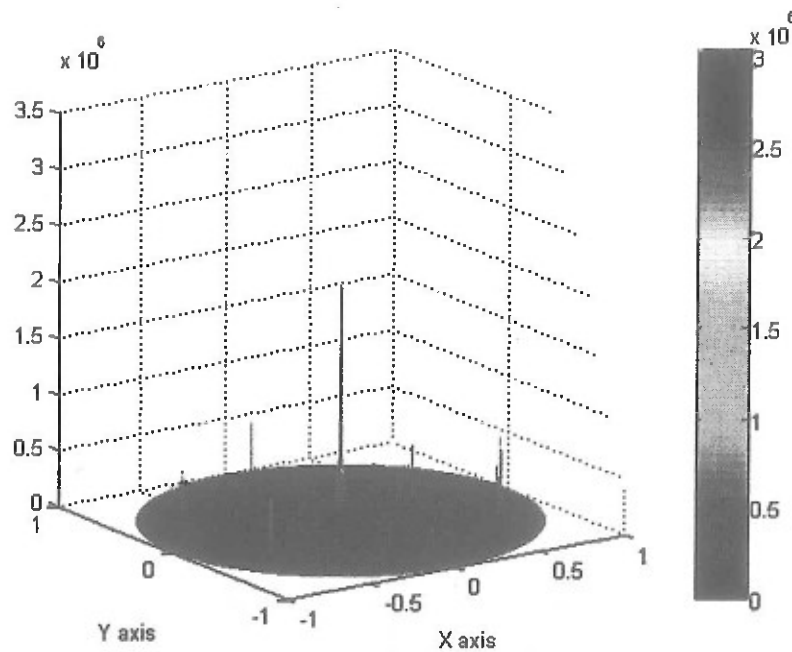
Figure 29. Backward diffracted light intensity distribution for colloidal crystal in 3-D space. Central peak and 6 peaks around it correspond the 2D diffraction pattern from the 18 planes of an fcc crystal. The wavelength of light is 160 nm. Every point of the circle represents a specific direction of backscattered light. The vertical axis indicates scattering intensity.

3.0 Directed Self-Assembly of Ge/Si Quantum Dots

3.1 Introduction

Fabrication methods that can control the three-dimensional structure of semiconducting materials at nanometer scales has very important applications such as, for example, in lightweight, low-power optical displays, visible and infrared imaging devices, laser systems, storage devices and other small, high-density and high-efficiency optoelectronic components. The unique properties of such devices rely on three-dimensional confinement of electronic states in the semiconductor. In recent years, three-dimensional islands of heterogeneous semiconducting materials, known as quantum dots (QDs), grown by self-assembly are essentially free of dislocations and chemical impurities, and therefore have optical and transport properties far superior to those formed by conventional methods such as lithography. But there are many limits to the technique of unguided self-assembly. The size distribution and spacing of QDs are randomized which limits the usefulness of self-assembled QDs for many device applications.

We have worked on developing novel approaches for controlling both the size and spacing of QD structures, based on *directed* self-assembly on a strained wetting layer surface. The system where we use this method is Ge/Si, although the procedure should work equally well for III-V systems such as InAs/GaAs and II-VI systems like CdSe/ZnSe. We take advantage of the coexistence of a metastable 2D phase and an equilibrium 3D phase and locally perturb the surface causing the nucleation of islands only in the region where the surface is being addressed. The local perturbation is achieved by planting C atoms on Si surface with an STM tip. *(For further detailed information about progress toward the growth of quantum dots using the UHV Nanoworkbench, please refer to Section 5.0.)*

A variety of characterization techniques are being employed to determine both the structure and optoelectronic properties of the proposed structures. Atomic force microscopy (AFM) and ANSOM studies, *in situ* scanning tunneling microscopy (STM), plan-view and cross-sectional TEM are employed to determine the three-dimensional structure of the fabricated QDs. The room-temperature and cryogenic AFM studies and photoluminescence measurements are set up in Prof. Levy's lab. Such optical characterization provides a sensitive probe of the size uniformity of the QD structures. Room-temperature and low-temperature near-field scanning optical microscopy are used to characterize individual QDs. Time-resolved studies of both luminescence and transient absorption are measured by using a mode-locked femtosecond laser and high-resolution spectrometer. Such studies provide important information about energy relaxation mechanisms, which are relevant for optoelectronic applications.

31

3.2 Overview of Technology

A great deal of progress has been made concerning the assembly of the single quantum dot spectroscopy system. Fig. 30 shows a functional overview of the integrated system. The system consists of a femtosecond light source (optical parametric oscillator), variable-temperature apertureless near-field scanning optical microscope (VT-ANSOM), and luminescence detection system consisting of a 1/2 meter spectrometer and InGaAs array. The light source is a Spectra Physics Opal system that has been tested and performs reproducibly over a wide range of wavelengths. The VT-ANSOM is a home-built system that has the capability of probing luminescence from single Ge/Si quantum dots.
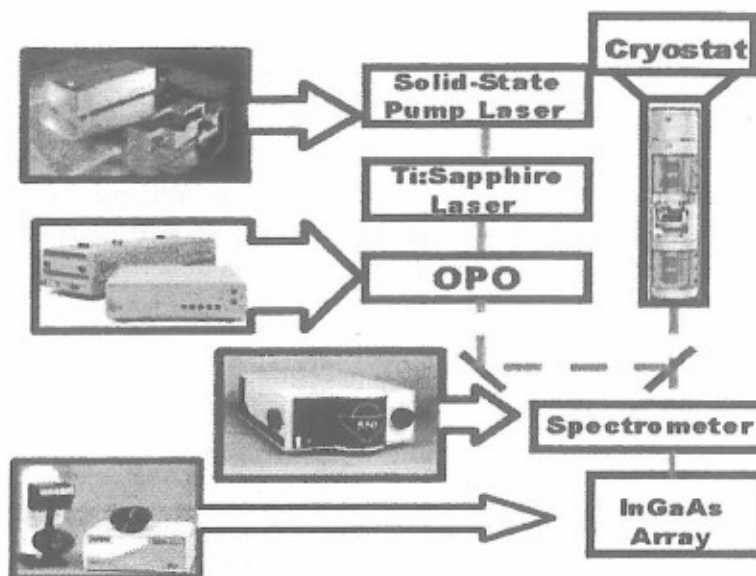
Figure 30. Overview of single quantum-dot spectroscopy system. Clockwise from top left: femtosecond optical parametric oscillator, apertureless near-field scanning optical microscope and optical cryostat; 1/2-meter spectrometer and InGaAs array.

Figure 31 shows a schematic of the method utilized for collecting luminescence. Light is focused from below using a high numerical aperture (40X, NA=0.8) microscope objective to a diffraction-limited spot. Many quantum dots will be excited by the light. To distinguish a single quantum dot, scattered light is detected from a nearby scanning probe tip. By modulating the tip height, it is possible to distinguish luminescence coming from the quantum dot directly below the tip. Luminescence from the quantum dots is directed toward the input port of a spectrometer and detected by a linear InGaAs array. The detection array has a high quantum efficiency (~50%) and exceptionally low noise when cooled by LN_2.
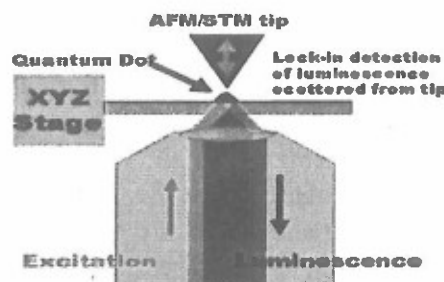
Figure 31. Schematic of method for probing luminescence from single quantum dots.

Aside from assembling the entire system, we have exhaustively tested the sub-components of the VT-ANSOM at room temperature and at cryogenic temperatures. Figure 32 gives a closer look at the completed instrument. The instrument is machined out of solid Macor, a machineable ceramic that combines high rigidity, low thermal expansion and electrical insulation. There are two coarse approach assemblies whose function is essential for the working of the microscope. The lower approach is used to focus the microscope objective (see Fig. 31). The upper approach is used for touching the scanning probe tip onto the sample surface and used in feedback mode to maintain a constant separation between sample and tip. Figure 33 illustrates the mechanism by which the motor functions. A hollow Macor tube is used to hold the object to be moved (in this case the microscope objective). Three sides are
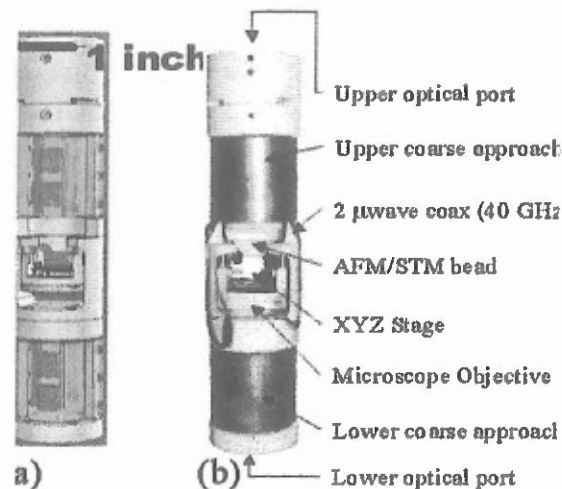
Figure 32. VT-ANSOM. (a) CAD drawing. (b) Completed instrument.
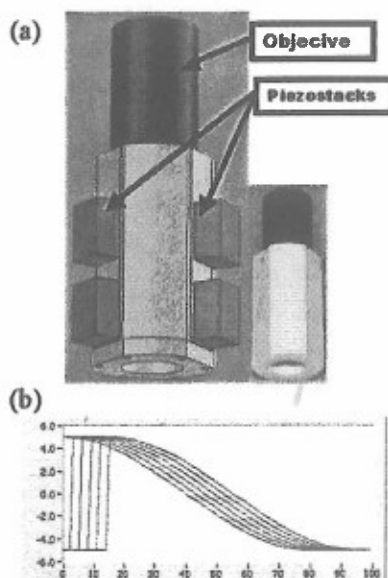
Figure 33. (a) Mechanism for microscope objective coarse approach. Six shear piezostacks (4 shown) slide against a polished Sapphire surface. (b) Voltage sequence used to produce a single step of size 10 nm < dz < 100 nm.

milled flat and fitted with optically polished Sapphire plates. The shaft is held with friction by six piezostacks that are glued into the base of the microscope. Upon application of a voltage to the piezostack, they shear upward (or downward) by a small amount (up to 1 µm). In order to displace the microscope by large distances (up to 10 mm), the six piezostacks are jerked and released in sequence, as shown in Figure 33(b). Each cycle of voltage pulses produces a fixed displacement up or down of the objective, allowing it to be focused.

Getting the motors to work with and against gravity, at room temperature and at cryogenic temperatures, is non-trivial, and it is a tribute to the design that the current system works so well and reproducibly. One hurdle that we have been able to overcome concerns the difference in the thermal expansion of some of the materials used for the stick-slip motors. Initially, the motors could be made to work reproducibly either at room or low temperature, but not over the entire range. To

33

fix this problem, the phosphor-bronze metal sheet which holds the motor together as per the initial design was replaced with a titanium sheet, which is more closely matched with the Macor.   Figure 34 shows the motor step size dz of one of the motors as a function of piezo voltage for two temperatures, 220K and 10K. The reduction in step size with temperature is well understood and arises due to the reduced response of the piezostacks at low temperatures. Most importantly, the motor now works without adjustment at all operating temperatures.

A design of low temperature amplifier has allowed us to use quartz tuning fork oscillators for scanning probe detection at low temperature. Normally, the weak signals from such devices are hard to detect, and are more difficult to use at low temperatures, where large capacitive loads can swamp the signal of interest. A new design using a GaAs HEMT that works from room temperature down to low temperature provides thermal-noise limited performance. Technical details related to this scheme are scheduled to be published in Review of Scientific Instruments.

Another important aspect of the microscope is the scanning stage, which must be small, stable, and able to scan over large areas. Figure 35 shows the design and implementation of our XYZ stage. The sample stage is at present a polished sapphire disk which rests upon three polished half-spheres (~1 mm diameter). Slip-stick methods are used for coarse positioning of the sample in the XY plane, and slower motions are used to scan the sample.
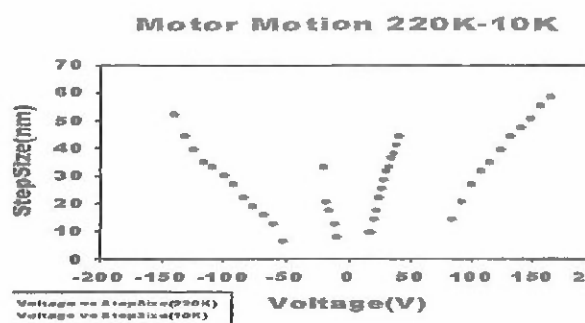
Figure 34.   Graph of step size dz vs. voltage magnitude at two temperatures. Initial results show that tension parameters exist which allow operation at room temperature and cryogenic temperatures without adjustment
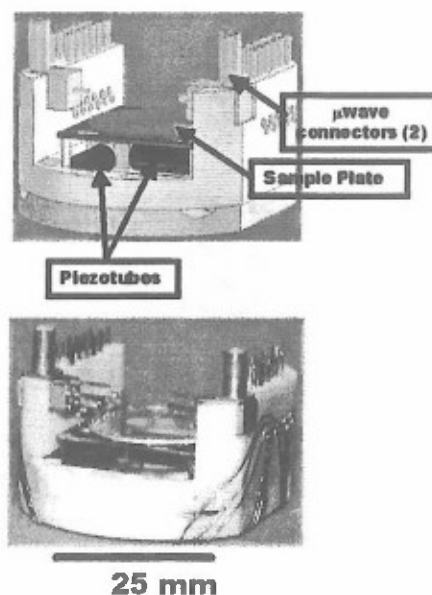
Figure 35. XYZ Stage. (a) CAD drawing. (b) Completed stage.
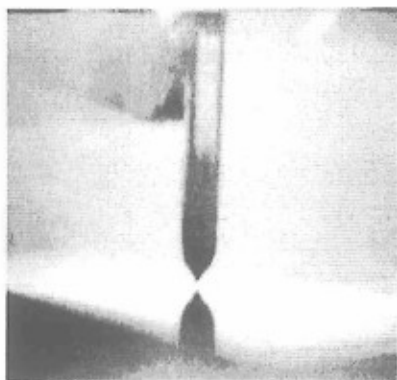
Figure 36. Photograph of sharp Pt-Ir tip mounted on the tuning fork scanning the sample.

A tuning fork, with a scanning tip attached at one end, is oscillated electrically or mechanically at the resonance frequency in order to maximize the sensitivity. When the scanning tip comes into the vicinity of a sample surface, the force gradient of the repulsive atomic force changes the resonance frequency and thus changes the response signal. A phase-locked loop (PLL) can monitor the shift in the resonance frequency of the tuning fork, while providing a fast response time. The output of the PLL is used as feedback signal to maintain a constant distance between the tip and sample and is sent into a commercial scanning probe controller. This equipment outputs the low voltage control signals.
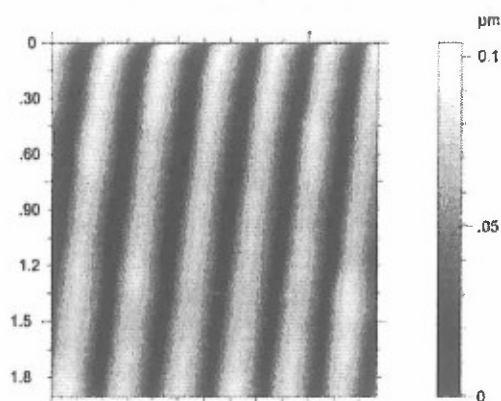
Figure 37. AFM image of 300 nm one dimensional silicon grating at 300 K.

Figure 36 shows an image of the tip scanning the sample. A sharp silicon/ Pt-Ir tip (10 nm tip radius) is glued to the tuning fork end and used as the probe. The stage is raster-scanned in the XY plane under the tip to scan the desired area of the sample. Figure 37 shows tests of the AFM at room temperature. A 300 nm one dimensional silicon grating was used as a test object. The stage can produce scans as large as 6 μm on a side at room temperature. The same grating was also cooled down to T=8 K and scanned. These tests resulted the excellent resolution and scan range of ~1 μm at T=4.2 K. Figure 38 shows an image of the same grating taken at T=8 K. The observed change in the scan range of the stage is due to the reduced piezoresponse of the scan tubes at low temperatures. The resultant calibration for the XY scanning stage is shown in Figure 39. One of the tests we carried out was imaging the self assembled QD with AFM system. Figure 40 shows a room-temperature image of self-assembled a Ge/Si QD sample grown in the UHV nanoworkbench.

Figure 38. AFM image of 300nm one-dimensional silicon grating at 8 K.
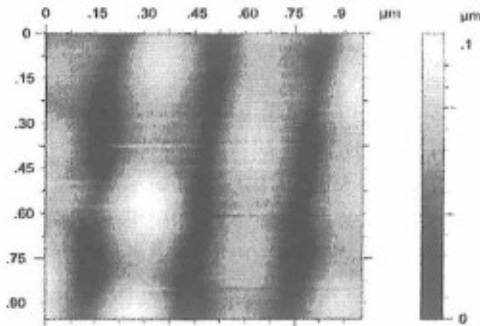
Figure 39. Calibration of the scanning stage for the Low
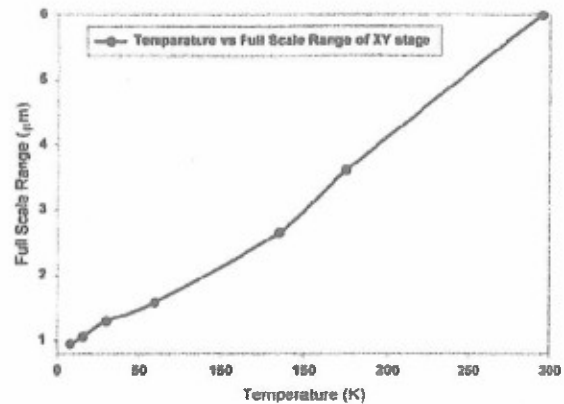
Figure 40. AFM of self assembled quantum dots at room temperature
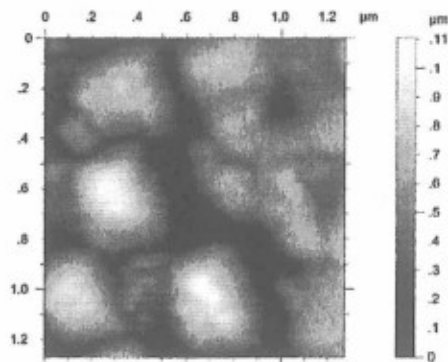
Figure 41. Panels of AFM scanning program.
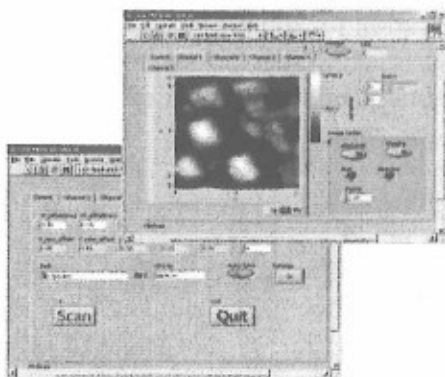
Due to the complexity of the experiments, it is important to be able to integrate the various components under a single software platform. LabVIEW programs have been written to control and automate all these experiments. One program generates pulsing signals via an analog output board to move the tip approach and objective motor. The same hardware and software also controls the stick-slip signals to move a sample on the stage. A touchdown program is written to move the tip and stage in turns continuously and read and analyze signals of feedback loop in order to stop them when the tip is within range of the sample.

The AFM controller mentioned above is connected via Ethernet to a host computer and controlled by a custom defined protocol. A suite of LabVIEW routines have been developed to run the AFM controller. Figure 41 shows the control panel of this program. Similar programs are also written to read data from the controller and plot it into images. Automation is achieved by sequencing or synchronizing all of the functions.

3.3 Conclusions

We have developed instruments to investigate structural and optical properties of the quantum dot materials. AFM and ANSOM experiments can now be carried out at room and cryogenic temperature to study the physical appearance, spectral properties and the relation between the two. Knowledge obtained from these experiments will play a significant role in the future applications of the directed self-assembly of Ge/Si quantum dots, including quantum computation.

4.0 A Molecular Scale Shift Register Memory.

4.1 Synthesis and Fabrication of Shift Register Memories

We have developed a general synthetic procedure for the assembly of supramolecular shift-register memories of the type shown below:
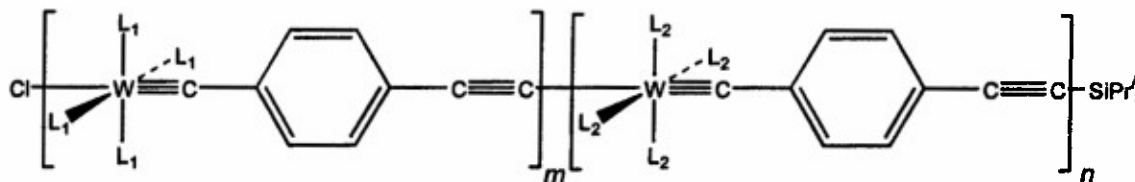
In these complexes L_1 and L_2 are ligands that control the local redox properties of the component electron-transfer cells and, thus, the mechanism by which the register operates. The step-growth procedure involves salt metathesis between one cell terminated with the triflate ($CF_3SO_3^-$) leaving group and a second cell terminated with an alkynyl-lithium moiety, which results in condensation of the cells.

This method was successfully applied to the synthesis of the two-cell (A–B) registers $Cl(dppe)_2W(\mu\text{-}\equiv CC_6H_4C\equiv C)W(\equiv CBu^t)(dmpe)_2$, **1**, and $Cl(dppe)_2W(\mu\text{-}\equiv CC_6H_4C\equiv C)W(\equiv CPh)(dmpe)_2$, **2**, which in their neutral form represent the bits "1,1". These registers are terminated by the electronically distinct alkylidyne R groups CMe_3 (**1**) and Ph (**2**), so that the n$\rightarrow\pi^*$ electronic transition energies of cell B are designed to be higher and lower respectively, than that of cell A, which is common to both registers. The equatorial ligands of cell A ($Ph_2PCH_2CH_2PPh_2$, dppe) and cell B ($Me_2PCH_2CH_2PMe_2$, dmpe; $Ph_2PCH_2CH_2PPh_2$, dppe) differ so that the redox states (1, neutral; 0, oxidized) of the A and B cells could be independently addressed. In both shift registers the cells are connected by a phenylene-ethynylene spacer; the theoretical analysis of the electron-transport properties of this spacer and its derivatives is described below.

We completed the characterization of these materials by conventional analytical methods, which provided key fingerprint NMR and mass spectrometric (MALDI, LC-MS) data for identifying the local chemical environments of cells in supramolecular assemblies. Shift register **1** was also characterized by a single-crystal X-ray diffraction study, which provided quantitative information about its molecular structure (shown below). The core bond distances and angles of
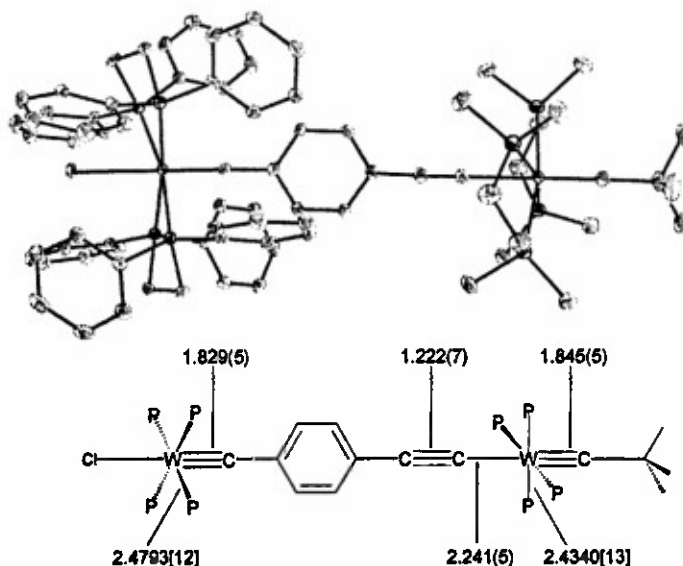
1 were determined to lie within the expectation ranges for its constituent cells. The important conclusion that can be drawn from these data is that the shift registers maintain the alternating bond order canonical structure expected for a conventional organic molecular wire; thus, substituting triply bonded metal atoms for triply bonded carbon atoms maintains the π-conjugated pathway necessary for efficient intra-cell and inter-cell electron transfer.

We completed a survey of alternative synthetic methodologies for the assembly of shift-register complexes. These methods included: (1) palladium-catalyzed cross coupling of condensable monomers of the type $W(\equiv CC_6H_4I)(dmpe)_2(C\equiv CH)$; (2) alkyne metathesis metal incorporation into alkyne-terminated monomers such as $W(\equiv CR)(dmpe)_2(C\equiv CC_6H_4C\equiv CBu^n)$ (R = H, Ph); and (3) dative self assembly of self-complementary ionic cells with labile axial ligands, typified by $[W(\equiv CC_6H_4C\equiv CC_5H_4N)(dppe)_2(NCMe)]^+$. These methods were not developed beyond the proof-of-principle stage because they either gave lower yields of register complexes or poorer control over monodispersity than the step-growth method described above.

In addition to assembling the shift registers 1 and 2, we completed the synthesis and characterization of test complexes for the study of inter-cell electronic communication. The complexes of formulae $W(\equiv CBu^t)(dmpe)_2(C\equiv CC_6H_4C\equiv CBu^n)$ (3) and $W(\equiv CPh)(dmpe)_2(C\equiv CC_6H_4C\equiv CBu^n)$ (4) contain the π-conjugated framework of 1 and 2, respectively, with the metal center of cell B present but the metal center of cell A absent. The complex $W(\equiv CC_6H_4C\equiv CH)(dppe)_2Cl$ (5) represents the registers 1 and 2 without the metal centers of the B cells. These were extensively characterized by standard analytical methods.

4.2 Optical, redox, and photophysical properties of shift registers.

We completed the electrochemical, photophysical, and electronic-spectroscopic characterization of registers 1 and 2 and the related test complexes 3–5. The properties are summarized in the table below. The data validate and extend several design principles

39

regarding the shift registers: (1) the electronic transition energies of electron transfer cells can be controlled by modification of the alkylidyne R group, and these properties carry over into the shift registers; (2) the oxidation potentials of electron-transfer cells in shift registers can be tuned, to within 100 mV, via the equatorial ligand, regardless of the nature of the shift register; and (3) the luminescence properties of these cells "turn on" when assembled into shift registers. The main conclusions that can be drawn from points 1 and 2 as regards the objectives of this project are that, indeed, cells within registers can be individually addressed, and the addressability can be controlled through chemical design. Point 3 illustrates that complicated chemical structures do not necessarily facilitate nonradiative decay pathways, which would lower the efficiency of electron transfer processes; in fact, in the present case, the photophysical properties of the registers are much improved over those of the cells.

Table 1.

Spectroscopic, photophysical, and electrochemical data (THF or 2-MeTHF solution).

Compound	$n \rightarrow \pi^*$ (nm)	Emission (nm)	τ_{em} (ns)	$E_{1/2}$ (V, $FeCp_2^{0/+}$)
1	510, 580	640, 680	740	–0.98, –0.58
2	560	700	—	–1.07, –0.57
3	490	not observed	not observed	–1.04
4	570	not observed	not observed	–0.89
5	580	735	200	–0.54

4.3 Theoretical Analysis of tunneling pathways

We have completed theoretical investigations of electronic coupling interactions through derivatized phenylene(Ar)-ethynylene spacers below. The
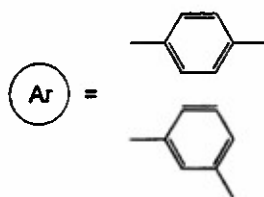
studies that were carried out probed the decay of the donor-acceptor interactions, and electron transfer rates, as a function of (1) the number of repeating units in the phenylene-ethynylene chain and (2) the substitution pattern of the phenyl substituent (meta *vs* para). We find the coupling interactions are substantially stronger in these unsaturated bridges than in previously examined saturated alkanes and that the interactions are dominated by the Π-electron orbitals. Electron transfer couplings are expected to decay by about a factor of six per phenyl-ethyne unit (in the planar geometry), based on our quantum mechanical calculations. In the case of meta-substitution, an orbital symmetry effect leads to an additional predicted ten-fold drop in the rates. The meta-effect on sigma electron communication is modest, but sigma-mediated communication is many orders of magnitude weaker than the pi-mediated communication in these structures.

We have also examined the changes in bridge-mediated coupling as a function of ring twist. The coupling decay changes by about a factor of ten as the central ring in a three-ring bridge is made orthogonal to its neighbors. The pure distance decay for a coplanar chain would result in rate change by about a factor of 36 per phenylene ethynylene unit. The strength of the down-chain coupling is sensitive to ring substitution pattern. The coupling pathways in the para- derivative interfere constructively, while the meta-derivative pathways interfere destructively. Electronic coupling varies by a factor of 10-100 as the donor and acceptor energies are swept through the range accessible to the experimental systems, from near resonant to far off resonant.

4.3.1 Electron transfer reorganization energy

We have used finite-difference solutions of the Poisson equation to estimate reorganization energies of model phenylene ethynylene compounds in polar solvents. Estimates of the reorganization energies fall in the 1-2 eV range, and increase by about 10% per phenylene ethynylene ring added in the range from one to three rings.

4.3.2 Pathway Dephasing

The calculations described above assume that the electronic coupling pathways in the bridges interfere with each other "coherently". The parallel paths are analogous to slits in a screen of a multi-slit electron transmission experiment. When electron transmission through a *specific* slit is detected by an observer, the diffraction (interference) pattern is destroyed. In our electron transfer case, "observation" of the propagation pathways can be established if one arm of the system has an inelastic channel for electron energy loss. We have constructed a model Hamiltonian to examine these pathways dephasing effects in bridge mediated electron transfer processes, and have performed preliminary examination of how dephasing effects might influence electron transfer rates in shift register elements. In mesoscale structures, pathway coherence among two arms of an electron interferometer has been controlled by secondary lithographic structures that are perturbed by the presence of an electron in one arm of the interferometer. The goal of our study is to understand the nature of tunneling pathway decoherence in *molecules*. Using this model Hamiltonian, we have demonstrated that inelastic tunneling indeed destroys pathway coherence and that this can lead to dramatic changes in electron transfer rates in chemical systems, especially those with destructively interfering pathways.

41

5.0 Nanoworkbench for Analysis, Manipulation, and Excitation of Individual Nanostructures.

5.1 Introduction.

We constructed a novel instrument that combined a multiple tip STM device, with an SEM and with an Auger analyzer for the study of single nanostructures. This system was coupled to a multiple UHV chamber system which allowed molecular beam epitaxy (MBE) and was equipped with multiple surface analysis capabilities. The activities of the last two years have been mainly focused on the construction and the testing of the novel device. The construction is now mainly completed and first results have emerged.

5.2 Technological Progress

5.2.1 UHV Chamber System

The design of the three UHV chamber system as shown Fig. 42 is completed and most of the vacuum parts have been constructed by the local machine shop and Kurt Lesker Company. All chambers are connected with each other through a special sample transfer system. This chamber system allows ultra clean sample preparation and characterization. The multiple source MBE (molecular beam epitaxy) chamber has been designed to be equipped with several electron beam evaporators for precise deposition and doping of metals and semiconductors.
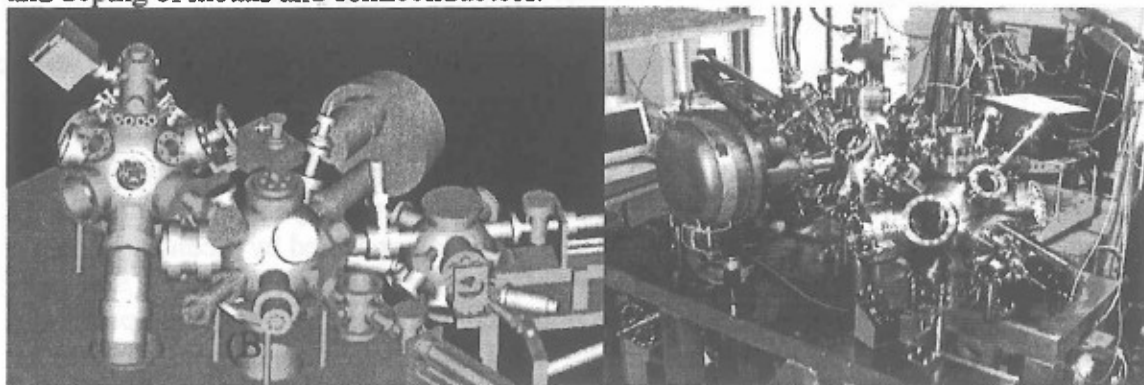
Figure 42. Three UHV chamber system.

5.2.2 Sample Heating and Cooling Device

For the controlled growth of atomically flat and pure silicon surfaces, as well as for Ge and carbon directed self-assembled quantum dot structures it is important to have precise control of the sample temperature in each UHV chamber. For this purpose a special transferable sample box with integrated heating device has been build and tested (Fig. 43). The temperature distribution was measured by an infra-red pyrometer and shows substantial derivations from the normally used thermocouple measurements.
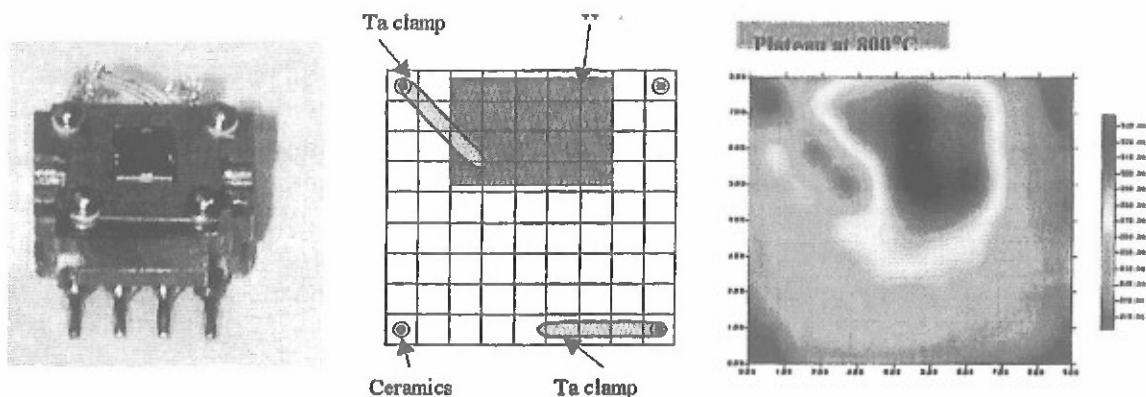
Figure 43. Left: transferable sample box with integrated heater and mounted Si (100) sample. Middle: Principle of pyrometer measurements matrix. Right: Temperature profile of the molybdenum plate, as measured with the pyrometer, for the home-made heater. The plateau value of 900°C is controlled via the TC connections and LabVIEW.

5.2.3   Multiple Tip STM

5.2.3.1 Novel Nanomanipulator MM3

In collaboration with Kleindiek Nanotechnik, we developed the novel STM-nanomanipulator MM3, which has a large operation range and allows easy STM tip exchange in UHV. The MM3, as shown in Figure 44, combines one linear motion with two rotational motions of more than 180^0 of freedom.

State of the art electronics and appropriate software have been developed to allow precise macroscopic movement of the tip as well as STM imaging with atomic resolution. We consider this achievement as a milestone in the development of a nanoMBE system for Ge quantum dots growth, as described below.
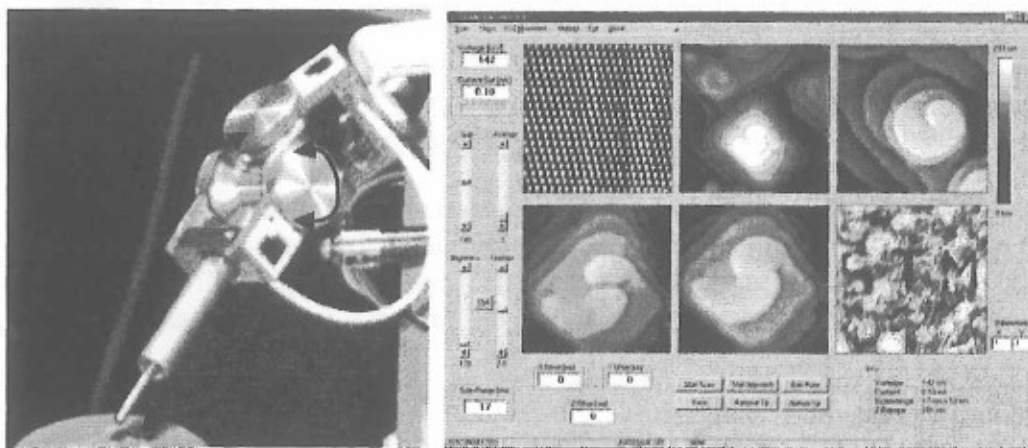
Figure 44. MM3 nanomanipulator. A specially developed computer program can rotate the STM tip in any direction and atomic resolution can be achieved by imaging a plane tilted in any direction.

5.2.3.2 Four Tip STM Assembly

Figure 45 shows the homebuilt STM mounting assembly with 4 STM probes in place. The STM tips are mounted at 45 degrees to the axis, and at 90 degrees to each other. The actual photograph of the devise (figure 45 center) shows additionally the recently developed high precision x,y,z-table with +/-10 mm range and sub-atomic resolution in all three directions. The table is equipped with novel position encoders (resolution better than 100 nm). It is fully programmable by an electronic pattern generator and can by used itself as a scanner for four point STM measurement.
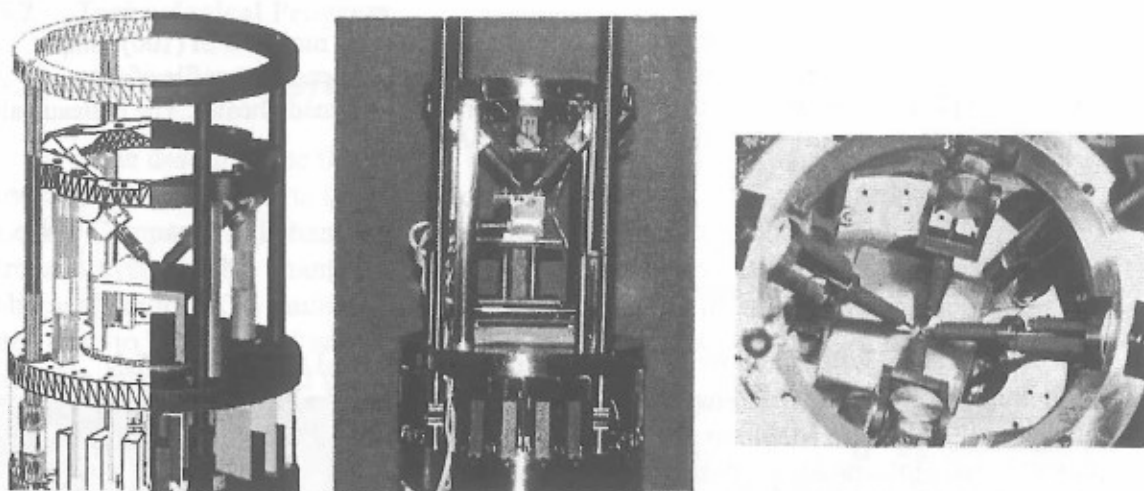
Figure 45. UHV multiple tip STM with eddy current damping system. Left: Design drawing. Middle and right hand side: Actual device side and top view.

In order to isolate the STM system from external vibrations, specific springs have been fabricated by using Inconel 700 wire. All four springs have exactly adjusted force constants and together with an Eddy current damping system, coupling of the resonant frequencies of the apparatus is avoided.

5.2.3.3 Vibration Analysis of Eddy Current Damping System of Multiple Tip STM

For high resolution multiple tip STM measurements an effective vibration isolation system is crucial. Fig. 46 describes a vibration analysis experiment recently performed on the Eddy current damping system of the multiple tip STM. The results are shown in Figure 47. This analysis enabled us to optimize the force constant of the spring system as well as the damping constant.

The transmission function of the optimized system was measured (Fig. 48) and the resonance frequencies of the vibration isolation system (~1.5 Hz) could be kept far from the lowest natural frequency of the nanomanipulators (~200 Hz), leading to a very effective vibration isolation.

Hanging Stage   CCD Camera   Pentium III
                                                   Computer
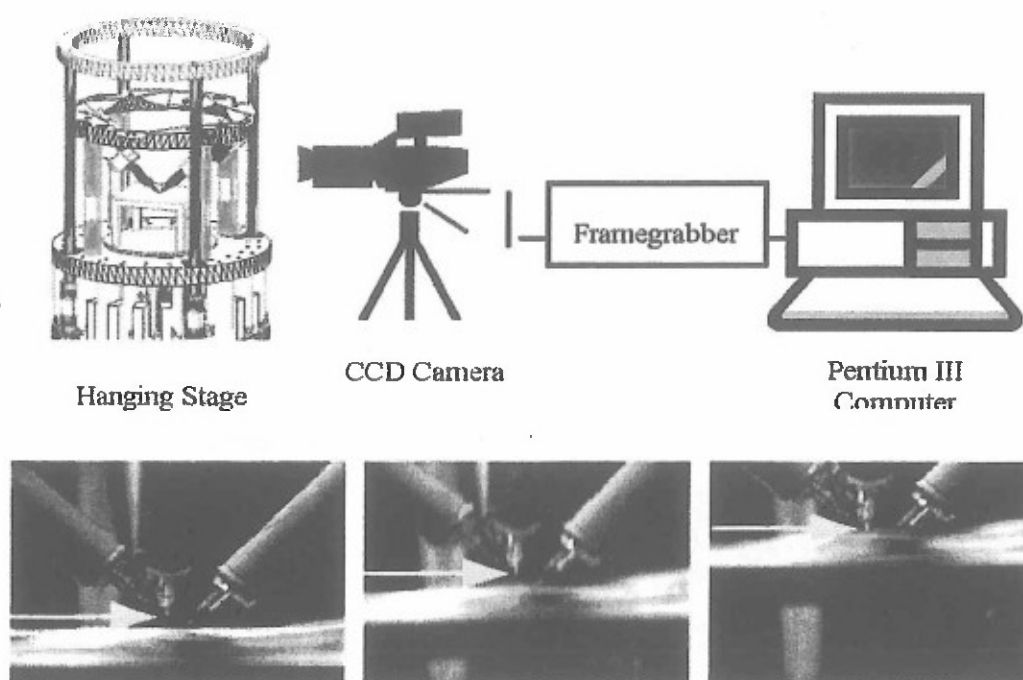
Figure 46. Setup for the vibration analysis experiment.

Figure 48. Transfer function of the suspended multiple tip STM device. Inadvertent vibration amplification of a factor of 2.68 is expected at the natural frequency.
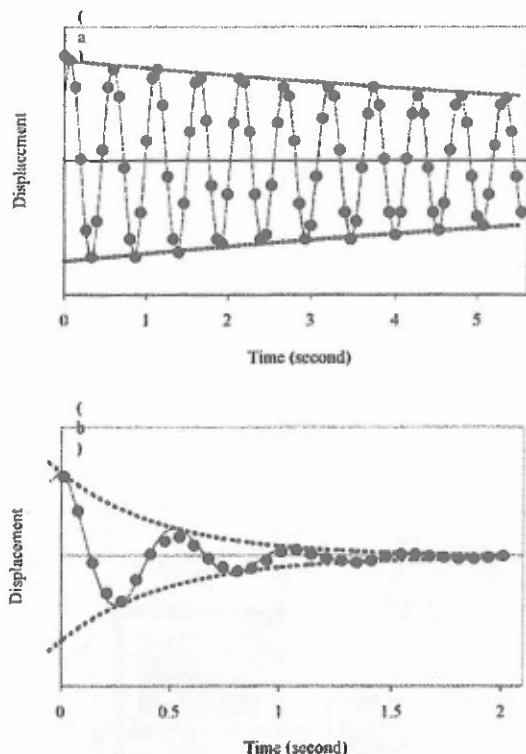
Figure 47. Relaxation of the STM unit, (a) without the Eddy-current damper and (b) with the Eddy-current damper.

5.2.3.4 Active Vibration Damping System

While the vibration problems effecting the multiple tip STM measurements have been solved by the internal Eddy current damping system, a separate solution had to be found to isolate the combined system (SEM/STM) from external vibrations. This has been achieved with a six point active vibration damping system for the whole UHV system. A special aluminum frame exhibiting a resonance frequency higher than 200 Hz has been designed and constructed in the local machine shop (Fig. 48).

Figure 49. Special frame exhibiting high resonance frequency. Together with a six point active vibration damping element it allows effective vibration isolation of the whole UHV system.

5.3 First Results

5.3.1 UHV- SEM. Manipulation of Nanometer Scaled Material Under SEM Control

The operation of the FEI column was tested in UHV by using a home-build channeltron detector which was operated in pulse-counting mode. Recently, an ultra thin microchannel plate (Hamamatsu F6589) with a hole in the center was mounted closely underneath the electron column and a dramatically increased SNR (factor 5) was observed. Fig. 49 shows the electron column mounted in the UHV chamber together with two STM tips.

Figure 50 shows two SEM images from a video documenting two STM tips approaching an isolated gold coated polystyrene (PST) particle of 500nm diameter. We succeeded for the first time to precisely position two tips under SEM control on selected PST particles in order to measure their electronic properties.
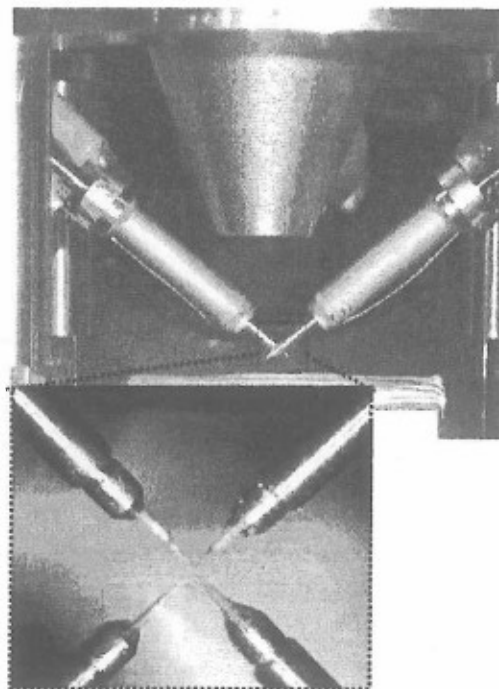
Figure 50. The electron column mounted in the UHV chamber (only the end tip is seen) together with the two STM tips, approaching each other.
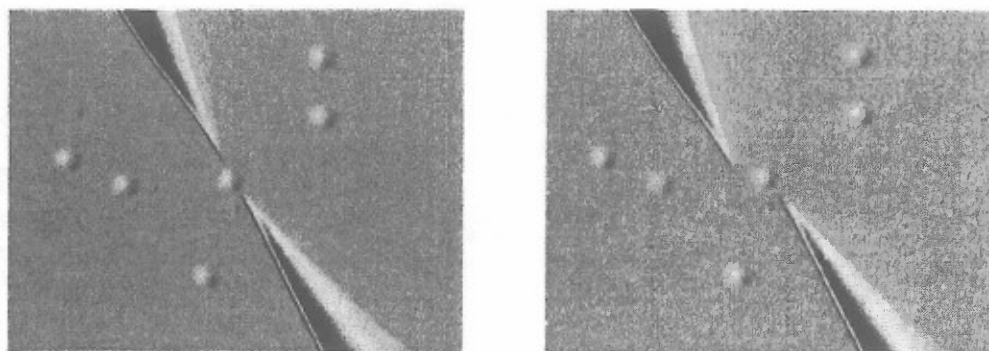
Figure 51. In-situ SEM imaging of two STM tips approaching an isolated PST particle. This images demonstrate for the first time the operation of a multiple tip STM.

5.3.2 Development of Nano-MBE System for Ge Quantum Dot Growth

Recently published results[29,30] indicate that Ge quantum dots grow on Si with a much smaller size after pre-deposition of carbon or Sb atoms. This ultra-small Ge dots show much enhanced photo luminescence than those grown without pre-deposition. Fig. 51 shows on the right hand side carbon induced ultra-small Ge quantum dots. Ge dots grown without carbon form pyramids about ten times larger in size than required (left).
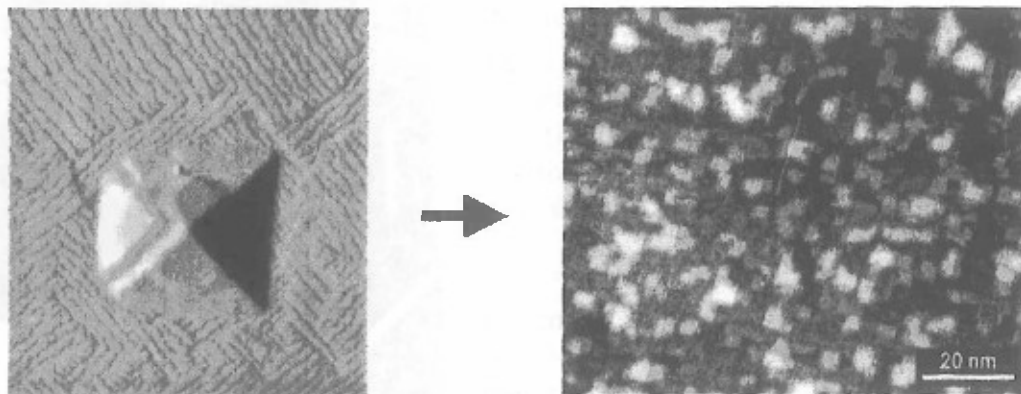
Figure 52: Left: Typical Ge-dot grown on Si substrate with a diameter of 80 nm (too large for quantum electronic devices. Right: Precise control over carbon deposition results in the growth of ultra-small Ge quantum dots.

Based on this information we are currently developing a NanoMBE system which uses the multiple tip STM (figure 52) to deposit various atoms at controlled surface sites This atoms subsequently act as nucleation centers for the Ge quantum dots. We are working on a method to equip the tips with reservoirs of the specified atoms. From these reservoirs the atoms supposed to diffuse to the tip end. For the deposition in UHV we will use field evaporation of atoms from the tip by applying relatively large voltage pulses or by a controlled tip approach as demonstrated in Figure 53.
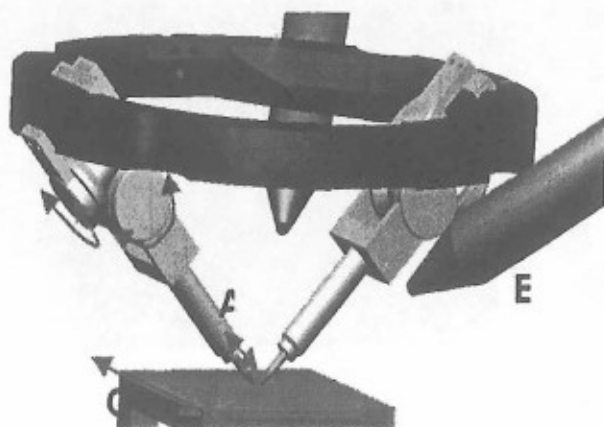
Figure 53. Up to four independently working STMs (A) are combined in the nanoworkbench. They are used to create patterns of carbon or Sb atoms on the Si substrate Evaporators(B) allow parallel deposition of Germanium and Si material. A high precision sample allows large scale positioning in x/y directions of the silicon substrate (C).

5.3.3 STM Tip Assisted Growth of Ge Dot Using a Precursor Molecule.

We succeeded in growing small Ge dots by using a precurser molecule and the STM tip. In Figure 54 the controlled growth of a Ge quantum dot in field-induced mode from Ge_2H_6 precursor molecules on the Si(111)-(7x7) surface is demonstrated. In this work the sample is biased negatively, and the emitted electrons can not gain sufficient energy to induce electron attachment effects in the region occupied by the adsorbed Ge_2H_6 molecules[32].
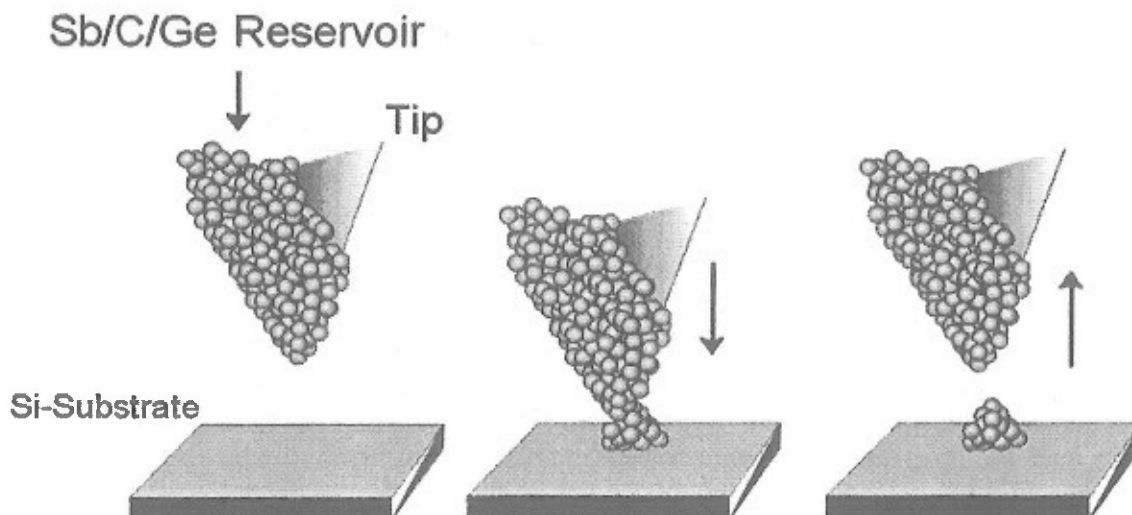
Figure 54. Schematic diagram of the suggested mechanism of material transfer from the STM to the Si substrate, caused by an appropriate tip approach.
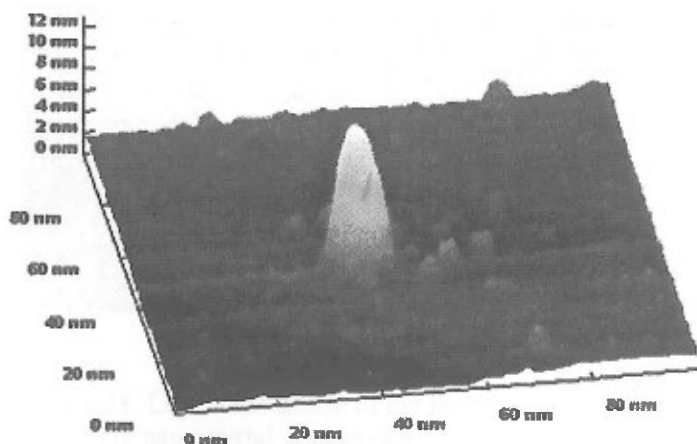
Figure 55. 3D constant current STM image (V = -2.5V, 1 = 0.01 nA) of a typical GeH_X nanostructure grown at negative sample bias voltage. Growth parameters were: V = -7 V, 1 = 0.01 nA, F = 4.1×10^{12} molecules/cm^2s, t = 3 min.

The experiments were conducted in a UHV chamber (base pressure $\sim 6 \times 10^{-11}$ Torr) equipped with a STM (Omicron) using electrochemically etched tungsten tips ($R_{Tip} \sim 5$ nm). The nanostructure was grown at room temperature by dosing Ge_2H_6 gas through a conductance-calibrated stainless steel doser located 4 cm away from the

49

tunneling junction, as schematically shown in figure 55. The flux of Ge_2H_6 is 4.1×10^{12} molecules/cm^{2}s.
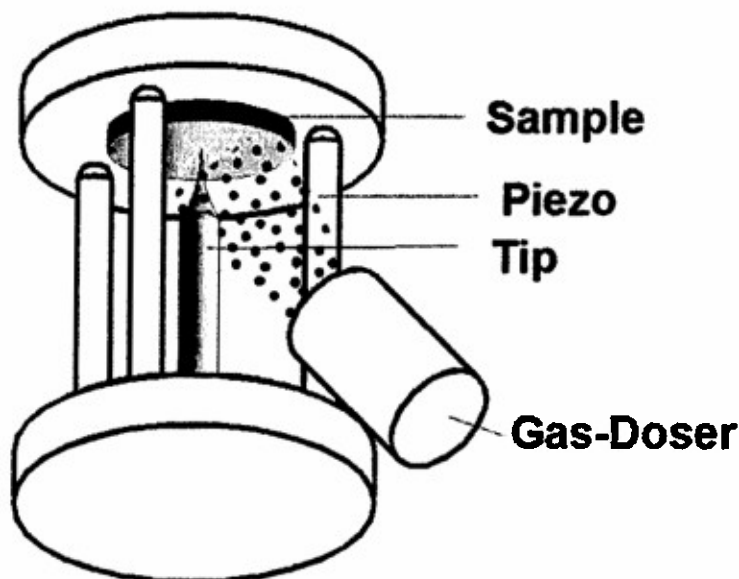
Figure 56. Schematic of experimental set-up for STM assisted growth of Ge dot.

The STM was operating in a tunneling or a field emission regime (negative sample bias) in the constant current mode. Before the growth, the Si(111)-(7×7) surface has been saturated with Ge_2H_6.

The grown nanostructure of this preliminary experiment is likely to be of composition GeH_X rather than pure Ge based on studies of CH_3SiH_3 decomposition on Si(100) induced by electrons[33]. For useful Ge quantum dots, it is likely that subsequent annealing of these structures will be necessary.

5.3.4. Progress in Growing Isolated Single Wall Carbon Nanotubes for Electronic Devices.

In order to measure accurately the electronic transport properties of carbon nanotubes (CNT) of various diameters by using the multiple tip STM it is necessary to control the growth CNTs and suspend them on insulating pillars. One successful method is to use CVD on Ni or FeO_2 nanoparticles as catalysts [1-4] for the growth of aligned carbon nanotubes. For this purpose a CVD set-up according to the literature [2] has been built in our laboratory. We succeeded to grow free standing Carbon nanotubes on various substrates as shown in figure 56a for a Ni-covered copper substrate. We also succeeded to grow mono-sized Ni clusters with an diameter of approximately 10 nm on a Si (100) surface which subsequently act as catalysts for the carbon nanotube growth as show in figure 56b.
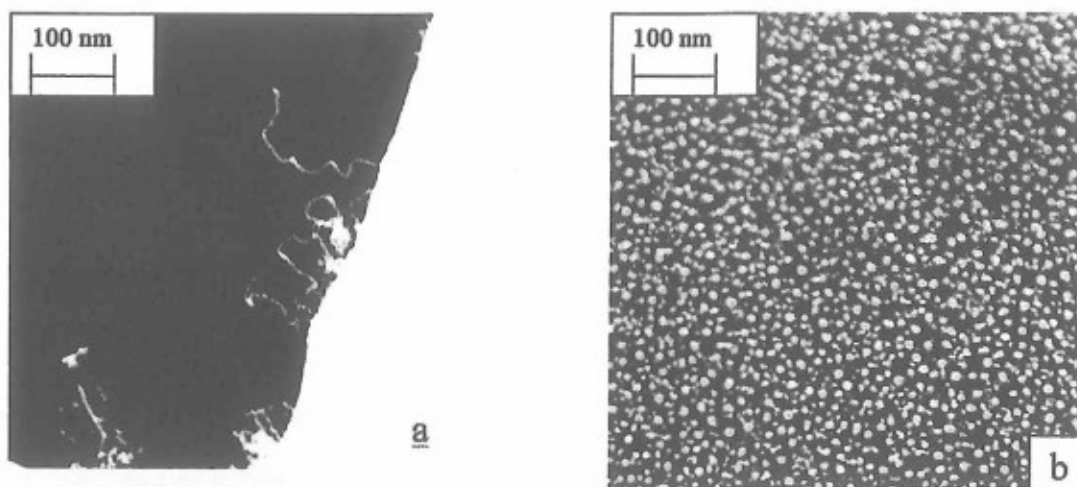
Figure 57. (a) Free-standing single carbon nanotubes grown on Ni catalysts deposited on a Cu substrate. (b) Mono-sized Ni particles grown on a Si(110) substrate.

5.3.5 Demonstration of Nanoworkbench Measurements

A method for etching the very fine STM tips has been developed in our laboratories which is capable of making slender tungsten tips with hemispherical ends of 3 – 5 nm radius[34]. These tips have been employed to probe the behavior of Ge nanocrystals deposited on Si(100). Figure 57 shows 4 tips in contact with a Ge nanocrystal at four separate exposed facet faces.
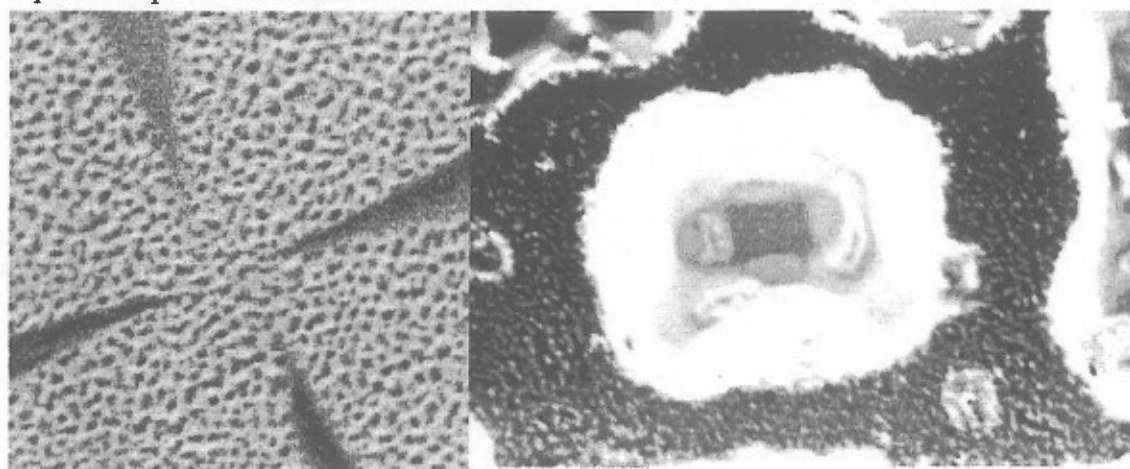
Figure 58. Left. SEM image of the four STM tips approaching an array of Ge- nanocrystals. Right: Ge nanocrystal contacted by 4 STM tips.

The results shown in Figure 57 demonstrate the first application of the nanoworkbench to the electrical characterization of a nanoobject, and demonstrate that the nanoworkbench is now working. The image in Figure 57 employs the SEM at a resolution of the order of 5 nm.

We have also demonstrated that in the STM mode, the nanoworkbench is capable of atomic level imaging. Figure 58 shows STM images made with a single tip in the STM mode. Atomic resolution could be demonstrated by imaging a Highly Oriented Pyrolytic Graphite, (HOPG) surface (Figure 58 a). Figures 58 b)…e) show STM images of a sputtered YBCO thin film at different scan ranges between 500 nm x 500 nm to 50 nm x 50 nm. The STM image f) demonstrates the writing capabilities of the special developed scan control electronic and software program. The STM tip has been moved 130 times along the scripture over a YBCO film with a tunnel current of 1 nm and a bias voltage of 0.5 V. The scan range here is 1.2 μm x 1.2 μm.
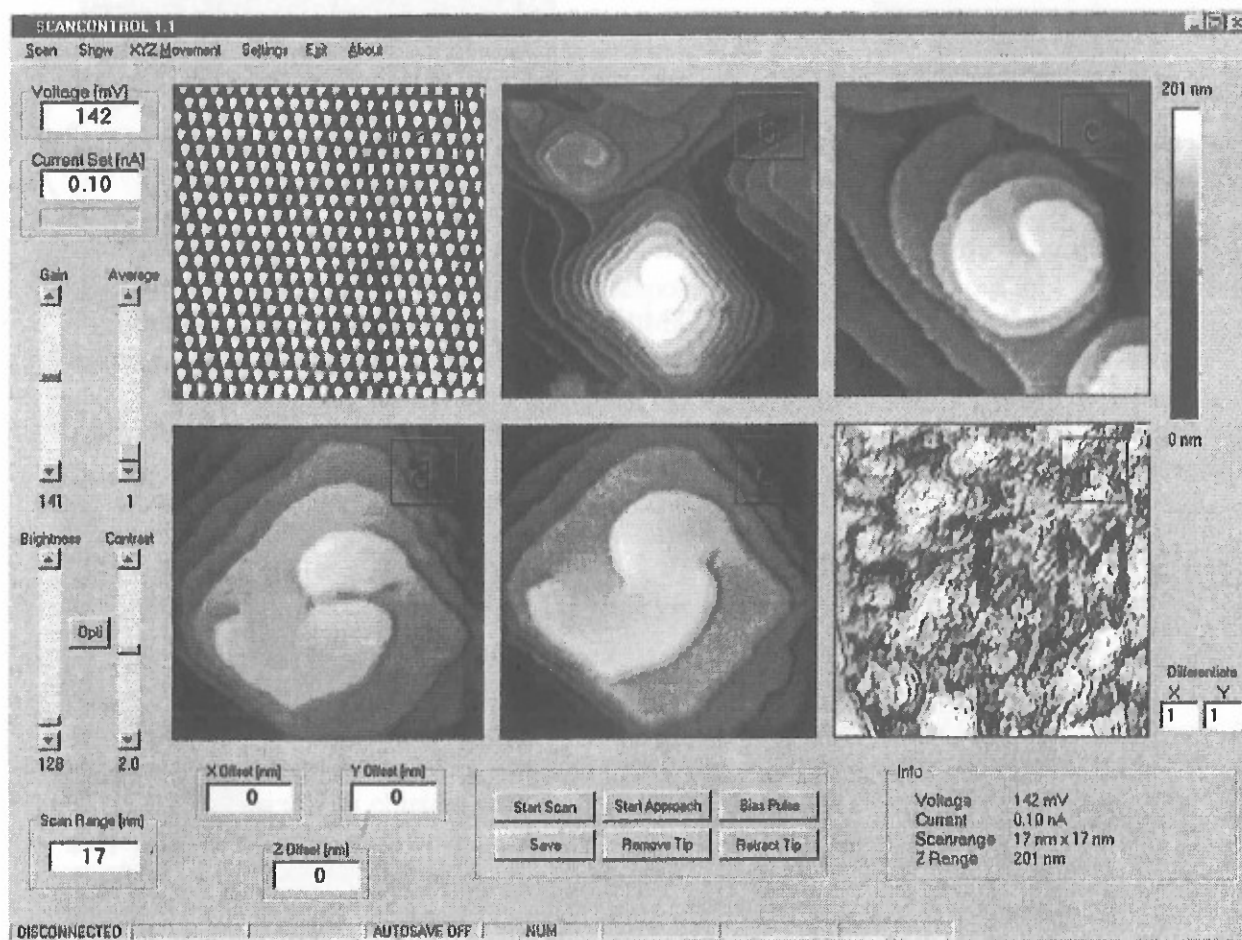
Figure 59. STM level imaging with the Nanoworkbench using a single tip. a) shows atomic resolution of HOPG surface. Images b)…e) show STM images of sputtered YBCO thin films at different scan ranges between 500 nm x500 nm to 50 nm x50 nm. f) demonstrates the writing capabilities of the four tip STM.

The results shown in Figures 57 and 58 are our first demonstrations of the operation of the Nanoworkbench.

6.0 Nano-optics and Chemical Imaging

The Walker group has built an aperture less near-field scanning infrared microscope which has a spatial resolution of <100 nm[35]. The microscope tip moves across a surface much like a tapping mode AFM tip. However, a laser field is also incident which can interact with the functional groups on the sample surface. In this microscope (Fig. 60), incident infrared radiation simultaneously interacts with the local optical properties of the sample (absorption and dispersion) and with the geometry of the probe assembly. The magnitude, polarization and phase of the IR radiation at an inhomogeneous sample surface varies according to the sample's properties. Changes in the detected intensities as a function of the probe position along the surface chemically maps the surface absorption spectrum.
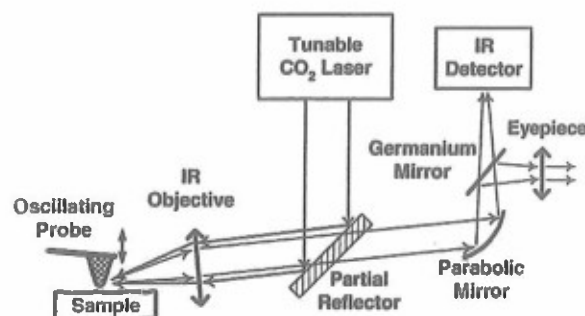
Figure 60. ANSIM: Apertureless Near Field Scanning Infrared Microscope.

We have applied the microscope to examine polymeric nanostructures (Fig. 61). In the figure green indicates strong scattering of light back to the detector, while purple indicates less scattering of light back to the detector. We discovered that it is important to move the tip at a constant height above the surface when imaging. The top panel of Figure 61 does not follow this mode of imaging, and topography related artifacts (the purple rings) dominate the signal. When we preread the topography and move at a constant height above the substrate onto which the film was cast, the chemical sensitivity of the instrument emerges. In this case the signal, which represents light scattered by the sample immediately beneath the tip, is properly attenuated while the chemical functional groups of the sample absorb the light. Therefore, the purple regions in the lower panel of figure indicate the presence of O-Si-O stretch vibrations of PDMS that absorb the incident light[35,36].
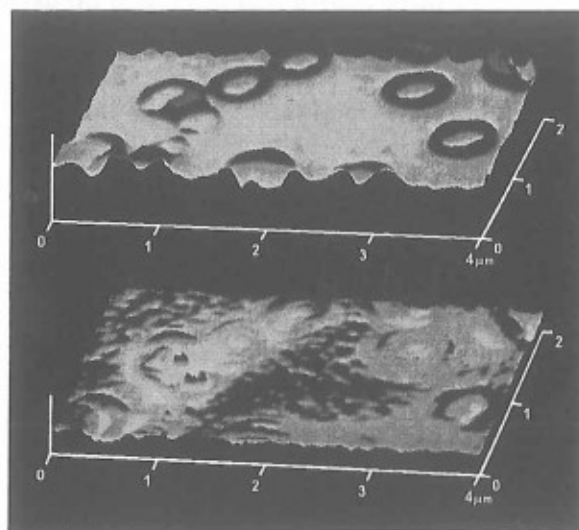
Figure 61. ANSIM image of cast polydimethylsiloxane-polystyrene (PDMS-PS) block copolymer surface. Laser wavelength in resonance with PDMS block. Top panel (constant gap scanning) shows consequence of topographic coupling. Bottom panel (constant height scanning) shows that PDMS domains are in fact the small bump features between the rings.

This microscope is extremely sensitive, and can detect even sub-monolayer coverages of DNA[37] on surfaces (Fig. 62). In this figure the spectrum of the sample collected by a normal far-field spectrometer is shown by small dots. The near field spectrum of the phosphate groups of DNA is shown by the triangles, and is seen to follow the far field spectrum, indicating the near field microscope is detecting the phosphate groups. We also developed other scanning probe analysis methods to examine polymer and colloidal particle assembly.[38-40]

In conjunction with the microscope development, we have also accomplished state-of-the art calculations of the predicted signals. In order to calculate the imaging properties of our microscope, we applied both an analytical model and a three-dimensional finite difference time domain (FDTD) method to solve Maxwell equations in order to calculate the scattering for an arbitrary probe-sample geometry.

We have shown that the metal tip used in the near field imaging acts as an antenna to enhance the laser light, and this understanding is inspiring us to develop new special tips with shapes that will be useful for developing better microscopes and other nano-optical devices.

Spectrum of DNA grafted on gold
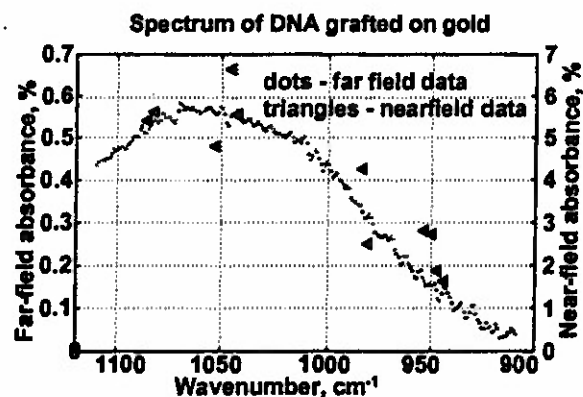
Figure 62. Comparison of frequency dependence of far field and near field absorption for sample 24 base pair single stranded DNA grafted onto a gold surface. The surface coverage is about 20% of a monolayer.

7.0 REFERENCES

1. Holtz, J.; Weissman, J.; Pan, G. and Asher, S. A., Material Research Soc., 1998, 23, (44).
2. Asher, S. A.; Holtz, J.; Liu, L. and Wu, Z., J. Am. Chem. Soc. 1994, 116, 4997-4998.
3. Holtz, J.H.; Holtz, J.S.W.; Munro, C.H., and Asher, S.A., Anal. Chem. 1998, 70, 780-791.
4. Holtz, J. H. and Asher, S. A., 1997, Nature, 1997, 389, 829-832.
5. Weissman, J.; Sunkara, H.; Tse, A. and Asher, S. A., 1996, Science, 274, 959-960.
6. Pan, G.; Kesavamoorthy, R. and Asher, S. A. 1997, Phys. Rev. Lett. 78, 3860-3863 .
7. Pan, G.; Kesavamoorthy, R. and Asher, S. A., 1998, J. Am. Chem. Soc. 120, 6525-6530.
8. Tanaka, T. and Fillmore, D.J., 1979, J. Chem. Phys. 70, 1214.
9. Kesavamoorthy, R.; Super, M. and Asher, S. A., 1992, J. Appl. Phys. 71, 1116.
10. Rundquist, P.A.; Photinos, P.; Jagannathan, S. and Asher, S. A., J. Chem. Phys., 1989, 91, 492.
11. Xu, X.; Friedman, G.; Humfeld, K.D.; Majetich, S.A. and S. A. Asher, 2002, Chem. Mat. 14, 1249-1256.
12. Xu, X.; Friedman, G.; Humfeld, K.D.; Majetich, S.A.and Asher, S.A., 2001, Adv. Mat. 13, 1681-1684.
13. Xu, X.; Majetich, S.A. and Asher, S. A., 2002, J. Am. Chem. Soc. in press.
14. Yanase, N.; Noguchi, H.; Asakura, H. and Suzuta, T., 1993, J. Appl. Polym. Sci. 50, 765-776.
15. Sauzedde, F.; Elaissari, A.; Pichot, C., Colloid Polym. Sci., 1999, 277, 846-855.
16. Kang, Y.S.; Risbud, S.; Rabolt, J.F. and Stroeve, P., 1996, Chem. Mater. 8, 2209-2211.
21. Parik, S.H. and Xia, Y., 1999, Langmuir, 15, 266-273.
18. Cullity, B.D., Introduction to Magnetic Materials (Addison-Wesley, Reading, 1972).
19. Tissot, I.; Novat, C.; Lefebvre, F.; Bourgeat-Lami, E., 2001, Macromolecules, *34*, 5737-5739.
20. Takei, H.; Shimizu, N., 1997, Langmuir, 13, 1865-1868.
21. Reese, C.E.; Baltusavich, M.E.; Keim, J.P.; Asher, S.A., 2001, Anal. Chem, 73, 5038-5042.
22. Still, W.C.; Kahn, M.; Mitra, A., J. Org. Chem. 1978, 43, 2923.
23. Juaristi, E.; Martinez-Richa, A.; Garcia-Rivera, A.; Cruz-Sanchez, J.S., J. Org. Chem., 1983, 48, 2603.
24. Joannopoulos, J.D.; Meade, R.D. and Winn, J.N., Photonic Crystals: Molding the Flow of Light", (Princeton Univ. Press, Princeton, NJ, 1995).
25. Yeh, P.; Yariv, A., and Hong, C.-S., 1997, J. Opt. Soc. Am. 67, 423.
26. Mittleman, D.M.; Bertone, J.F.; Jiang, P.; Hwang, K.S. and Colvin, V.L., 1999, J. Chem. Phys. 111, 345.
27. Taflove, A., Computational Electrodynamics. The Finite-Difference Time Domain Method (Artech House, MA, 1995).

28. Bohren, C.F.; Absorption and scattering of light by small particles, (John Wiley & Sons, Inc., 1983).
29. Leifeld, O.; Hartmann, R.; Müller, E.; Müller, B.; Kern, K., and Grützmacher, D., Self organized growth of Ge quantum dots on Si [100] substrates induced by sub monolayer C coverages, 1999, Nanotechnology, 10, 122.
30. Peng, C.S.; Huang, Q.; Cheng, W.Q., and Zhou, J.M., Optical properties of Ge self organized quantum dots in Si, 1998, Phys. Rev. B **15** 8805.
31. Mezhenny, S.; Lyubinetsky, I.; Levy, J., and Yates, J.T., Jr., STM tip assisted growth of Ge dot using a precursor molecule, submitted to *J. Appl. Phys. Lett., June (2000)*
32. Lyubinetsky, I.; Mezhenny, S.; Choyke, W.J., and Yates, J.T., Jr. Two mechanisms of STM assisted nanostructure formation using precursor molecules, 1999, J. Vac. Sci. Technol. A 17, 1445; Scanning tunneling microscope assisted nanostructure formation: Two excitation mechanisms for precursor molecules, 1999, J. Appl. Phys. 86, 4949.
33. Xu, J.; Choyke, W.J., and Yates, J.T., Jr., Amorphous SiC Film formation on Si(100) using electron beam excitation, Appl. Surf. Sci., 1997, 120, 279.
34. Guise, O.L.; Ahner, J.W.; Jung, M.-C.; Goughnour, P.C., and Yates, J.T., Jr., Reproducible electrochemical etching of tungsten probe tips., 2002, Nano Letters 2(3) 191.
35. Akhremitchev, B. B; Walker G. C. "Apertureless Scanning Near-Field Infrared Microscopy of Rough Polymeric Surface", *Langmuir*, 2001, 17, 2774-2781.
36. Akhremitchev, B. B. and Walker, G. C. "Developing Vibrational Infrared Near Field Spectroscopy to Characterize Polymer Structures on Surfaces", *Bull. Chem. Soc. Japan.*, 2002, *75*, 1011-1018.
37. Akhremitchev, B. B.; Sun, Y.; Stebounova, L.; Walker, G. C. "Monolayer-Sensitive Infrared Imaging of DNA Stripes Using Apertureless Near-Field Microscopy", *Langmuir*, 2002, 18, 5325-5328.
38. Sun, Y.; Walker, G. C. "Two-Dimensional-Self-Assembly of Latex Particles in Wetting Films on Patterned Polymer Surfaces", *J. Phys. Chem. B.,* 2002, *106*(9); 2217-2223.
39. Al-Mawaali, S.; Bemis, J.; Akhremitchev, B. B.; Janesko, B; Walker,. G. C. "Study of Polydispersity of Grafted PDMS Surfaces Using Single Molecule Atomic Force Microscopy", *J. Phys. Chem. B*, 2001, 105, 3965-3971.
40. Bemis, J.; Walker, G. C. "Constant Drag Force Associated with Polymer-Polymer Interactions in Bad Solvents" *J. Phys. Chem. B.,* in revision.

BIBLIOGRAPHY

1. Xu, X.; Friedman, G.; Humfeld, K.D.; Majetich, S.A. and Asher, S.A., Synthesis and Utilization of Monodisperse Superparamagnetic Colloidal Particles for Magnetically Controllable Photonic Crystals. Chemistry of Materials, 2002, 14, (3), 1249-1256.

2. Xu, X.; Friedman, G., Humfeld, K.D.; Majetich, S.A., and Asher, S.A., Superparamagnetic Photonic Crystals. Advanced Materials, 2001, 13, (22), 1681-1684.

3. Xu, X,; Majetich, S.A.; and Asher, S.A. Mesoscopic Monodisperse Ferromagnetic Colloids Enable Magnetically Controlled Photonic Crystals. J. Am. Chem. Soc., 2002, 124, (46), 13864-13868.

4. Wang, W. and Asher, S.A. Photochemical Incorporation of Silver Quantum Dots in Monodisperse Silica Colloids for Photonic Crystal Applications. J. Am. Chem. Soc., 2001, 123, (50), 12528-12535.

5. Reese, C.E.; Guerrero, C.D.; Weissman, J.M.; Lee, K. and Asher, S.A. Synthesis of Highly Charged, Monodisperse Polystyrene Colloidal Particles for the Fabrication of Photonic Crystals. J. of Colloid and Interface Science, 2000, 232, 76-80.

6. Akhremitchev, B.B; Walker G.C.; Apertureless Scanning Near-Field Infrared Microscopy of Rough Polymeric Surface. Langmuir, 2001, (17), 2774-2781. and Akhremitchev, B.B.; Sun, Y.; Stebounova, L.; Walker, G. C. Monolayer-Sensitive Infrared Imaging of DNA Stripes Using Apertureless Near-Field Microscopy. Langmuir, 2002, (18), 5325-5328.

7. Chen, J.; Liu, H.; Weimer, W. A.; Halls, M. D.; Waldeck, D. H.; Walker, G. C., Noncovalent Engineering of Carbon Nanotube Surfaces by Rigid Functional Conjugated Polymers. J. Am. Chem. Soc., 2002, 124, 9036-9037.

8. Sun, Y.; Walker, G. C., Two-Dimensional-Self-Assembly of Latex Particles in Wetting Films on Patterned Polymer Surfaces, J. Phys. Chem. B., 2002, 106, (9), 2217-2223.

9. Ahner, J.; Nanoworkbench for Imaging, Analysis, Manipulation and excitation of individual nanostructures, MST News, 199, 4, (16).

10. Mawhinney, D.B.; Naumenko, V.; Kuznetsova, A.; Yates, J.T., Jr.; Liu, J. and Smalley, R.E. Infrared spectral evidence for the etching of carbon nanotubes: Ozone oxidation at 298 K. J. Am.Chem. Soc., 2000, 122, 2383-2384.

11. Kuznetsova, A.; Mawhinney, D.B.; Naumenko, V.; Yates, J.T. Jr.; Liu, J. and Smalley, R.E., Enhancement of adsorption inside of single-walled nanotubes: opening the entry ports. Chem. Phys. Lett., 2000. 321, 292-296 (2000).

12. Kuznetsova, A.; Yates, J.T. Jr.; Liu, J. and Smalley, R.E., Physical adsorption of xenon in open single walled carbon nanotubes: Observation of a quasi-one-dimensional confined Xe phase. Journal of Chemical Physics, 2000. 112, 9590-9598.

13. Patil, N.G. and Levy, J. Low-Noise Variable-Temperature Preamplifier for Piezoelectric Tuning Fork Force Sensors, Rev. Sci Instrum. 2002, 73, (2), 486.

14. Mezhenny, S.; Lyubinetsky, I.; Levy, J. and Yates, J.T., Jr., Field induced growth of a quantum dot from Ge_2H_6 precursor gas using the scanning tunneling microscope. Journal of Vacuum Science & Technology B, 2001, 19, (2), 567-568.

15. Guise, O. L.; Ahner, J.W.; Jung, M.-C.; Goughnour, P.C. and Yates, J.T., Jr. Reproducible electrochemical etching of tungsten probe tips. 2002, 2 (191).

Appendix A.

Reprint of "Synthesis and Utilization of Monodisperse Superparamagnetic Colloidal Particles for Magnetically Controllable Photonic Crystals"

Synthesis and Utilization of Monodisperse Superparamagnetic Colloidal Particles for Magnetically Controllable Photonic Crystals

Xiangling Xu,[†] Gary Friedman,[‡] Keith D. Humfeld,[§] Sara A. Majetich,[§] and Sanford A. Asher*,[†]

Department of Chemistry, University of Pittsburgh, Pittsburgh, Pennsylvania 15260, Electrical Engineering and Computer Science Department, University of Illinois, Chicago, Illinois 60607, and Department of Physics, Carnegie Mellon University, Pittsburgh, Pennsylvania 15213

We demonstrate fabrication of novel magnetically controllable photonic crystals formed through the self-assembly of highly charged, monodisperse superparamagnetic colloidal spheres. These superparamagnetic monodisperse charged polystyrene particles containing nanoscale iron oxide nanoparticles were synthesized through emulsion polymerization. They self-assemble into crystalline colloidal arrays (CCAs) in deionized water and Bragg diffract visible light. The diffraction from these superparamagnetic CCAs can be controlled by imposition of magnetic fields, which readily alter the CCA lattice constant. We also observe magnetically induced self-assembly of these superparamagnetic particles into CCAs in media such as NaCl aqueous solutions and organic polar solvents, which normally do not permit spontaneous CCA self-assembly. We also find that magnetic fields can strain the face-centered cubic lattice of superparamagnetic CCAs polymerized within hydrogels. The lattice symmetry of this photonic crystal becomes tetragonal. The observed magnetically induced CCA self-assembly enables the development of novel photonic crystal materials and devices.

Monodisperse highly charged colloidal particles spontaneously self-assemble into face-centered cubic (fcc) or body-centered cubic (bcc) crystalline colloidal arrays (CCAs) in low ionic strength aqueous solutions.[1-8] The optical dielectric constant of these colloidal particles, in general, differs from that of the surrounding medium, which results in a periodic variation in the material's refractive index. Similar to the diffraction of X-rays from atomic and molecular crystals, the resulting CCAs Bragg diffract UV, visible, or near-IR light, depending on their lattice constant. These CCAs are the simplest photonic crystals to show band gaps for propagation of electromagnetic radiation in particular directions.[4,6-13]

These CCA photonic crystal materials are of interest because they strongly interact with light and their diffracting periodic structure self-assembles. CCAs that are 100 μm thick show narrow diffraction bands (~5 nm bandwidths) with transmittances[4] of less than 10^{-7}. We

demonstrated earlier that these CCAs could be used as optical notch filters to filter out narrow wavelength intervals.[4,6,14,15] In addition, we have been developing these materials for nonlinear optical limiters and switches by making the refractive index of the colloidal particles nonlinear with respect to the incident light intensity.[16-18]

In addition to their utility for fabricating classical optical devices, there is also the possibility that these CCAs could be used to chemically fabricate 3-D photonic band gap materials.[19-24] These 3-D photonic band gap materials would have no eigenmodes for propagation of

(9) Biswas, R.; Sigalas, M. M.; Subramania, G.; Ho, K. M. *Phys. Rev. B* 1999, *57*, 3701–3705.
(10) Busch, K.; John, S. *Phys. Rev. E* 1999, *58*, 3896–3905.
(11) Rundquist, P. A.; Jagannathan, S.; Kasavamoorthy, R.; Brnardic, C.; Xu, S.; Asher, S. A. *J. Chem. Phys.* 1991, *94*, 711–717.
(12) Kesavamoorthy, R.; Jagannathan, S.; Rundquist, P. A.; Asher, S. A. *J. Chem. Phys.* 1991, *94*, 5172–5179.
(13) Rundquist, P. A.; Kesavamoorthy, R.; Jagannthan, S.; Asher S. A. *J. Chem. Phys.* 1991, *95*, 8546–9551.
(14) Flaugh, P. L.; O'Donnell, S. E.; Asher, A. S. *Appl. Spectrosc.* 1984, *38*, 847–950.
(15) Asher, S. A.; Flaugh, P. L.; Washinger, G. *Spectroscopy* 1989, *1*, 26–31.
(16) Pan, G. S.; Kesavamoorthy, R.; Asher, S. A. *Phys. Rev. Lett.* 1997, *78*, 3860–3863.
(17) Pan, G. S.; Kesavamoorthy, R.; Asher, S. A. *J. Am. Chem. Soc.* 1999, *120*, 6525–9530.
(18) Holtz, J.; Weissman, J.; Pan, G.; Asher, S. A. *Mater. Res. Soc.* 1998, *23*, 44–50.
(19) Yablonovitch, E. *J. Phys.: Condens. Matter* 1993, *5*, 2443–2460.
(20) Joannopoulos, J. D.; Meade, R. D.; Winn, J. N. *Photonic Crystals*; Princeton University Press: Princeton, NJ, 1995.
(21) Ho, K. M.; Chan, C. T.; Soukoulis, C. M. *Phys. Rev. Lett.* 1990, *65*, 3152–3155.
(22) Yablonovitch, E.; Gmitter, T. J. *Phys. Rev. Lett.* 1991, *67*, 2295–2299.

* To whom correspondence should be addressed. Tel: (412) 624-9570. Fax: (412) 924–0599. E-mail: asher@pitt.edu.
† University of Pittsburgh.
‡ University of Illinois.
§ Carnegie Mellon University.
(1) Krieger, I. M.; O'Neill, F. M. *J. Am. Chem. Soc.* 1968, *90*, 3114–3120.
(2) Hiltner, P. A.; Krieger, I. M. *J. Phys. Chem.* 1969, *73*, 2386–2389.
(3) Carlson, R. J.; Asher, S. A. *Appl. Spectrosc.* 1984, *38*, 297–304.
(4) Rundquist, P. A.; Photinos, P.; Jagannathan, S.; Asher, S. A. *J. Chem. Phys.* 1999, *91*, 4932–4941.
(5) Spry, R. J.; Kosan, D. J. *Appl. Spectrosc.* 1986, *40*, 792.
(6) Asher, S. A. U.S. Patents 4,627,689, 1986 and 4,632,517, 1986.
(7) Tarhan, I. I.; Watson, G. H. *Phys. Rev. Lett.* 1996, *76*, 315–319.
(8) Pradhan, R. D.; Bloodgood, J. A.; Watson, G. H. *Phys. Rev. B* 1997, *55*, 9503–9507.

electromagnetic radiation in particular spectral intervals and thus would show many unusual properties, with profound technological implications.[9,10,19,20]

Unfortunately, it appears that fcc or bcc CCA photonic crystals that contain dielectric spheres in lower refractive index media cannot show 3-D photonic band gaps.[19] Other crystal structures, such as the diamond structure,[21] for example, can show 3-D photonic band gaps. However, at present, methods to promote the self-assembly of these types of structures have not been demonstrated.

It has been suggested that optically anisotropic spherical colloidal particles[22-24] could be used to chemically fabricate 3-D photonic band gap materials. The anisotropy would perturb the fcc array symmetry[10] sufficiently enough to split the degeneracy of the Brillouin zone. This might increase the angular width of the photonic band gaps to approach the requirements for a 3-D photonic band gap material. Unfortunately, spherical colloidal particles cannot form anisotropic arrays unless the spherically symmetric interparticle interaction symmetry is perturbed.

Here, we demonstrate the fabrication of novel magnetically controllable photonic crystals formed through the self-assembly of highly charged, monodisperse superparamagnetic colloidal spheres. These superparamagnetic, monodisperse, and charged polystyrene particles, containing nanoscale iron oxide nanoparticles, were synthesized through emulsion polymerization.[25,26] They self-assemble into CCAs in deionized water and Bragg diffract visible light.

The diffraction from these superparamagnetic CCAs can be controlled by the imposition of magnetic fields, which readily alter the CCA lattice constant. We also observe magnetically induced self-assembly of these superparamagnetic particles into CCAs in media such as NaCl solutions and organic polar solvents, which normally do not permit spontaneous CCA self-assembly.

We find that magnetic fields can strain the fcc lattice of the superparamagnetic CCAs polymerized within hydrogels.[27-29] The lattice symmetry of this photonic crystal becomes tetragonal. Thus, this magnetically induced CCA self-assembly enables the development of novel photonic crystal materials and applications.

Experimental Section

Synthesis of Iron Oxide Nanoparticles. Nanoscale iron oxide was prepared by the coprecipitation of ferric and ferrous ions in ammonium hydroxide solution.[30-34] A 10.8 g portion of $FeCl_3 \cdot 6H_2O$ (J. T. Baker) and 4.0 g $FeCl_2 \cdot 4H_2O$ (Sigma) were dissolved in 50 mL of water. The resulting solution was poured with vigorous stirring into 500 mL of a 1.0 M NH_4OH solution. The resulting black precipitate was collected with a magnet. A 500 mL portion of 1 M tetramethylammonium hydroxide

(TMAOH, Aldrich) solution was added to the precipitate, and the mixture was sonicated for 1 h. After that, 6.3 g of oleic acid and 1.0 g of sodium dodecyl benzene sulfonate (SDBS, Alcolac) were added to modify the magnetic colloid surface properties.[35]

Synthesis of Superparamagnetic Polymer Particles. We modified the procedure of Yanase[26] to produce superparamagnetic, highly charged, and monodisperse polystyrene–iron oxide composite colloidal particles. These particles were synthesized by emulsion polymerization of styrene by using a jacketed cylindrical reaction vessel that contained a reflux condenser, a Teflon mechanical stirrer, and a nitrogen/reagent inlet. The temperature was maintained through the jacket with the use of a circulating temperature bath. A nitrogen blanket and a stirring rate of 350 rpm were maintained throughout the polymerization.

The reaction vessel containing 180 mL of water and 20 mL of the above iron oxide dispersion was deoxygenated for 30 min. A 30 mL portion of styrene (St, Aldrich), 3.0 mL of methyl methacrylate (MMA, Aldrich), and 0.2 g of sodium styrene sulfonate (NaSS, Polyscience) were then added, and the temperature was increased to 70 °C when 2.0 g of APS (ammonium persulfate, Aldrich) was added to initiate the polymerization. The polymerization was carried out for 5 h.

The emulsion polymerization product appeared brown. A magnet was used to harvest the particles containing the iron oxide nanoparticles. We estimated from the magnetization measurements and the reaction stoichiometry that ~3.5% of the polystyrene particles contained iron oxide particles.

Characterization of Nanosize Iron Oxide and Magnetic Polymer Composite Particles. X-ray powder diffraction studies utilized a Philips X'PERT system. A Zeiss EM 902A was used to measure the transmission electron micrographs. Energy dispersive X-ray fluorescence spectrometry (EDS, JEOL 35 CF) was used for qualitative elemental determinations. Flame atomic absorption was used to quantitatively measure the iron oxide content in the polystyrene–iron oxide composite particles. The surface charge density was determined by conductometric titrations of the particles with NaOH. A Brookhaven Z-90 plus light scattering photometer was used to measure hydrodynamic diameters and the ζ-potentials.

A Quantum Design MPMS superconducting quantum interference device (SQUID) magnetometer was used to determine the magnetic properties of the iron oxide nanoparticles and the polystyrene–iron oxide composite particles at room temperature between ±50 KOe.

Polymerized CCA Fabrication. The suspension of polystyrene–iron oxide composite particles, which was dialyzed against pure water and then further deionized with ion-exchange resin, self-assembles into CCAs due to the electrostatic repulsion between these highly charged particles.

Polymerized CCAs (PCCAs)[27-29] were prepared by dissolving acrylamide (Fluka) or hydroxyethyl methacrylate (HEMA, Polysciences), cross-linkers such as N,N-methylenebisacrylamide (BAM, Fluka) or ethylene glycol dimethacrylate (EGDMA), and a UV photoinitiator such as diethoxyacetophenone (DEAP, Acros) in a diffracting suspension containing the polystyrene–iron oxide composite particles. This mixture was injected into a cell consisting of two quartz plates, separated by a 125 μm Parafilm spacer. The cell was exposed to UV light from a Blak-Ray (365 nm) mercury lamp to initiate polymerization. After 60 min of exposure, the PCCA was removed from

(23) Haus, J. W.; Sozuer, H. S.; Inguva, R. *J. Mod. Opt.* **1992**, *39*, 1991–2005.
(24) Li, Z. Y.; Wang, J.; Gu, B. Y. *Phys. Rev. B* **1998**, *58*, 3721–3729.
(25) Noguchi, H.; Yanase, N.; Uchida, Y.; Suzuta, T. *J. Appl. Polym. Sci.* **1993**, *48*, 1539–1547.
(26) Yanase, N.; Noguchi, H.; Asakura, H.; Suzuta, T. *J. Appl. Polym. Sci.* **1993**, *50*, 765–776.
(27) Asher, S. A.; Holtz, J.; Liu, L.; Wu, Z.; *J. Am. Chem. Soc.* **1994**, *116*, 4997–4999.
(28) Holtz, J. H.; Asher, S. A. *Nature* **1997**, *389*, 929–932.
(29) Weissman, J. M.; Sunkara, H. B.; Tse, A. S.; Asher, S. A. *Science* **1996**, *274*, 959–960.

(30) Kang, Y. S.; Risbud, S.; Rabolt, J. F.; Stroeve, P. *Chem. Mater.* **1996**, *8*, 2209–2211.
(31) Sauzedde, F.; Elaissari, A.; Pichot, C. *Colloid Polym. Sci.* **1999**, *277*, 846–955.
(32) Liz, L.; Quintela, A.; Mira, J.; Rivas, J. *J. Mater. Sci.* **1994**, *29*, 3797–3801.
(33) Perez, J. A.; Quintela, M. A.; Mira, J.; Rivas, J.; Charles, S. W. *J. Phys. Chem. B* **1997**, *101*, 8045–8047.
(34) Lee, J.; Isobe, T.; Senna, N. *J. Colloid Interface Sci.* **1996**, *177*, 490–494.
(35) Shimoiizaka, J.; Nakatsuka, K.; Chubachi, R.; Sato, Y. *Nippon Kagaku Kaishi* **1979**, 6–9.

Table 1. Comparison of X-ray Diffraction Measurements of Our Iron Oxide Nanoparticles and Polystyrene−Iron Oxide Nanocomposite Particles to That of Different Iron Oxide Structures

nanoscale iron oxide		PSt composite	bulk γ-Fe$_2$O$_3$		bulk Fe$_3$O$_4$	
d (Å)	intensity	d (Å)	d (Å)	intensity	d (Å)	intensity
2.95	37	2.94	2.95	34	2.97	70
2.51	100	2.52	2.52	100	2.53	100
2.10	30	2.09	2.08	24	2.10	70
1.70	18	1.70	1.70	12	1.71	60
1.81	40	1.61	1.81	33	1.81	85
1.48	56	1.48	1.48	53	1.48	85

the cell. Alternatively, the PCCA was thermally polymerized using 2,2′-azobisisobutyronitrile (AIBN, Aldrich) as the initiator. The polymerization was performed at 65 °C for 2 h.

Diffraction Measurements. The diffraction spectra of the CCA and PCCA were measured by using a model 440 CCD UV-vis spectrophotometer (Spectral Instruments, Inc.) coupled to a 6 around 1 reflectance probe optical fiber. Transmission measurements were measured by using a Perkin-Elmer Lambda 9 absorption spectrophotometer. The CCA and PCCA samples were oriented normal to the incident light beam.

Results and Discussion

1.0. Characterization of Superparamagnetic Polystyrene Particles.

1.1. X-ray Diffraction Characterization. We used X-ray diffraction (XRD) to determine the structure of our iron oxide nanoparticles, which were produced by coprecipitation of ferric and ferrous chloride in ammonia, and of our polystyrene−iron oxide composite particles (Figure 1). The XRD spectra are identical, indicating that the iron oxide structure was not changed during the emulsion polymerization.

There are many different possible iron oxide structures such as magnetite (Fe$_3$O$_4$), hematite (α-Fe$_2$O$_3$), maghemite (γ-Fe$_2$O$_3$), or ferric hydroxide (β-FeOOH). Although our particles show XRD d spacings close to those of both magnetite and maghemite, which are inverse spinel structures, the relative diffraction intensities indicate that they are closer to maghemite than magnetite (Table 1). The increased oxygen content may result from the oxidation of our particles in air.[31−34]

1.2. Transmission Electron Microscopy Measurements. Figure 2 shows transmission electron microscopy (TEM) of the iron oxide nanoparticles and the polystyrene−iron oxide composite particles. The iron oxide nanoparticles have a broad size distribution (2−15 nm) with an average diameter of ∼10 nm.

The polystyrene−iron oxide composite particles have a number average particle diameter of 134 nm (essentially identical to their hydrodynamic diameter measured by light scattering in 5 mM KCl). These particles show a polydispersity of 7.5%. TEM shows that the iron oxide particles occur as clumps within the polystyrene particles. EDS (Figure 3) shows the expected iron peaks.

1.3. Magnetization Measurements. Figure 4 shows SQUID magnetometer measurements of the iron oxide nanoparticles and the polystyrene−iron oxide composite particles. Neither coercivity nor remanence was observed. Thus, the particle magnetic moments relax to their equilibrium magnetic state within the measurement time. Thus, these monodisperse polystyrene−iron oxide composite particles are superparamagnetic and, as shown below, are attracted to regions of high
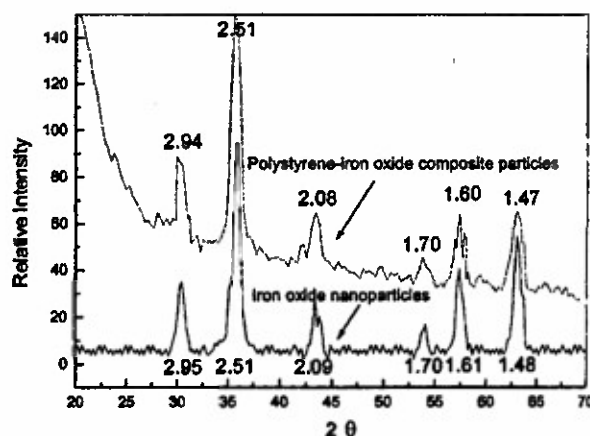
Figure 1. X-ray powder diffraction pattern (Cu Kα radiation) of the nanoscale iron oxide and polystyrene−iron oxide composite particles. The lattice spacings (in Å) and the relative diffraction intensities indicate that the iron oxide structure is γ-Fe$_2$O$_3$.

magnetic field divergence, ∇H. The saturation magnetizations of the iron oxide nanoparticles and polystyrene−iron oxide composite particles are 72.8 and 12.7 emu g^{-1}, respectively. This ratio of saturation magnetization (17.4%) is essentially identical to the weight fraction of iron oxide in the polystyrene−iron oxide composite particles found by atomic absorption measurements (17.0 wt %, assuming Fe$_2$O$_3$). The average saturation magnetic moment per polystyrene−iron oxide composite particle, μ_{pt}, is 1.48 × 10^{-14} emu.

1.4. Colloidal Particle Surface Charge. Our conductometric titration measurements show a polystyrene−iron oxide composite particle surface charge density of 6.3 μC cm^{-2}. We measure a ζ-potential of −55 mV for these particles in a 5 mM KCl solution.

2.0. Magnetic Field Induced Superparamagnetic CCA Self-Assembly.

2.1. Effect of Magnetic Field on the Self-Assembly in Deionized Water. These superparamagnetic, monodisperse, and highly charged particles self-assemble in deionized water into CCAs that Bragg diffract light in the visible region. In the absence of a magnetic field, their spontaneously self-assembled CCA lattice constant is determined solely by the particle number density and the crystal structure.

When a permanent magnet is brought close to the CCA, an additional force $F_m = \nabla(\mu H)$ occurs, which causes the superparamagnetic particles to be attracted to the local magnetic field gradient maximum, where μ is the magnetic field dependent particle magnetic moment. Based on the magnetization curve shown in Figure 4, we calculated a magnetic packing force, $F_m = -4.0 \times 10^{-11}$ dynes per particle, for a 2.7 KOe magnetic field with a gradient of 3.56 KOe cm^{-1}.

The presence of the magnetic field induces a magnetic moment, which generates an interparticle magnetic moment−magnetic moment repulsive force, $F_{mr} = 3(\mu_{pt}^2/d^4)$, in the plane perpendicular to the magnetic field and an attractive interparticle force in the direction parallel to the field, $F_{ma} = -6(\mu_{pt}^2/d^4)$. In the presence of a 2.7 KOe magnetic field with a gradient of 3.56 KOe cm^{-1}, the nearest-neighbor spacing of our particles is (center-to-center) $d = 198.6$ nm (Figure 6).

Using the above interparticle magnetic moment interaction expressions, we calculated a maximum mag-
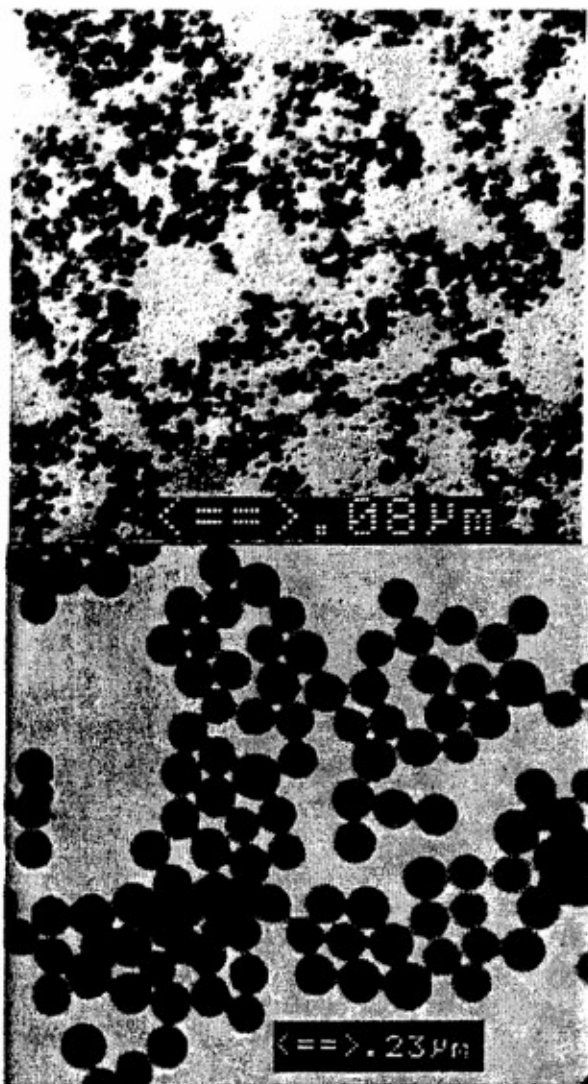
Figure 2. Transmission electron microscopy measurement of nanoscale iron oxide (top) and polystyrene—iron oxide composite particles (bottom). The iron oxide particles have a broad size distribution from 2 to 15 nm, with a number average diameter of ~10 nm. The polystyrene particle average diameter is 134 nm, with a polydispersity of 7.5%. The aggregates of iron oxide nanoparticles appear as black dots in the center of the larger polystyrene—iron oxide composite particles.

Figure 3. Energy dispersive X-ray fluorescence spectrometry of polystyrene—iron oxide composite particles. The peak due to Fe is clearly evident, while the strong Cu peak is derived from the copper grid used to support the sample.
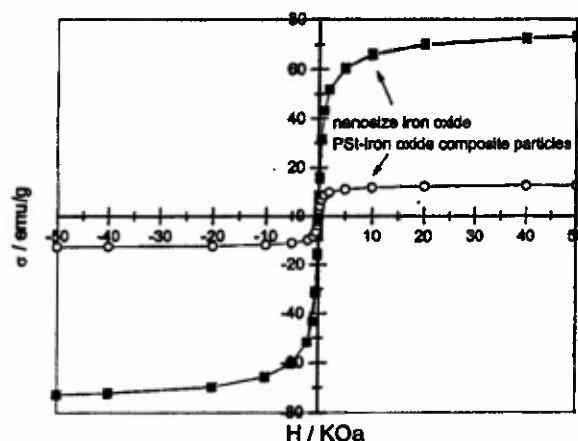
Figure 4. SQUID measurements of nanoscale iron oxide and polystyrene—iron oxide composite particles at room temperature. Neither coercivity nor remanence was observed for both samples. The lack of hysteresis indicates that these particles are superparamagnetic.

netic dipole repulsive force in the plane perpendicular to the external magnetic field of $F_{mr} = 4.2 \times 10^{-9}$ dynes per particle and a maximum interparticle magnetic dipole attractive force parallel to the external magnetic field of $F_{ma} = -8.4 \times 10^{-9}$ dynes per particle. These forces are ~50-fold smaller than the interparticle electrostatic repulsive force, $F_{er} = \pi \epsilon \zeta^2 \kappa a e^{-\kappa h} = 4.0 \times 10^{-7}$ dynes per particles (a dielectric constant $\epsilon = 78.4$, a ζ-potential $\zeta = -55$ mV, a Debye length $1/\kappa = 15$ nm, a particle radius $a = 67$ nm, and an interparticle surface-to-surface distance $h = 68$ nm).

The presence of a 2.7 KOe magnetic field with a gradient of 3.56 KOe cm^{-1} causes a 5.2 nm mm^{-1} gradation of the nearest-neighbor particle distance along the field. We can model this phenomenon, most simply, if we consider a square lattice of spherical particles and consider layers 1, 2, and 3 in detail (Figure 5). Given

that the Figure 5 magnetic field diverges toward the right, the nearest particle distance d_{12} is slightly smaller than d_{23}. The uniaxial magnetic field packing force, $F_m = -4.0 \times 10^{-11}$ dynes per particle, compresses the lattice and establishes a static equilibrium balance between the magnetic packing force and the electrostatic repulsive force between particles.

We calculate that the magnetic dipole—magnetic dipole attractive forces between particles along the field direction is much smaller than the difference in the electrostatic repulsive forces between particles. For example, for particle 2, $F_{ma,12} - F_{ma,32} = 1.5 \times 10^{-13}$ dynes per particle, while $F_{er,12} - F_{er,32} = 2.9 \times 10^{-11}$ dynes per particle. The lattice constant is essentially determined by the balance between the magnetic packing force and the interparticle electrostatic repulsive force. The lattice constant should be a minimum at the locus of the magnetic field gradient maximum and should increase as the gradient decreases.

The magnetic dipole—magnetic dipole interaction terms should lead to a tetragonal distortion of the fcc

Monodisperse Superparamagnetic Colloidal Particles

Chem. Mater., Vol. 14, No. 3, 2002 1253

No Magnetic Field   In Magnetic Field
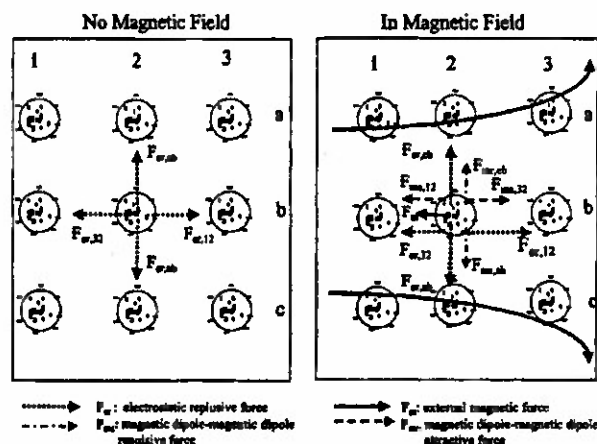
Figure 5. Forces on superparamagnetic particles within a CCA in the absence and presence of a magnetic field. In the absence of a magnetic field, the interparticle electrostatic repulsive forces F_{er} balance each other. The magnetic field induces additional magnetic packing forces, F_m, additional magnetic dipole–magnetic dipole repulsive forces, F_{mr} that are perpendicular to the magnetic field, and additional magnetic dipole attractive forces, F_{ma} that are parallel to the magnetic field. The CCA is compressed along the magnetic field. Thus, the magnetic packing force F_m on layer 2 is balanced by both the electrostatic repulsive force $(F_{er,12}-F_{er,32})$ and the magnetic dipole–magnetic dipole attractive force $(F_{ma,12}-F_{ma,32})$.

lattice, where the interparticle spacing increases in the plane perpendicular to the field, while along the field the interparticle spacing decreases. We can roughly estimate the magnitude of this change by calculating the DLVO interparticle distance change required to balance the additional forces. We estimate that the resulting tetragonal distortion would be associated with ~0.1% of alterations in the interparticle distances. This small tetragonal distortion will be difficult to measure experimentally. Therefore, we see no difference between the diffraction normal and parallel to the external magnet field.

Figure 6 shows the observed influence of a magnetic field on a thick CCA assembly of superparamagnetic particles. The diffraction peaks, shown in the Figure 6 insert, result from the CCA 111 fcc planes, which are the most densely packed and are oriented parallel to the glass surface. For 180° backscattering, the diffraction peak blue-shifts from ~560 to ~428 nm as the magnetic field gradient increases from 1.5–5.4 KOe cm^{-1}. Using Bragg's law for the CCA $(\lambda_0 = 2nd \sin \theta$, where λ_0 is the wavelength of the diffracted light in a vacuum, n is the average CCA refractive index, d is the 111 plane spacing, and $\theta = 90°$ is the Bragg glancing angle), we calculate[3] that the 111 plane spacing decreases from 206 to 153 nm. As expected, the plane spacing is a minimum at the locus of the magnetic field gradient maximum and increases as the gradient decreases.

We also measured the magnetic field dependence of diffraction from a thin superparamagnetic CCA (Figure 7). In the absence of a magnetic field, this sample diffracts 910 nm light. The 910 nm peak results from diffraction by the fcc 111 plane, while the peak at half this wavelength (455 nm) results from second-order diffraction from a host of planes that fortuitously diffract

simultaneously.[36] Usually, the second-order diffraction is much more intense than the first-order diffraction.[36] Presumably, the decreased second-order intensity results from absorption by the iron oxide nanoparticles.

As this thin sample is translated toward the magnet, the diffraction wavelength observed in back diffraction decreases from 904 to 850 nm, where the field divergence maximizes at 4.7 KOe cm^{-1}. As expected, the lattice spacing varies linearly with the magnetic field gradient, since the magnetic packing force is proportional to the gradient of the magnetic field.

This experiment also demonstrates that the diffraction of this spontaneously self-assembled CCA can be controlled by magnetic fields. To our knowledge, this is the first example of a magnetically controlled photonic crystal.

2.2. Magnetic Field Induced CCA Self-Assembly. Normally, CCA self-assembly does not occur spontaneously in high ionic strength aqueous solutions or in organic solvents, due to the screening of the electrostatic repulsion between colloidal particles. However, these superparamagnetic particles can be magnetically induced to self-assemble into CCAs within high ionic strength aqueous solutions and in polar organic solvents.

When an external magnetic field is applied to the dispersion of superparamagnetic particles, the field gradient exerts a force on the particles and induces a slow phase separation of the superparamagnetic particles into a high volume fraction phase near the wall of the sample holder. These particles slowly pack into highly ordered CCAs at the container wall. Although a similar high volume fraction (~20%) of these charged colloidal particles would show some ordering, highly ordered CCAs would not be formed since the high particle volume fraction would be too viscous to allow the CCAs to anneal into a well-ordered fcc structure. The system would form a glassy state.

This magnetic self-assembly mechanism is probably similar to the mechanisms responsible for the formation of close-packed CCA ordering during gravitational settling and the mechanism responsible for the formation of close-packed CCA ordering during fluid flow assembly,[39] under oscillatory shear,[40] or evaporative deposition,[41] where the 111 fcc crystal planes grow out from the surface as the next layer of particles pack against the previously stacked layer.

Figure 8A shows diffraction spectra of magnetically assembled CCAs in solutions of increasing NaCl concentrations. In pure water, the 111 plane of the fcc lattice diffracts ~620 nm light, while in 0.16 mM NaCl, the diffraction blue-shifts to 575 nm and further blue-shifts to 420 nm for a 4 mM NaCl concentration. Thus, these superparamagnetic particles pack more densely as the screening increases for the higher NaCl ionic strengths. It is somewhat surprising that we observe a minimum neighbor spacing as large as ~180 nm, since

(36) Liu, L.; Asher, S. A. *J. Am. Chem. Soc.* 1997, *119*, 2729–2732.
(37) Sogami, I.; Ise, N. *J. Chem. Phys.* 1984, *81*, 6320–32.
(38) Tomita, M.; Ven, T. G. M. *J. Phys. Chem.* 1985, *89*, 1291–1296.
(39) Parik, S. H.; Xia, Y. *Langmuir* 1999, *15*, 266–273.
(40) Vickreva, O.; Kalinina, O.; Kumacheva, E. *Adv. Mater.* 2000, *12*, 110–102.
(41) Jiang, P.; Bertone, J. F.; Hwang, K. S.; Colvin, V. L. *Chem. Mater.* 1999, *11*, 2132–2140.
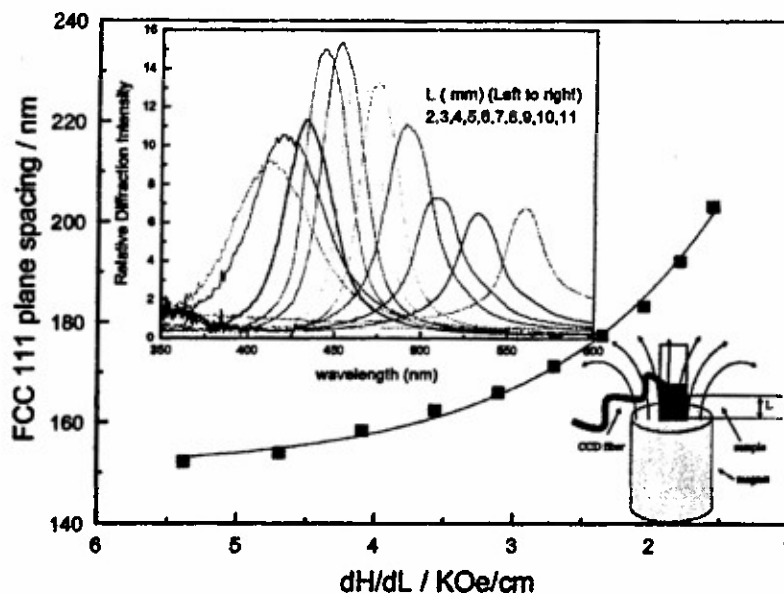
Figure 6. Influence of the average magnetic field gradient, dH/dL, on the lattice constant of a thick CCA composed of 134 nm superparamagnetic particles in deionized water (4.2 vol %). The top inset shows the dependence of the diffraction peak wavelength on the distance from the magnet. In the lower right is an experimental schematic showing the CCA on top of a permanent magnet. A reflectance optical fiber probe connected to a CCD spectrometer is used to measure the diffraction spectrum. The spatial dependence of the magnetic field strength was measured by using a Hall probe.
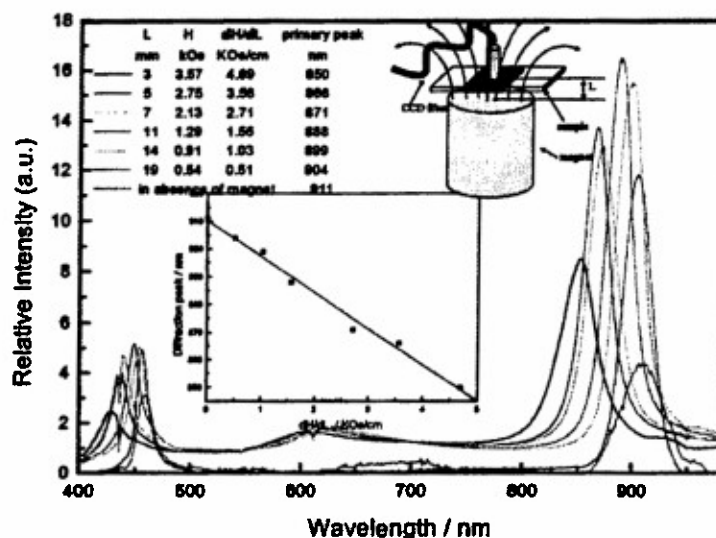
Figure 7. Influence of a magnetic field on the packing of a thin CCA composed of 134 nm superparamagnetic particles in deionized water (2.5 vol %). The inset shows the linear dependence of the diffraction wavelength on the magnetic field gradient. The diffracted wavelength linearly decreases from 904 to 850 nm as the sample is translated to increase the magnetic gradient.

the actual particle diameter is 134 nm and because 4 mM NaCl solutions have short Debye lengths of 4.8 nm.[37]

Figure 8B shows diffraction spectra of superparamagnetic magnetically self-assembled CCAs in a series of organic solvents. In pure water, the 111 plane diffracts ~530 nm light. The diffraction blue-shifts to 495 nm in dimethyl sulfoxide and to 450 nm in acetonitrile and further blue-shifts to 400 nm in ethanol. The 111 plane spacing decreases linearly as the solvent dielectric constant decreases, as expected from the DLVO theory, which predicts that the electrostatic repulsive forces are proportional to the dielectric constant.[37,38]

3.0. Fabrication of Solid Photonic Crystals. The CCA fluid photonic crystals were rigidized into soft solids by embedding the CCAs into hydrogel polymer matrixes. Previous hydrogel polymerizations to form PCCA required the use of photochemical polymerization to avoid ionic species that would screen the interparticle repulsive interactions which would decrease the CCA ordering.[27-29] In contrast, the magnetically assembled superparamagnetic CCAs can be polymerized in a variety of solvents and by using a variety of initiators.

For example, we assembled our CCA in a deionized aqueous solution, which contained 0.0993 gm mL^{-1} of AM, 0.003 gm mL^{-1} of BAM, and 0.005 gm mL^{-1} of
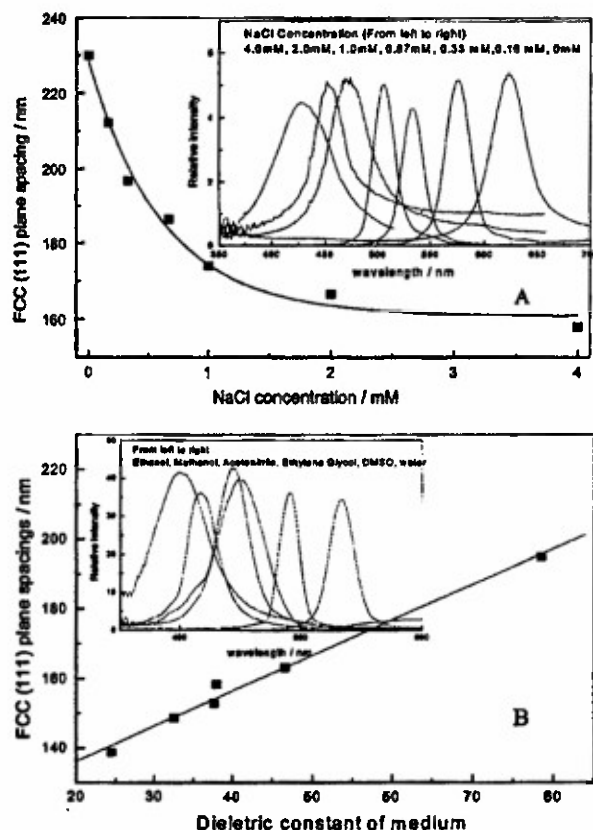
Figure 8. Magnetic field induced packing of superparamagnetic particles in different media in a 4.6 KOe magnetic field with a 6.2 KOe cm^{-1} gradient: (A) magnetic assembly from a 5% particle volume fraction NaCl aqueous solution; (B) magnetic self-assembly from 10% particle volume fraction dispersions in ethanol (24.5), methanol (32.6), acetonitrile (37.7), ethylene glycol (38), DMSO (46.6), and water (78). The dielectric constant of each solvent is given in parentheses.

AIBN (the thermal initiator). In the absence of a magnetic field, we introduced this CCA solution into a thin cell which we heated to 60 °C to polymerize the PCCA. Figure 9 shows that this magnetically assembled CCA diffracted 450 nm light before and after polymerization. This PCCA had only ~3% cross-linking. After polymerization, we removed this PCCA from the cell and exposed it to deionized water, which caused the hydrogel to swell and the lattice to expand, which red-shifted the diffraction to 580 nm.

These PCCA hydrogels can also be polymerized in the presence of magnetic fields under conditions that are incompatible with spontaneous CCA self-assembly. Figure 10 shows the reflection spectra of PCCAs fabricated by the thermal polymerization of AM and BAM in water and by the thermal polymerization of HEMA and EGDMA in ethanol.

As discussed above, the magnetic field can induce a gradient in the lattice constant, where the diffraction wavelength decreases with increased distance from the magnet (Figure 6). This permits fabrication of PCCA photonic crystals where the diffraction wavelengths vary as a function of position.

4.0. Magnetic Response of PCCA. Superparamagnetic PCCA are soft elastic materials that should respond to magnetic fields. Figure 11 shows the mag-
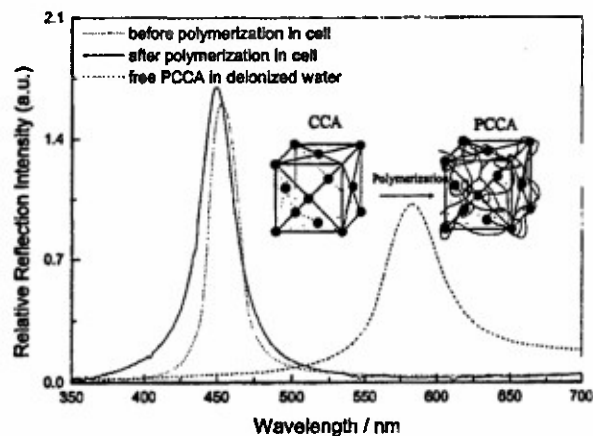
Figure 9. Reflection spectra of CCA in deionized water before and after a thermal hydrogel polymerization initiated with AIBN. The low cross-linking of the PCCA volume resulted in a significant swelling and diffraction red-shift upon removing the PCCA from the polymerization cell and exposing it to deionized water.
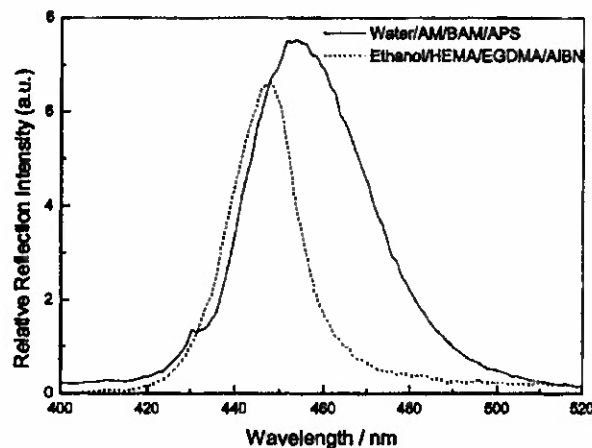
Figure 10. Reflection spectra of PCCA formed by the magnetic assembly of a CCA polymerized in situ, in media which are incompatible with spontaneous CCA self-assembly: (A) aqueous solution containing 7.7 mM APS; (B) ethanol.

netic response of a 500 μm thick PCCA film of superparamagnetic particles made by the thermal polymerization of AM and BAM. One end of the film was held stationary. A magnet was placed next to the free end. The diffraction was measured normal to the film plane. The diffraction from this superparamagnetic PCCA promptly blue-shifted from 787 to 783 nm and, over a period of 60 min, slowly blue-shifted to its equilibrium diffraction of ~777 nm. The magnetic field induced diffraction shift was fully reversible (Figure 11); removal of the magnet caused the diffraction to shift back to its original 787 nm diffraction.

The magnetically induced diffraction shift presumably results from a uniaxial strain on the PCCA. The anisotropic strain induced by the magnetic field elongates the lattice constant along the field direction. Conservation of volume decreases the lattice constant along directions normal to the strain direction and thus decreases the 111 plane lattice constant and blue-shifts the diffraction wavelength. Thus, magnetic fields can be used to tune the diffraction wavelength. Although the diffraction wavelength shift is relatively small in
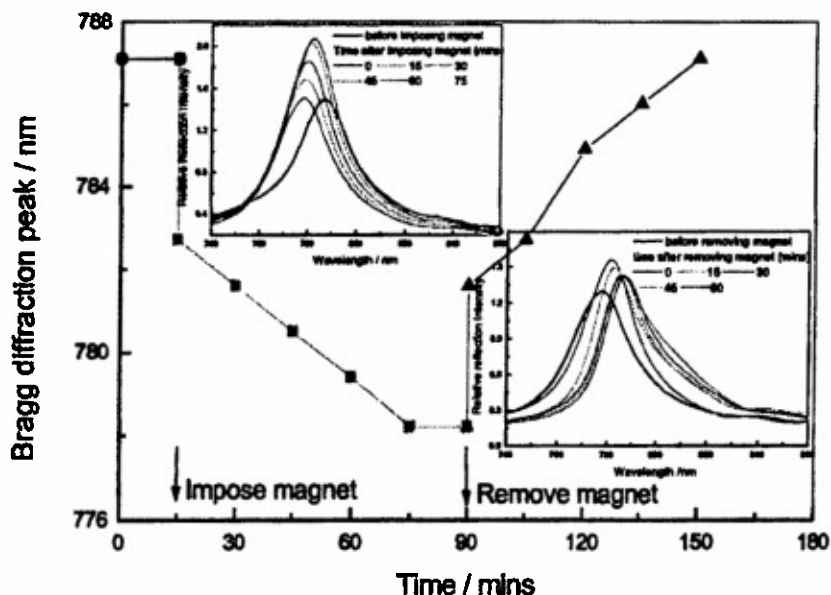
Figure 11. Response of superparamagnetic PCCA film to a 2.4 KOe magnetic field with a 3.2 KOe cm^{-1} gradient. After imposition of the magnetic field, the Bragg diffraction blue-shifted from 787 to 777 nm. This shift was fully reversible; the diffraction red-shifted back to 787 nm after removing the magnetic field.

this example, the use of higher magnetic fields or the use of more elastic superparamagnetic PCCA would give larger wavelength tuning.

The unixial strain on the PCCA causes an anisotropy in the fcc lattice constant, where the lattice constant along the field lines increases while the lattice constants that are perpendicular decrease. Thus, the crystal symmetry changes from the cubic symmetry of the fcc lattice to tetragonal symmetry. This may have significant consequences for the PCCA diffraction properties. These tetragonal lattices may prove to be useful in the fabrication of 3-D photonic band gap materials.

Conclusions

We have demonstrated the fabrication of novel magnetically controllable photonic crystals formed through the self-assembly of highly charged, monodisperse superparamagnetic colloidal spheres. These superparamagnetic monodisperse charged polystyrene particles containing nanoscale iron oxide nanoparticles were synthesized through emulsion polymerization. They self-assemble into CCAs in deionized water and Bragg diffract visible light. The diffraction from these super-

paramagnetic CCAs can be controlled by applying magnetic fields, which readily alter the CCA lattice constant. We also observe magnetically induced self-assembly of these superparamagnetic particles into CCAs in media, such as NaCl aqueous solutions and organic polar solvent, which normally do not permit spontaneous CCA self-assembly. We also find that magnetic fields can strain the fcc lattice of superparamagnetic CCAs polymerized within hydrogels. The lattice symmetry of this photonic crystal becomes tetragonal. The observed magnetically induced CCA self-assembly enables the development of novel photonic crystal materials and devices.

Appendix B.

Reprint of "Superparamagnetic Photonic Crystals"

similar to that of a set of 14 independent molecules in a solution. Conversely, a semi-rigid, optimized acentric organization results in coherent second harmonic emission at the supramolecular level, the corresponding iotensity from tbe dendrimer solution being almost proportional to $N^2_{monomer}\langle\beta^2_{monomer}\rangle$. The $N^2_{monomer}$ dependence assumes a lioear additive model, whereby the individual sub-units follow an interactioo-free oriented gas behavior.

We have, therefore, clear evidence of quasi-optimized octupolar ordering in a dendrimer made of highly nonlinear ruthenium complexes. This is, to the best of our koowledge, the most efficieot type of self-assembled supramolecular octupolar order reported to date. The availability of nonlioear octupolar dendrimers creates attractive possibilities for oaooscale pbotonic applications with other photonic functionalities, such as pertain to luminescence.

[1] D. A. Tomalia, *Adv. Mater.* 1994, 6, 529.
[2] O. R. Newkome, E. He, C. N. Moorefield, *Chem. Rev.* 1999, 99, 1689.
[3] A. W. Bosman, H. M. Janssen, E. W. Meijer. *Chem. Rev.* 1999, 99, 1665.
[4] V. Balzani, S. Campagna, G. Denti, A. Juris, S. Serroni, M. Venturi, *Acc. Chem. Res.* 1998, 31, 26.
[5] S. Li, D. McGrath, *J. Am. Chem. Soc.* 2000, 122, 6795.
[6] A. Adronov, J.-M. J. Fréchet, *Chem. Commun.* 2000, 1701.
[7] A. M. McDonagh, M. G. Humphrey, M. Samoc, B. Lutber-Davies, *Organometallics* 1999, 18, 5195.
[8] S. Yokohama, T. Nakahama, A. Otomo, S. Mashiko, *J. Am. Chem. Soc.* 2000, 122, 3174.
[9] A. M. McDonagh, M. G. Humphrey, M. Samoc, B. Luther-Davies, S. Houbrechts, T. Wada, H. Sasabe, A. Parsoons, *J. Am. Chem. Soc.* 1999, 121, 1405.
[10] J. Zyss, *J. Chem. Phys.* 1993, 98, 6583.
[11] J. Zyss, C. Dhenaut, T. Chauvan, I. Ledoux, *Chem. Phys. Lett.* 1993, 206, 409.
[12] C. Dhenaut, I. Ledoux, I. D. W. Samuel, J. Zyss, M. Bourgault, H. Le Bozec, *Nature* 1995, 374, 339.
[13] V. R. Tballadi, S. Brasselet, H.-C. Weiss, D. Bläser, A. K. Katz, H. L. Carrell, R. Boese, J. Zyss, A. Nangia, G. R. Desiraju, *J. Am. Chem. Soc.* 1998, 120, 2563.
[14] S. Brasselet, J. Zyss, *J. Opt. Soc. Am. B* 1998, 15, 257.
[15] J. Lacour, C. Ginglinger, C. Grivet, G. Bernardinelli, *Angew. Chem. Int. Ed. Engl.* 1997, 36, 608.
[16] O. Maury, J. Lacour, H. Le Bozec, *Eur. J. Inorg. Chem.* 2001, 201.
[17] T. Le Bouder, *Ph.D. Thesis*, University of Rennes, France 2000.
[18] Complete assignmenl of the ¹³C NMR spectra was achieved by means of heteronuclear multiple bond correlation (hmbe) and heteronuclear multiple quantum correlation (hmqc) correlations.
[19] a) R. W. Terhune, P. D. Maker, C. M. Savage, *Phys. Rev. Lett.* 1965, 14, 681. b) K. Clays, A. Persoons, *Phys. Rev. Lett.* 1991, 66, 2980.
[20] I. D. Morrison, R. O. Deoning, W. M. Laidlaw, M. A. Stammers, *Rev. Sci. Instrum.* 1996, 67, 1445.
[21] a) M. A. Pauley, C. H. Wang, *Chem. Phys. Lett.* 1997, 280, 544. b) M. A. Pauley, C. H. Wang, *Rev. Sci. Instrum.* 1999, 70, 1277.
[22] J. Zyss, J.-F. Nicoud, M. Coquillay, *J. Chem. Phys.* 1984, 81, 4160.

Superparamagnetic Photonic Crystals**

By *Xiangling Xu, Gary Friedman, Keith D. Humfeld, Sara A. Majetich*, and *Sanford A. Asher**

There is intense scientific and technological interest in fabricating three-dimensiooal (3D) pbotonic bandgap materials.[1–5] Monodisperse highly charged colloidal particles readily self-assemble to form crystalline colloidal arrays (CCAs) in low ionic strength aqueous solutions.[6–13] They are the simplest photonic crystals showing bandgaps only in particular directions.[1,2,9–16] Though, these CCAs cannot show 3D photonic bandgaps, it may be possible to fabricate 3D photonic bandgap materials from face-centered cubic (fcc) particle arrays by utilizing oriented anisotropic spberes,[17–19] or by perturbiog the array symmetry.[2] Here we show the fabrication of superparamagnetic pbotonic crystals from highly charged, mooodisperse superparamagnetic ~134 nm polystyrene–iron oxide composite colloidal spheres. The lattice spacing of tbese superparamagnetic CCAs can be altered by magnetic fields. Soft solid polymerized CCAs (PCCAs) are synthesized by polymerizing the fcc array of superparamagnetic particles within a hydrogel matrix. Magnetic fields may be utilized to reversibly deform the PCCA lattice in one direction, wbich decreases the lattice symmetry and shifts the diffraction. This breaking of the fcc symmetry may be useful for creating unique photonic bandgap materials.

We modified the procedure of Yanase et al.[20] to produce superparamagnetic, highly charged, monodisperse colloidal particles. These particles were synthesized by emulsion polymerization of styrene, in the presence of ~10 nm iroo oxide particles. The superparamagnetic nanoscale iron oxide particles were produced by the coprecipitation of ferric and ferrous chloride in ammonium hydroxide solution.[21,22] Before emulsion polymerization, the surface of these iron oxide particles was modified by adsorption of oleic acid.[23] Further details are given in the experimental section. After emulsion polymerization, the polystyreoe particles containing iron oxide inclusions were harvested with a magnet. Transmission electron microscopy (TEM) measurements indicate a 134 nm oumber average diameter (polydispersity 7.5 %, Fig. 1). As expected, the polystyrene–iron oxide composite particles are superparamagnetic, and show oo coercivity or remaneoce at room temperature.

[*] Prof. S. A. Asher, Dr. X. Xu
Department of Chemistry, University of Pittsburgh
Pittsburgh, PA 15260 (USA)
E-mail: asher@pitt.edu
Prof. G. Friedman
Electrical Engineering and Compuler Science Department
University of Illinois
Chicago, IL 60607 (USA)
Dr. K. D. Humfeld, Prof. S. A. Majetich
Department of Physics, Carnegie Mellon University
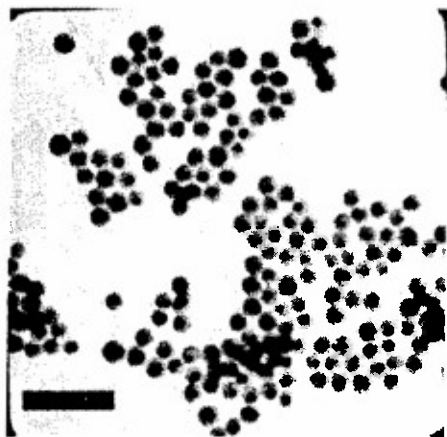Pittsburgh, PA 15213 (USA)

71

Fig. 1. TEM image of monodisperse polystyrene particles containing superparamagnetic nanoparticles. The aggregates of iron oxide nanoparticles appear as black dots in the larger polystyrene spheres. The polystyrene particle average diameter is 134 nm, with a polydispersity of 7.5 %.

These monodisperse superparamagnetic particles self-assemble into CCAs in deionized water, due to electrostatic repulsive interactions between the individual spherical particles. When an inhomogeneous magnetic field is applied to the CCA, an additional force occurs which causes the superparamagnetic particles to be attracted to the maximum of the local magnetic field gradient. Thus, the CCA is compressed along the magnetic field gradient. As shown in Figure 2, the diffraction wavelength blueshifts as the magnetic field and its gradient increases. The lattice constant observed is determined by the balance between the magnetic packing forces and the spherically symmetric interparticle electrostatic repulsive forces. Therefore, the lattice constant is a minimum at the locus of the magnetic field gradient maximum and increases as the gradient decreases.

Normally, CCAs do not self-assemble into highly ordered CCAs in high ionic strength aqueous solutions or in polar organic solvents due to the weak interparticle electrostatic interactions.[24,25] However, for superparamagnetic colloidal particles dispersed in these media, the magnetic field gradient exerts a force on these particles that induces a slow phase separation of these superparamagnetic particles into a high volume fraction phase near the wall of the sample holder. Then, these particles slowly pack into highly ordered CCAs there. Although a similar high volume fraction of these charged colloidal particles shows some ordering, highly ordered CCAs do not form since the high particle volume fraction is too viscous for the CCAs to anneal into a well ordered fcc structure. This magnetic self-assembly mechanism is probably similar to the mechanisms responsible for formation of close packed CCAs ordering during gravitational settling and the mechanism responsible for formation of close packed CCA ordering during fluid flow assembly,[26] where the fcc (111) crystal planes grow out from the surface as the next layer of particles pack against the previously stacked layer. Figure 3 shows the dependence of the diffraction wave-

Fig. 2. Influence of the average magnetic field gradient, dH/dL on the lattice constant of a thick CCA composed of 134 nm superparamagnetic particles in deionized water (4.2 vol.-%). Top inset shows the dependence of the diffraction peak wavelength on the distance from the magnet. The lower right inset is an experimental schematic showing the CCA on top of a permanent magnet, with an optical fiber probe connected to a charge coupled device (CCD) spectrometer to determine the diffraction spectrum. The spatial dependence of the magnetic field was measured using a Hall probe.

Fig. 3. Magnetic field induced packing of superparamagnetic particles in different media in a 4.6 kOe magnetic field with a 6.2 kOe/cm gradient. A) Magnetic assembly from a 5 % particle volume fraction NaCl aqueous solution. B) Magnetic self-assembly from 10 % particle volume fraction dispersions in ethanol (24.5), methanol (32.6), acetonitrile (37.7), ethylene glycol (38), dimethyl sulfoxide (DMSO) (46.6), and water (78). The dielectric constant of each solvent is given in parentheses.

72

length and the fcc (111) plane spacing on the NaCl concentration of aqueous CCAs and on the dielectric constant of a series of polar organic solvent CCAs. The fcc (111) plane spacing decreases as the NaCl cooceotration increases, and as the organic solvent dielectric constant increases.

We can form anisotropic arrays hy embeddiog the superparamagnetic CCA in soft hydrogels and then perturbing the crystal structure with a magnetic field. We dispersed the superparamagnetic particles in an aqueous solution containing acrylamide and bisacrylamide. After the fcc CCA self-assembled, we thermally polymerized it into a hydrogel (PCCA).[27,28] As shown in Figure 4, the superparamagnetic PCCA film fixed on one-end quickly blue shifts from 787 nm to 783 nm upon impositioo of a magnetic field next to the free end. Over an additiooal 60 min the diffraction further blue shifts to

Fig. 4. Response of superparamagnetic PCCA film to a 2.4 kOe magnelie field with a 3.2 kOe/cm gradient. After imposition of the magnetie field the Bragg diffraction blueshifted from 787 nm lo 777 nm. This shift was fully reversible; lhe diffraction redshifted back to 787 om after removing the magnetic field.

an equilihrium value of ~777 nm. This slower process is presumahly associated with the creep of this viscoelastic hydrogel. The resulting anisotropic strain applied by magnetic field on the PCCA film, elongates the lattice constant aloog the field direction. Therefore the lattice constant decreases along directions normal to the strain direction, due to cooservation of volume. As also shown in Figure 4, the magnetic field induced deformation of the superparamagnetic PCCA is fully reversible. The magnetic field can, thus, be used to hoth tune the diffraction wavelength and to alter tbe crystal structure.

In conclusion, tbese monodisperse, highly charged, superparamagnetic colloidal particles enable fabrication of magnetically controlled photonic crystals. In addition, this superparamagnetic particle magnetic self-assemhly fahricates photonic crystals in media that were previously incompatible with CCA formation. This self-assembly in non-aqueous systems enahles utilizatioo of oon-aqueous chemical processing to develop oovel photonic crystal materials aod applications.

Magnetic fields can be used to both alter tbe diffraction wavelength and to control the crystal structure and lattice plane spacing. The magnetic field ioduced perturbation of the PCCA fcc symmetry alters tbe diffraction properties of these materials and creates unique pbotonic crystal materials.

Experimental

Nanoscale iron oxide was prepared by the coprecipitation of ferric and ferrous ions in ammonium hydroxide solution. 10.8 g of $FeCl_3 \cdot 6H_2O$ (J. T. Baker), and 4.0 g $FeCl_2 \cdot 4H_2O$ (Sigma) was dissolved in 50 mL of water. The resultiog solution was poured with vigorous stirriog ioto 500 mL of a 1.0 M $NH_3 \cdot H_2O$ solution. The black precipitate was collected with a magnet. 500 mL of 1 M
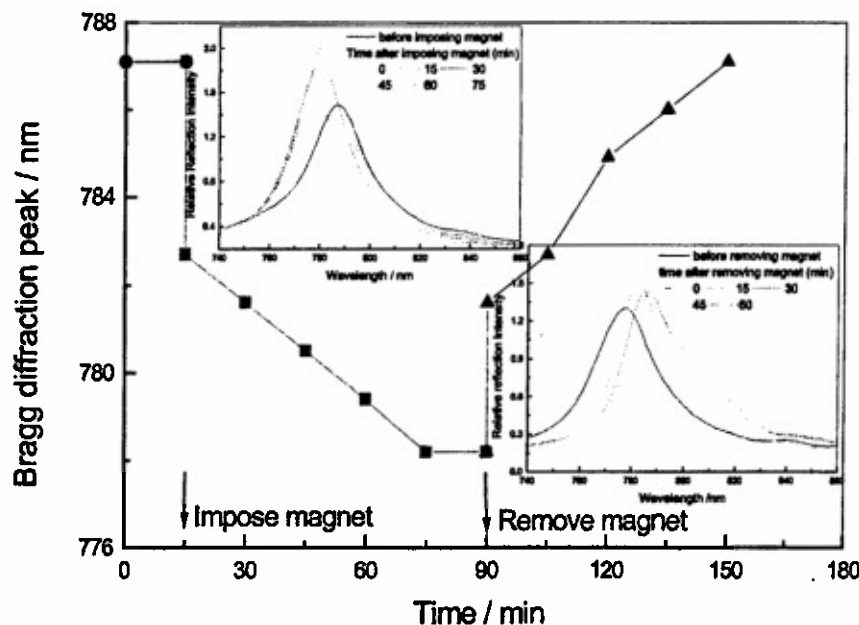
TMAOH (tertramelhylammonium hydroxide, Aldrich) solution was added to the precipitate and the mixture was sonicated for 1 h. Our particles show X-ray diffraction spacing close lo those of both magnetite (Fe_3O_4) and maghemite (γ-Fe_2O_3), which are inverse spinel structures. The relative diffraction intensities indicate that they are closer to maghemite than magnetite. TEM measurements show a broad size distribution (2–15 nm), with an average diameter ~10 nm. At room temperature neither coercivity nor remanence was observed, indicatiog that nanoparticles are superparamagnetic.

Superparamagnetie, monodisperse and charged polystyrene spheres were synthesized by emulsion polymerization in presence of iron oxide nanaoparticles. A jacketed cylindrical reaction vessel was charged with 180 mL of water and 20 mL of the Iron oxide dispersion. After 30 min of deoxygeoating, 30 mL styrene (St, Aldricb), 3.0 mL methyl methacrylate (MMA, Aldrich), and 0.2 g sodium styrene sulfonate (NaSS, Polyscience) were added into the vessel. The temperature was increased to 70 °C and 2.0 g ammonium persulfate (APS, Aldrich) was added to initiate polymerization, which reacted for 5 b. The polystyrene particles containing iron oxide were harvested by a magnet. TEM measurements indicales that these particles are monodisperse with a ~134 nm diameter. Conductometrie titrations show a surface charge of 6.3 $\mu C/cm^2$. Flame atomie absorption and magnetic measurements obtained by using a supercooducting quaotum interference device (SOUID) magnetometer both indicate a 17.1 wt.-% iron oxide content. As expected, the dry magnetic polystyreoe particle powder shows oo coercivity or remanence.

[1] R. Biswas, M. M. Sigalas, G. Subramania, K. M. Ho, *Phys. Rev. B* **1998**, *57*, 3701.
[2] K. Busch, S. John, *Phys. Rev. E* **1998**, *58*, 3896.
[3] E. Yablonovitch, *J. Phys.: Condens. Matter.* **1993**, *5*, 2443.
[4] J. D. Joannopoulos, R. D. Meade, J. N. Winn, *Photonic Crystals*, Princeton University Press, Princeton, NJ **1995**.
[5] K. M. Ho, C. T. Chan, C. M. Soukoulis, *Phys. Rev. Lett.* **1990**, *65*, 3152.
[6] I. M. Krieger, F. M. O'Neill, *J. Am. Chem. Soc.* **1968**, *90*, 3114.
[7] P. A. Hiltner, L. M. Krieger, *J. Phys. Chem.* **1969**, *73*, 2386.
[8] R. J. Carlson, S. A. Asher, *Appl. Spectrosc.* **1984**, *38*, 297.
[9] P. A. Rundquist, P. Photinos, S. Jagannathao, S. A. Asher, *J. Chem. Phys.* **1989**, *91*, 4932.
[10] N. A. Clark, A. J. Hurd, B. J. Ackerson, *Nature* **1979**, *281*, 57.

73

[11] S. A. Asher, *US Patent 4627 689*, 1986. *US Patent 4632 517*, 1986.
[12] I. I. Tarhan, G. H. Watson, *Phys. Rev. Lett.* 1996, 76, 315.
[13] R. D. Pradhan, J. A. Bloodgood, G. H. Watson, *Phys. Rev. B* 1997, 55, 9503.
[14] P. A. Rundquist, S. Jagannathan, R. Kasavamoorthy, C. Brnardic, S. Xu, S. A. Asher, *J. Chem. Phys.* 1991, 94, 711.
[15] R. Kesavamoorthy, S. Jagannathan, P. A. Rundquist, S. A. Asher, *J. Chem. Phys.* 1991, 94, 5172.
[16] P. A. Rundquist, R. Kesavamoorthy, S. Jagannathan, S. A. Asher, *J. Chem. Phys.* 1991, 95, 8546.
[17] E. Yablonovitch, T. J. Gmitter, *Phys. Rev. Lett.* 1991, 67, 2295.
[18] J. W. Haus, H. S. Sozuer, R. Inguva, *J. Mod. Opt.* 1992, 39, 1991.
[19] Z. Y. Li, J. Wang, B. Y. Gu, *Phys. Rev. B* 1998, 58, 3721.
[20] N. Yanase, H. Noguchi, H. Asakura, T. Suzuta, *J. Appl. Polym. Sci.* 1993, 50, 765.
[21] F. Sauzedde, A. Elaissari, C. Pichot, *Colloid Polym. Sci.* 1999, 277, 846.
[22] Y. S. Kang, S. Risbud, J. F. Rabolt, P. Stroeve, *Chem. Mater.* 1996, 8, 2209.
[23] J. Shimoiizaka, K. Nakatsuka, R. Chubachi, Y. Sato, *Nippon Kagaku Kaishi* 1976, 6.
[24] I. Sogami, N. Ise, *J. Chem. Phys.* 1984, 81, 6320.
[25] M. Tomita, T. G. M. Ven, *J. Phys. Chem.* 1985, 89, 1291.
[26] S. H. Park, Y. Xia, *Langmuir* 1999, 15, 266.
[27] S. A. Asher, J. Holtz, L. Liu, Z. Wu, *J. Am. Chem. Soc.* 1994, 116, 4997.
[28] J. M. Weissman, H. B. Sunkara, A. S. Tse, S. A. Asher, *Science* 1996, 274, 959.

Core–Shell Structures Formed by the Solvent-Controlled Precipitation of Luminescent CdTe Nanocrystals on Latex Spheres**

By *Igor L. Radtchenko, Gleb B. Sukhorukov, Nikolai Gaponik, Andreas Kornowski, Andrey L. Rogach,** and Helmuth Möhwald*

A novel method of fabricating core–shell structures, comprising monodisperse submicrometer-sized latex spheres as cores and nanocrystals as shells, is demonstrated. The coating was formed by a solvent-controlled precipitation of CdTe nanocrystals from aqueous solutions either by adding ethanol or by changing the pH. The proper choice of the concentration of the latex particles and nanocrystals provided a homogeneous and complete coverage of colloidal cores with luminescent shells of desirable thickness in the range of 15–40 nm as confirmed by transmission electron microscopy (TEM) and confocal fluorescence microscopy.

Engineering of colloidal surfaces is a current topic of applied chemistry in the field of developing new materials with

[*] Dr. A. L. Rogach,[+] Dr. N. Gaponik,[+] A. Kornowski
Institute of Physical Chemistry, University of Hamburg
D-20146 Hamburg (Germany)
E-mail: rogach@chemie.uni-hamburg.de
I. L. Radtchenko, Dr. G. B. Sukhorukov, Prof. H. Möhwald
Max Planck Institute of Colloids and Interfaces
D-14424 Potsdam (Germany)
[+] On leave from: Physico-Chemical Research Institute, Belarusian State University, Minsk, Belarus.

tailored properties. Research on composite colloidal particles (core–shell structures) has received sufficient interest due to various applications expected in the areas of coatings, electronics, photonics, and catalysis.[1] Formation of shells on colloidal particles yields composites possessing properties significantly different from that of the core, e.g., increased stability, adhesion, surface area, magnetic and optical properties. There are several approaches to fabricate shells on colloidal cores, which involve, for instance, surface chemical reactions,[2] precipitation of inorganic salts[3,4] or colloidal particles,[5] and the layer-by-layer (LbL) assembly of charged macromolecules or nanoparticles.[6–9] All these methods have their own advantages and drawbacks for the preparation of coated particles, resulting in different uniformity, thickness, and composition of the shells.

Colloidally synthesized semiconductor nanocrystals with tailored surface properties (through the proper choice of stabilizing molecules) and sufficiently strong luminescence tunable through the particle size[10] can successfully be used for the fabrication of luminescent shells on colloidal particles. It was shown[11,12] that a shell structure comprising polyelectrolyte multilayers and luminescent CdTe nanocrystals[13] can be deposited on latex particles using the step-wise approach of LbL alternate adsorption. This method of the nanocomposite assembly provides a defined shell composition on the colloidal core with a shell thickness being a function of the number of deposited layers. The LbL approach can be applied to coat charged colloidal particles of different shapes with sizes ranging from 0.1 to 10 μm.[6–9] However, the procedure is sufficiently time consuming because it requires the removal of non-bound polyelectrolytes and nanocrystals at each step of the assembly. The presence of the polymer component in the nanocrystal-containing shells is also not always desirable. The nanoparticles must carry sufficient charge to be used in the LbL assembly technique.

We have developed and report in this paper a new method of coating colloidal particles through the controlled precipitation of CdTe nanocrystals by means of their aggregation in solution on latex spheres. The approach demonstrated is a variation of heteroaggregation phenomena in colloidal environments. The aggregation of nanocrystals on colloidal cores was induced, for the first time, by the solvent–non-solvent-pair precipitation technique, which was previously successfully used to separate semiconductor nanocrystals by size.[14,15] Colloidal cores statistically harvest aggregated nanocrystals (Scheme 1). Alternatively, precipitation of nanocrystals can be driven by changing their solubility through the change of pH of the aqueous solution.[5] The technique described herein allows the production of uniform complete shells in one step on a time scale of minutes, which is a drastic acceleration in comparison to the multi-step LbL approach that needs hours or even days to complete. The thickness of the shells can be effectively controlled through the proper choice of the concentration ratio of colloidal particles serving as cores and the precipitated species. As considered theoretically,[16] there are certain concentration windows for colloidal cores and the

74

Appendix C.

Reprint of "Mesoscopic Monodisperse Ferromagnetic Colloids Enable Magnetically Controlled Photonic Crystals"

Mesoscopic Monodisperse Ferromagnetic Colloids Enable Magnetically Controlled Photonic Crystals

Xiangling Xu,[†] Sara A. Majetich,[‡] and Sanford A. Asher[*,†]

*Contribution from the Department of Chemistry, University of Pittsburgh,
Pittsburgh, Pennsylvania 15260 and Deportment of Physics, Carnegie Mellon University,
Pittsburgh, Pennsylvania 15213*

Received May 14, 2002

Abstract: We report here the first synthesis of mesoscopic, monodisperse particles which contain nanoscopic inclusions of ferromagnetic cobalt ferrites. These monodisperse ferromagnetic composite particles readily self-assemble into magnetically responsive photonic crystals that efficiently Bragg diffract incident light. Magnetic fields can be used to control the photonic crystal orientation and, thus, the diffracted wavelength. We demonstrate the use of these ferromagnetic particles to fabricate magneto-optical diffracting fluids and magnetically switchable diffracting mirrors.

Introduction

There is intense interest in the nanoscale and mesoscale chemical fabrication of novel photonic crystal materials whose properties can be externally controlled.[1-20] For example, a variety of photonic crystals have been developed which are responsive to their thermal, chemical, and photonic environments.[1-5,19,20] Most recently, we developed the first magnetically controllable photonic crystals[16,17] which were fabricated through the magnetic self-assembly of monodisperse, highly charged, superparamagnetic composite polystyrene colloidal particles; these polystyrene particles contained superparamagnetic iron oxide nanoparticles. We demonstrated a new magnetic field induced crystalline colloidal array (CCA) self-assemble motif

based on the attraction of these superparamagnetic particles to the location of magnetic field gradient maxima.

We also formed soft solid polymerized CCA (PCCA) by polymerizing the face-centered cubic (fcc) array of superparamagnetic particles within a hydrogel matrix. Magnetic fields can reversibly deform the superparamagnetic PCCA fcc lattice to shift the Bragg diffraction wavelength. We should note that Gates et al.[18] demonstrated another approach to fabricating superparamagnetic photonic crystals, where monodisperse polystyrene colloids were assembled into a close packed fcc array in an ferrofluid containing nanometer-sized magnetite. The magnetic nanoparticles filled the interstices between the polystyrene particles.

We report here the fabrication of the first monodisperse, mesoscopic ferromagnetic particles. These novel ferromagnetic particles contain nanoscopic inclusions of cobalt ferrite in mesoscopic polystyrene colloids. These ferromagnetic composite particles readily self-assemble into magnetically responsive photonic crystals that efficiently diffract light.

Magnetic fields can control the ferromagnetic photonic crystal orientation and position in space as well as its diffracted wavelength. We demonstrate the use of these materials to fabricate magneto-optical photonic crystal fluids that act as magnetically controlled light modulators. These materials also form magnetically tunable optical switches and mirrors.

Results and Discussion

Synthesis and Characterization of Ferromagnetic Polystyrene Particles. Ferromagnetic composite colloidal particles were synthesized by emulsion polymerization, using methods similar to those used to synthesize our mesoscopic superparamagnetic particles.[16,17] First, ~20-nm cobalt ferrite particles were formed by coprecipitation of $CoCl_2$ and $FeCl_3$ (mole ratio 1:2) in a 1 M tetramethylammonium hydroxide (TMAOH) solution.[21-24] The XRD measurements shown in Figure 1 indicate that the resulting nanocrystals are in an inverse spinel

* To whom correspondence should be sent. Telephone: (412) 624-8570.
Fax: (412) 624-0588. E-mail: asher@pitt.edu.
  † University of Pittsburgh.
  ‡ Carnegie Mellon University.
(1) Asher, S. A.; Holtz, J.; Weissman, J.; Pan, G. *MRS Bull.* 1998, 23, 44-50.
(2) Holtz, J. H.; Asher, S. A. *Nature* 1997, 389, 829-32.
(3) Weissman, J. M.; Sunkara, H. B.; Tse, A. S.; Asher, S. A. *Science* 1996, 274, 959-60.
(4) Pan, G. S.; Kesavanorthy, R.; Asher, S. A. *Phy. Rev. Lett.* 1997, 78, 3860-3.
(5) Tse, A. S.; Wu, Z.; Asher, S. A. *Macromolecules* 1995, 28, 6533-8.
(6) Asher, S. A. U.S. Patent 4,627,689 (1986) and 4,632,517 (1986).
(7) Murray, C. B.; Kagan, C. R.; Bawendi, M. G. *Science* 1995, 270, 1335-8.
(8) Springholz, G.; Holy, V.; Pinczolits, M.; Bauer, G. *Science* 1998, 282, 734-7.
(9) Johnson, S. A.; Ollivier, P. J.; Mallouk, T. E. *Science* 1999, 283, 963-5.
(10) Sun, S.; Murray, C. B.; Weller, D.; Folks, D. L.; Moser, A. *Science* 2000, 287, 1989-92.
(11) Graf, C.; Blaaderen, A. *Langmuir* 2002, 18, 524-34.
(12) Breen, M. L.; Dinsmore, A. D.; Pink, R. H.; Qadri, S. B.; Ratna, B. R. *Langmuir* 2001, 17, 903.
(13) Toader, O.; John, S. *Science* 2001, 292, 1133-5.
(14) Jiang, P.; Bertone, J. F.; Colvin, V. L. *Science* 2001, 291, 453-7.
(15) Muller, M.; Zentel, R.; Maka, T.; Romanov, S. G.; Torres, C. M. S. *Chem. Mater.* 2000, 12, 2508-12.
(16) Xu, X.; Friedman, G.; Humfeld, K. D.; Majetich, S. A.; Asher, A. S. *Adv. Mater.* 2001, 13, 1681-3.
(17) Xu, X.; Friedman, G.; Humfeld, K. D.; Majetich, S. A.; Asher, A. S. *Chem. Mater.* 2002, 14, 1249-56.
(18) Gates, B.; Xia, Y. *Adv. Mater.* 2001, 13, 1605-8.
(19) Gu, Z.; Fujishima, A.; Sato, O. *J. Am. Chem. Soc.* 2000, 122, 12387-8.
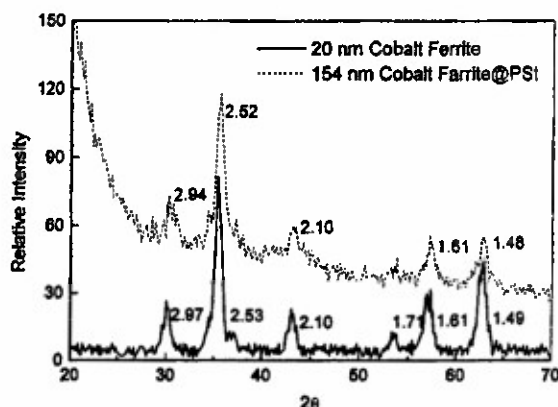(20) Debord, J. D.; Lyon, L. A. *J. Phys. Chem. B* 2000, 104, 6327-31.

Figure 1. X-ray powder diffraction pattern (Cu Kα radiation) of 20-nm cobalt ferrite and 154-nm polystyrene cobalt ferrite composite particles.
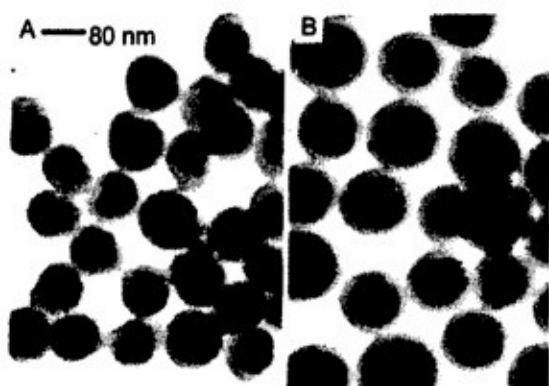

Figure 2. TEM image of ferromagnetic polystyrene composite particles containing cobalt ferrite nanoparticles. (A) TEM image of 120-nm composite particles with a size polydispersity of 7%. The particles contain 14 wt % cobalt ferrite. (B) TEM image of 154-nm composite particles with a size polydispersity of 6%. The particles contain 5 wt % cobalt ferrite. The cobalt ferrite particles appear as black dots inside the composite particles.

structure.[21,25] Since only tiny differences occur between the XRD of Fe_3O_4 and $CoFe_2O_4$, XRD cannot be used directly to determine purity. The cobalt/iron ratio (1:2.2) in the crystal measured by atomic absorption is consistent with pure $CoFe_2O_4$ nanocrystals.

These cobalt ferrite particles were incorporated within polystyrene colloidal particles by emulsion polymerization.[26] The resulting monodisperse ferromagnetic particles were harvested with a magnet (~10% yield).

We can vary the cobalt ferrite loading in the polystyrene spheres by varying the concentration of cobalt ferrite nanoparticles in the emulsion polymerization reaction. For example, Figure 2 shows the TEM images of ~120-nm (polydispersity 7%, Figure 2A) and ~154-nm (polydispersity 6%, Figure 2B) ferromagnetic particles. The nanoscale cobalt ferrite particles

(21) Vincente, J.; Delgado, A. V.; Plaza, R. C.; Duran, J. D. G.; Gonzalez-Caballero, F. *Langmuir* 2000, *16*, 7954–61.
(22) Kang, Y. S.; Risbud, S.; Rabolt, J. F.; Stroeve, P. *Chem. Mater.* 1996, *8*, 2209–11.
(23) Tang, Z. X.; Sorensen, C. M.; Klabunde, K. J.; Hadjipanayis, G. C. *J. Colloid Interface Sci.* 1991, *146*, 38–51.
(24) Sauzedde, F.; Elaissari, A.; Pichot, C. *Colloid Polym. Sci.* 1999, *277*, 846–55.
(25) Rondinone, A. J.; Samia, A. C. S.; Zhang, Z. J. *J. Phys. Chem. B* 1999, *103*, 6876–80.
(26) Yanase, N.; Noguchi, H.; Asakura, H.; Suzuta, T. *J. Appl. Polym. Sci.* 1993, *50*, 765–76.
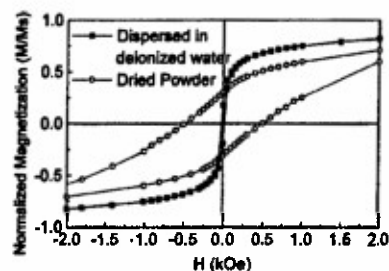

Figure 3. Magnetic behavior of a dried powder and a deionized water dispersion (1.6 wt %) of 120-nm ferromagnetic particles. The magnetization observed was normalized to the saturation magnetization (M_S) observed at 50 kOe. The powder magnetization curve clearly shows hysteresis, while the solution dispersion does not. The larger reduced magnetization (M/M_S) observed for the liquid dispersion presumably results from the ability of these particles to orient with their easy magnetic axes along the field.

appear as black inclusions in TEM images. The cobalt ferrite loading is obviously smaller in the 154-nm (Figure 2B) particles. Although the mesoscopic polystyrene ferromagnetic composite particles are reasonably monodisperse, the TEM indicates significant polydispersity in the cobalt ferrite loading.

We used a SQUID magnetometer to measure the magnetic properties of these particles at room temperature. For a dried powder of the ~120-nm particles, we observe hysteresis that demonstrates ferromagnetism (Figure 3), a saturation magnetization, M_S, at 50 kOe of 7.2 emu/g (7.0×10^{-15} emu/particle) and a remanent magnetization of 1.7 emu/g (1.6×10^{-15} emu/particle). The remanent magnetization persists indefinitely. For the ~154-nm particles, we observe a saturation magnetization, M_S, of 2.5 emu/g (4.9×10^{-15} emu/particle) and a remanent magnetization of 0.55 emu/g (1.0×10^{-15} emu/particle). From the 51 emu/g measured saturation magnetization of a powder of our nanoscopic cobalt ferrite particles, we calculate a 14 wt % cobalt ferrite fraction in the 120-nm particles and a 5 wt % cobalt ferrite fraction in 154-nm composite particles.

Magnetically Controlled Orientation of Single Ferromagnetic Particle. Inhomogeneous magnetic fields generate translational forces on all magnetic particles,[27] while homogeneous magnetic fields induce physical torques only on ferromagnetic particles. This torque attempts to rotate the particles to align their magnetic moments along the magnetic field. In contrast, superparamagnetic particles show only Néel rotation, where the magnetic moments of the particles rotate, but not the particles themselves. In a superparamagnet, Néel rotation is rapid relative to the measurement time, but in small ferromagnetic particles, Brownian rotation predominates.[27]
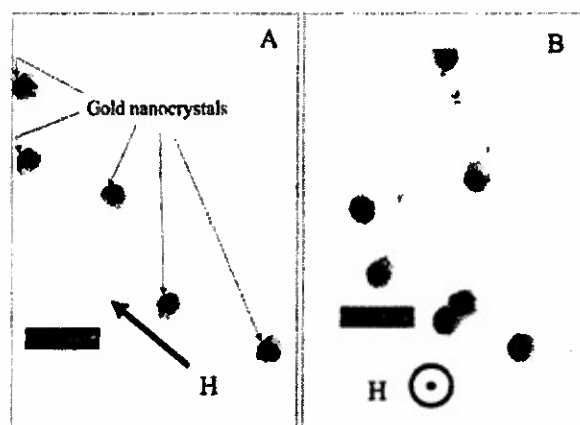
The Figure 3 room temperature hysteresis occurs because the magnetic torque is insufficient to reorient the entire sample and Néel relaxation in the ferromagnet is negligibly slow. In contrast, no hysteresis is observed for these same particles in a 1.6 wt % aqueous dispersion at room temperature (Figure 3) because they rapidly rotate and align with the field within the measurement time. The larger reduced magnetization (M/M_S) observed for the liquid dispersion compared to that of the powder results from the ability of spheres to rotate until their easy magnetic axes lie parallel to the field.

Thus, a strong magnetic field induces a permanent magnetic moment in these particles. A weaker magnetic field can then

(27) Cullity, B. D. *Introduction to Magnetic Materials*; Addison-Wesley: Reading, MA, 1972.
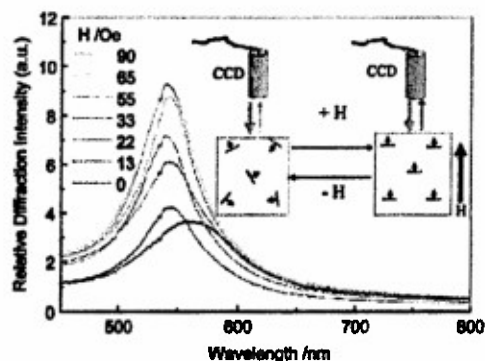
Figure 4. Demonstration of magnetically controlled orientation of magnetized ferromagnetic particles. The magnetized ferromagnetic particles are labeled with a gold patch on their north pole. An aqueous drop containing the magnetized particles was dried onto the TEM grid in the presence of a 300-Oe magnetic field. (A) The magnetic field was oriented as shown within the TEM grid plane. The outward normals to the gold patches orient along the magnetic field direction. (B) The magnetic field was oriented normal to the TEM grid plane, pointed toward the observer. The outward normals to the gold patches point towards the observer.

act on this moment to control the orientation of these ferromagnetic particles. We demonstrated this by coating the ~120-nm ferromagnetic particles with a thin silica shell[28] and then drying these ferromagnetic particles on a substrate. A permanent magnetic moment was induced in these particles by applying a 6-kOe magnetic field normal to the substrate plane. The north pole of each sphere was labeled by sputtering gold onto the exposed north pole surfaces.[29]

These labeled spheres were then redispersed into deionized water, and a drop of this dispersion was dried onto a TEM grid in a homogeneous 300 Oe magnetic field, either oriented within the TEM grid plane or normal to it. TEM measurements of the particles (Figure 4A and B) clearly show that the 300-Oe magnetic field rotates the ferromagnetic particles to orient their magnetic moments along the applied magnetic field. Figure 4A shows that the spheres orient with the outward normals to the gold patches pointing toward the upper left corner, in the direction of the applied field. When the magnetic field is normal to the TEM grid plane, the gold patches orient with their normals toward the observer (Figure 4B).

Fabrication and Response of Ferromagnetic Photonic Crystals to External Magnetic Fields. Our monodisperse ferromagnetic colloidal particles can be induced to magnetically self-assemble into CCA in a manner similar to that demonstrated for superparamagnetic particles.[16,17] This magnetic self-assembly is induced by placing a magnet next to a cell containing magnetic particles; the particles are attracted by the magnetic field divergence and slowly pack into a three-dimensional array against the wall of a container. Because the particles have a large surface charge, they also spontaneously self-assemble into a fcc CCA photonic crystal in low ionic strength aqueous solution, as a result of the strong electrostatic repulsion between neighboring particles. These photonic crystals can be transiently magnetized by a strong magnetic field; the CCA will possess a

(28) Tissot, I.; Novat, C.; Lefebvre, F.; Bourgeat-Lami, E. *Macromolecules* 2001, *34*, 5737–9.
(29) Takei, H.; Shimizu, N. *Langmuir* 1997, *13*, 1865–8.

Figure 5. Response of ferromagnetic composite PCCA fragments to an external magnetic field. In the absence of a magnetic field, the fiber optic probe only detects weak back diffraction from the small number of fragments fortuitously oriented with their 111 directions parallel to the fiber optic probe. Application of a magnetic field orients the fragments with their normals along the fiber optic probe, which results in an increased diffraction intensity. The small magnetic field induced diffraction wavelength blue shift occurs because the magnetic field was not exactly parallel to the fiber optic axis.

macroscopic magnetic moment because of the summed contribution of the magnetic moments of the individual ferromagnetic colloidal spheres of the CCA. However, the magnetization quickly dissipates because of the free rotations of the spheres within the CCA.

However, we can create a macroscopically magnetized photonic crystal by polymerizing a CCA of ferromagnetic particles into a hydrogel (PCCA) to lock the position and orientation of these particles relative to one another. We should observe a net magnetization of the ferromagnetic PCCA such that magnetic fields can now be used to control the orientation of this ferromagnetic photonic crystal in order to control the wavelength of light diffracted by the photonic crystal.

For example, we self-assembled ~154-nm monodisperse high surface charged ferromagnetic polystyrene particles (5 wt % cobalt ferrite) into a CCA which we then polymerized into a ~35-μm thick acrylamide hydrogel film.[30] The PCCA fcc 111 plane, which orients parallel to the plane of the PCCA film, has a lattice spacing such that it Bragg diffracts 540-nm normally incident light. We used a 3-kOe magnetic field to magnetize the PCCA such that its magnetic moment was oriented normal to the PCCA film. We then shredded this PCCA into small fragments (~100 μm × ~100 μm × 35 μm). Each PCCA fragment possesses a macroscopic magnetic moment because of the summed contribution of the magnetic moments of the individual ferromagnetic colloidal spheres.
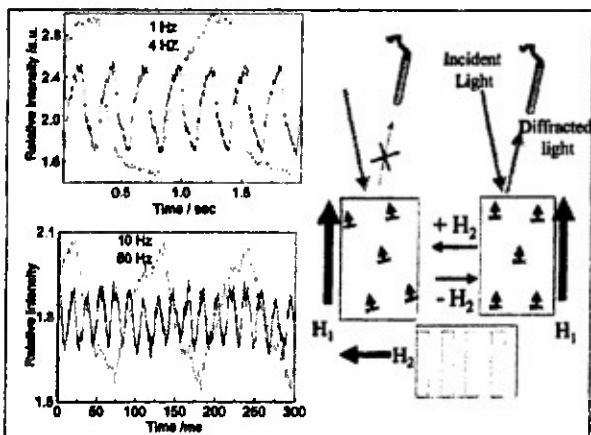
We measured the diffraction from this PCCA film dispersion by using a nine-around-one fiber optic probe. Incident white light from the central fiber is back diffracted by the PCCA fragments and collected by the nine surrounding fibers (Figure 5). In the absence of a magnetic field, we only detect weak diffraction from the small number of fragments fortuitously oriented with their 111 directions almost parallel to the fiber optic probe.[31] Application of a magnetic field orients the fragment normals parallel to the fiber optic probe axis; the diffracted intensity increases with the magnetic field strength.

(30) Asher, S. A.; Holtz, J.; Liu, L.; Wu, Z. *J. Am. Chem. Soc.* 1994, *116*, 4997–8.
(31) Reese, C. E.; Baltusavich, M. E.; Keim, J. P.; Asher, S. A. *Anal. Chem.* 2001, *73*, 5038–42.

Figure 6. Response of magnetic PCCA to oscillating magnetic field. The PCCA was magnetized with its magnetic moment parallel to the fcc 111 direction, which was normal to the plane of the PCCA film fragments. One electromagnet gave a constant $H_1 = 75$ Oe field along the sample cell normal, while another magnet imposed a perpendicular magnetic field, H_2, which alternated between 0 and 30 Oe. Thus, the net magnetic field orientation oscillates between being normal to the sample cell surface and lying 22° off of the normal. This causes the ferromagnetic PCCA fragment orientation to oscillate and causes an oscillation in diffraction intensity.

Figure 6 shows the response of this magneto-optical fluid to a periodically varying magnetic field. A 543.5-nm He−Ne laser beam was incident as shown, and a fiber optic was oriented such that it collected the diffracted light at a Bragg glancing angle of ~75°. This diffraction occurs only for those photonic crystals fragments which were oriented such that their normals bisected the angle between the incident and diffracted beam. One electromagnet gave a constant $H_1 = 75$ Oe field along the sample cell normal, while another magnet imposed a perpendicular magnetic field, H_2, which oscillated as a step function between 0 and 30 Oe (Figure 6). This resulted in a net magnetic field direction whose orientation periodically switched between being along the sample cell normal and 22° from the normal. The ferromagnetic photonic crystal fragments reorient in response to the oscillating field which results in an oscillating diffraction intensity (Figure 6).

At the lowest frequencies (<1 Hz), the fragments can fully orient with the field direction within each cycle; thus, a maximum modulation occurs for the diffracted light. At 1 Hz, we observe both a slow and fast rise time within each cycle. These two rise times probably result from a bimodal population of fragment sizes; the smaller fragments completely and promptly orient, while the largest fragments do not have sufficient time to fully orient. Higher frequency modulations (>4 Hz) do not permit fragments to fully orient; thus, the modulation depth of the diffraction decreases (Figure 7).

This dispersion of ferromagnetic photonic crystal fragments acts as a magneto-optical fluid whose diffraction and transmission is controlled by incident magnetic fields. The maximum response rate observed was slightly greater than 70 Hz. This response rate is determined by the reorientation rate, which depends on the magnetically induced torque and the rotational friction. The response rate is expected to dramatically increase as the ferromagnetic photonic crystal fragment size decreases.

We also fabricated a reversible photonic crystal mirror by gluing together two ferromagnetic PCCAs ($2 \times 5 \times 0.2$ mm^3)
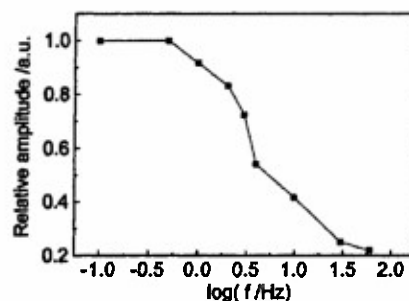
Figure 7. Dependence of the magnetically induced diffraction intensity modulation on the magnetic field switching frequency.
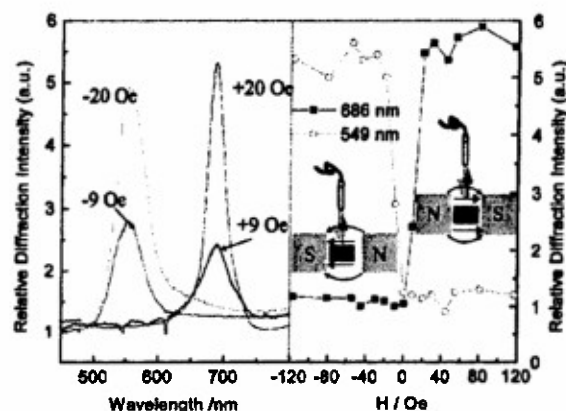
Figure 8. Response of ferromagnetic composite PCCA fragments to an external magnetic field. Two PCCA films with different lattice constants were glued together with their 111 planes parallel to each other. The PCCA magnetic moment was aligned to lie within the 111 plane of the PCCA film. The PCCA film was suspended on a water surface, with the magnetic moment and both PCCA 111 plane normals parallel to the water surface. The figure shows the experimental configuration viewed from the top; the CCD fiber optic probe axis was oriented within the plane of the water surface and normal to the external magnetic field. If the magnetic field points to the left, the PCCA Bragg diffracts ~549-nm light. If the magnetic field is reversed, the PCCA Bragg diffracts ~686-nm light.

with different fcc lattice constants. These PCCAs diffract 549- and 686-nm light incident perpendicular to their 111 planes. We then magnetized this photonic crystal laminate with a 3-kOe magnetic field oriented within the PCCA 111 planes. This laminate was sufficiently thick that we were able place this film on the surface of water, with the PCCA 111 plane normal lying parallel to the plane of the water surface. This film could only rotate about an axis normal to the water surface.

Figure 8 shows the magnetic field orientation dependence of this PCCA film diffraction observed by our nine-around-one fiber optic probe, whose axis was oriented within the plane of the water surface and normal to external magnetic field direction. The left panel shows that a magnetic field can control the PCCA film orientation and can switch the surface of the film facing the fiber optic probe. When the magnetic field points to the left, we observe diffraction of 549-nm light. A 180° reversal of the magnetic field rotates the PCCA film such that the other PCCA face diffracts 686-nm light. The diffraction efficiency increases as the field strength increases from 9 to 20 Oe because of the increase in the alignment of the film. This is most clearly shown in the right panel of Figure 8, which shows the dependence of the diffraction wavelength and intensity as a function of the magnetic field strength.

Experimental Section

Synthesis of Cobalt Ferrite Nanoparticles. Nanoscale cobalt ferrite was prepared by the coprecipitation of ferric and cobalt ions in tetramethylammonium hydroxide (TMAOH, Aldrich) solution.[21-24] A 10.8-g amount of $FeCl_3 \cdot 6H_2O$ (J. T. Baker) and 4.8 g of $CoCl_2 \cdot 4H_2O$ (Sigma) were dissolved in 50 mL of water. The resulting solution was poured with vigorous stirring into 500 mL of a 1.0 M TMAOH solution. The resulting brown precipitate was separated by centrifugation. A 500-mL volume of 1 M TMAOH solution was added to the precipitate, and the mixture was sonicated for 1 h. After that, 6.3 g of oleic acid and 1.0 g of sodium dodecyl benzene sulfonate (SDBS, Alcolac) were added to modify the magnetic colloid surface properties.

Synthesis of Ferromagnetic Polymer Particles. Monodisperse ferromagnetic polystyrene cobalt ferrite composite colloidal particles were synthesized by a method similar to that previously used for the synthesis of superparamagnetic particles.[16,17,26] These ferromagnetic particles were synthesized by emulsion polymerization of styrene in the presence of cobalt ferrite, in a jacketed cylindrical reaction vessel that contained a reflux condenser, a Teflon mechanical stirrer, and a nitrogen/reagent inlet. The temperature was maintained through the jacket with the use of a circulating temperature bath. A nitrogen blanket and a stirring rate of 350 rpm were maintained throughout the polymerization.

The reaction vessel containing 180 mL of water and 20 mL of the above cobalt ferrite dispersion was deoxygenated for 30 min. A 30-mL aliquot of styrene (St, Aldrich), 3.0 mL of methyl methacrylate (MMA, Aldrich), and 0.2 g of sodium styrene sulfonate (NaSS, Polyscience) were then added. The temperature was increased to 70 °C, and 2.0 g of APS (ammonium persulfate, Aldrich) was added to initiate the polymerization. The polymerization was carried out for 5 h.

The emulsion polymerization product appeared as dark brown. A magnet was used to harvest the particles containing the cobalt ferrite nanoparticles. We estimate from the magnetization measurements that we magnetically harvested 5% of the polystyrene particles. These polystyrene cobalt ferrite composite particles contain on the average 5 wt % cobalt ferrite nanoparticles. We increased the cobalt ferrite loading by adding more cobalt ferrite particles to the emulsion polymerization recipe. Figure 1A shows ferromagnetic particles containing 14 wt % cobalt ferrite.

Characterization of Nanosize Cobalt Ferrite and Magnetic Composite Particles. X-ray powder diffraction studies utilized a Philips X'PERT system. A Zeiss EM 902A was used to measure the transmission electron micrographs. A Quantum Design MPMS superconducting quantum interference device (SQUID) magnetometer was used to determine the magnetic properties of the cobalt ferrite nanoparticles and the polystyrene cobalt ferrite composite particles at room temperature between ±50 kOe.

PCCA Fabrication. The suspension of polystyrene cobalt ferrite composite particles, which was dialyzed against pure water and then further deionized with ion-exchange resin, self-assembles into a CCA because of the electrostatic repulsion between these highly charged particles. Polymerized CCAs (PCCAs) were prepared by dissolving 0.1 g of acrylamide (Fluka), 0.025 g of cross-linkers N,N-methylenebisacrylamide (BAM, Fluka), and a drop of UV photoinitiator diethoxyacetophenone (DEAP, Acros) into a 1-mL diffracting suspension containing the polystyrene cobalt ferrite composite particles. This mixture was injected into a cell consisting of two quartz plates, separated by a 35-μm Parafilm spacer. The cell was exposed to UV light from a Blak Ray (365 nm) mercury lamp to initiate polymerization.[30]

Diffraction Measurements. The diffraction spectra of the CCA and PCCA were measured by using a Model 440 CCD UV-vis spectrophotometer (Spectral Instruments, Inc.) coupled to a nine-around-one reflectance probe optical fiber. Incident light transmits out of the central fiber, and we detect the light back diffracted by the CCA collected by the nine surrounding fibers. Transmission measurements were measured by using a Perkin-Elmer Lambda 9 absorption spectrophotometer. The CCA and PCCA samples were always oriented normal to the incident light beam.

81